COHERENCE PROTECTION IN COUPLED QUBIT SYSTEMS

Helen Mary Cammack

A Thesis Submitted for the Degree of PhD
at the
University of St Andrews

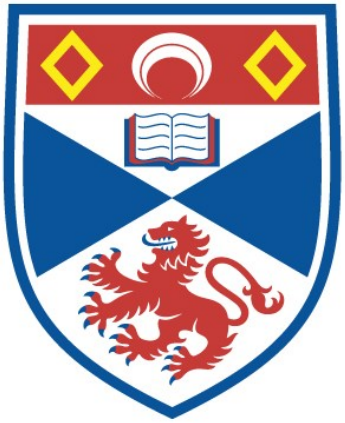

2018

Coherence Protection in Coupled Qubit Systems

Helen Mary Cammack

University of
St Andrews

This thesis is submitted in partial fulfilment for the degree of

Doctor of Philosophy (PhD)

at the University of St Andrews

July 2018

Candidate's declaration

I, Helen Mary Cammack, do hereby certify that this thesis, submitted for the degree of PhD, which is approximately 19,000 words in length, has been written by me, and that it is the record of work carried out by me, or principally by myself in collaboration with others as acknowledged, and that it has not been submitted in any previous application for any degree.

I was admitted as a research student at the University of St Andrews in August 2013.

I received funding from an organisation or institution and have acknowledged the funder(s) in the full text of my thesis.

Date 29/10/18 Signature of candidate

Supervisor's declaration

I hereby certify that the candidate has fulfilled the conditions of the Resolution and Regulations appropriate for the degree of PhD in the University of St Andrews and that the candidate is qualified to submit this thesis in application for that degree.

Date 29/10/18 Signature of supervisor

Permission for publication

In submitting this thesis to the University of St Andrews we understand that we are giving permission for it to be made available for use in accordance with the regulations of the University Library for the time being in force, subject to any copyright vested in the work not being affected thereby. We also understand, unless exempt by an award of an embargo as requested below, that the title and the abstract will be published, and that a copy of the work may be made and supplied to any bona fide library or research worker, that this thesis will be electronically accessible for personal or research use and that the library has the right to migrate this thesis into new electronic forms as required to ensure continued access to the thesis.

I, Helen Mary Cammack, have obtained, or am in the process of obtaining, third-party copyright permissions that are required or have requested the appropriate embargo below.

The following is an agreed request by candidate and supervisor regarding the publication of this thesis:

Printed copy

No embargo on print copy.

Electronic copy

No embargo on electronic copy.

Date 29/10/18 Signature of candidate

Date 29/10/18 Signature of supervisor

Underpinning Research Data or Digital Outputs

Candidate's declaration

I, Helen Mary Cammack, hereby certify that no requirements to deposit original research data or digital outputs apply to this thesis and that, where appropriate, secondary data used have been referenced in the full text of my thesis.

Date 29/10/18 Signature of candidate

I write differently from what I speak, I speak differently from what I think, I think differently from the way I ought to think, and so it all proceeds into deepest darkness.

Franz Kafka

Abstract

Decoherence is a major barrier to the implementation of quantum technologies. Theoretical techniques for understanding decoherence in composite systems have traditionally been focused on systems with distinguishable emission spectra, where measuring the frequency of an emitted photon allows one to determine which process took place. Here the photon contains information about the state of the system.

On the other hand, systems with indistinguishable spectra do not necessarily completely reveal information about the state of the system when a photon is emitted. It can be impossible to say for certain which of two nearly degenerate transitions has occurred just by measuring the photon's frequency. It is then possible to preserve information within the system throughout the decay process.

In this Thesis we show that indistinguishable spectra can lead to protected coherences within one part of a coupled quantum system, even as another part decays. We develop a zero-temperature exact approach for modelling such systems, and compare it to the microscopically derived Born-Markov master equation. This comparison helps us to understand the range of validity of the Markovian approximation. We use this understanding to extend the master equation approach to finite temperature within the Markovian regime, and we compare its high temperature results to a semiclassical model.

We examine the physical conditions required for coherence protection, and remarkably we find that heating the system can improve coherence protection. Similarly, increasing the decay rate of the unprotected part of the coupled system can also enhance the coherence of the protected part. These effects are the results of linewidth broadening and thus greater spectral indistinguishability.

The findings in this Thesis are of interest to both those seeking to engineer hybrid quantum systems and those seeking to develop theoretical techniques for dealing with the decoherence of composite quantum systems.

Publications

This thesis is based on the following publications:

Coherence protection in coupled quantum systems. H. M. Cammack, P. Kirton, T. M. Stace, P. R. Eastham, J. Keeling, and B. W. Lovett. Physical Review A **97**, 022103 (2018).

Bath induced coherence and the secular approximation. P. R. Eastham, P. Kirton, H. M. Cammack, B. W. Lovett, and J. Keeling. Physical Review A **94**, 012110 (2016).

Acknowledgements

General acknowledgements

Every thesis is a journey, and this one has been a very bumpy ride at times. Many thanks to Brendon Lovett for your support, encouragement and eternal patience. You continued to believe in me even when I didn't believe in myself. Not only have you helped me navigate the world of quantum information, you have supported me in pursuing my science communication interests. No question was ever too stupid to ask whilst in your office. My thanks also go to Jonathan Keeling, whose physical and mathematical insights have been invaluable in this work. You have been an exceptional co-author to work with.

As well as support for my academic work, I have been very fortunate to receive pastoral support from many individuals. Brendon, Jonathan, Vivienne Wild and Chris Hooley have all helped immensely, particularly during the difficulties of the last few months. Thank you all. The CM-CDT office staff have been absolutely outstanding, helping with administration and financial issues, but also providing a sympathetic ear whenever I popped in. A special mention goes to Julie Massey, who combines efficiency with great kindness and empathy. You do a wonderful job.

I have had some excellent officemates during my PhD. Steven Thomson, your dedication to theoretical physics is awe-inspiring. Thank you for excellent office conversation, and for encouraging me to take my first steps into science communication. Thank you also to Conor Stevenson and Rhea Stewart, who have provided lovely office company.

During my time as a PhD student I have developed a passion for public engagement. No-one I know epitomises the values of public engagement or is a more passionate advocate for it than Mhairi Stewart. Working with you has been inspirational. You have shown me a world where researchers enter into dialogue with the public as equals, and I know that this is the world I want to help create and sustain.

Thank you also to Gregor Steele of SSERC for excellent discussions on presenting quantum physics to a non-specialist audience, and for sharing your educational expertise with me. I greatly enjoyed the hours I spent making physics animations with you.

I have met many excellent people via public engagement activities, including Kate Cross. We met for stand-up comedy science silliness; now I'm lucky to count you among my closest friends. Wigwams have many supports, and Steph Nixon and Jess Werrell

have also done so much to support me and help me be the person I am today. Thank you all for your friendship; you know it means a lot.

Looking back, there are key people without whom I never would have started this PhD, never mind finished it. My college teachers Pam Dugdale and Andrew Tunstall kindled my love of physics and mathematics – thank you both. Thank you also to my family, who have always been there with their unconditional love and support. Without you I wouldn't be the person that I am today. Last but not least, thank you so much to Phillie. You've been an exceptionally good person through some very difficult times, and your friendship is very dear to me.

Funding

This work was supported by the Engineering and Physical Sciences Research Council [grant number EP/G03673X/1]; the Scottish Doctoral Training Centre in Condensed Matter Physics; and the University of St Andrews (School of Physics and Astronomy).

Research Data/Digital Outputs access statement

All of the materials required to reproduce these results are available within this Thesis.

Contents

Chapter 1

Introduction

"Begin at the beginning," the King said gravely, "and go on till you come to the end: then stop."

Lewis Carroll, Alice in Wonderland

1.1 Motivations

In life everybody has their own strengths and weaknesses, and the most fruitful collaborations occur when diverse individuals with complimentary skills work together for a common goal. These teams often behave in a more complex way than the sum of their individual parts, and such partnerships can often lead to surprising results.

So it is within the world of quantum computing: the basic unit of a quantum computer, the qubit, can be realised in many different ways, each of which has its own physical properties. The most promising quantum computing schemes consist of multiple qubit types coupled together, each one performing its own specialist function. However the

behaviour of these hybrid schemes is more complex and the act of coupling different quantum systems together can lead to unexpected phenomena.

In this Thesis we study coupled quantum systems from a theoretical standpoint. The time evolution of a single quantum system weakly coupled to a thermal environment can generally be described using the *Lindblad equation*. The Lindblad equation models system behaviour as the result of a set of individual transition processes, each occurring at its own rate. Implicit in this model is the assumption that each individual transition is distinct from all of the others, so that when a system process occurs the frequency of the emitted photon would allow an observer to confidently infer which process has taken place.

The Lindblad equation has also been traditionally used to model coupled quantum systems, particularly in the field of quantum optics. In quantum optics, two different quantum systems – light and matter – are coupled together by placing the matter inside an optical cavity. So long as the light is quite weakly coupled to the matter, as is usually the case, each individual transition is distinguishable from all others by measuring the output photon frequency, so here the Lindblad equation is valid.

However when we use the Lindblad equation on other types of coupled quantum systems, we run into problems. For example, once it is no longer possible to fully distinguish between two different transitions by measuring the emitted photon's frequency, these two transitions interfere with one another and the Lindblad equation no longer describes the system behaviour. Many types of coupled quantum systems fall into this category, and among them are some of the most promising quantum computing schemes. The variation in qubit properties that proves such an advantage when constructing a quantum computer can also necessitate a more complex theoretical description.

Here we examine the behaviour of these composite systems using a variety of theoretical techniques, both at zero and at finite temperature. Along the way, we reveal ways of protecting quantum coherence in surprising regimes, including at high tempera-

ture. The indistinguishable transitions that cause the invalidity of the Lindblad equation also provide a way of preventing the loss of quantum information to the environment. When a system with overlapping spectral lines emits a photon, the photon's wavelength does not allow one to determine for certain which transition has occurred. The emitted photon contains less information about the system from which it was emitted, and as we shall see, this can be used to protect quantum coherences from being lost to the environment.

Therefore this work is of interest both to those wishing to enhance coherence protection within physical systems, and to those looking for a more accurate theoretical treatment of coupled quantum systems beyond the Lindblad equation.

1.2 Outline of Thesis

In this Thesis we consider a coupled two-qubit open quantum system. Firstly in Chapter 2, we consider the limitations of classical computing and the need to develop robust quantum computers. Then we introduce the key mathematical properties of qubits and the differences between quantum and classical states. We finish Chapter 2 by reviewing the progress made to date in realising a physical quantum computer. We assess the most promising qubit types: donor spins in solid-state systems, quantum dots, superconducting qubits, optical qubits and ultracold atoms. Chapter 2 finishes with an overview of hybrid quantum computing schemes. These schemes inform the model that we study in the rest of this Thesis.

Having introduced key quantum information concepts, in Chapter 3 we turn to the effect of the environment on a quantum system. We define an open quantum system and introduce two main approximations commonly made when dealing with open quantum systems: the Born and Markov approximations. Next we cover the model used to describe the environment and its effect on the system of interest.

In Chapter 3 we then derive two separate models for studying a coupled open quantum system. The first model is the Born-Markov quantum master equation, which is valid at zero and at finite temperature, but (as the name suggests) relies on the Born and Markov approximations. We examine the additional approximation required to turn a general quantum master equation into a Lindblad equation, and the consequences of remaining in non-Lindblad form. The second model is an exact approach which uses the Schrödinger equation in the single-excitation subspace, valid only at zero temperature. We will use both of these methods later on in the Thesis.

In Chapter 4 we apply each of these methods in turn to a coupled two-qubit open quantum system. The model we use is informed by the hybrid computing schemes reviewed in Chapter 2. In Chapter 4 we study this system at zero temperature in order to compare the results obtained using the Born-Markov master equation to those found with the exact approach (both detailed in Chapter 3). By doing this, we are able to assess the validity of the Born-Markov approximations within relevant parameter regimes. We also demonstrate coherence protection in coupled quantum systems, and detail the conditions required to maximise this.

Having assessed the validity of the Born-Markov master equation at zero temperature, in Chapter 5 we extend this to finite temperature. We look at the dynamics across different temperature regimes and find three distinct patterns of behaviour. In particular, the high temperature regime exhibits significant coherence protection due to broadening of the transition linewidths. We examine the limitations of the Born-Markov solution at very high temperature and consider a semiclassical model, which we compare to the Born-Markov solution. We describe the limitations of this semiclassical model, which also implicitly uses the Markov approximation. Finally, in Chapter 6 we conclude the Thesis and give suggestions for future experimental and theoretical work.

Chapter 2

Quantum Information Processing

Information about the package is as important as the package itself.

Frederick W. Smith

In this Chapter we give an introduction to quantum computing and review the mathematical and physical properties of qubits. We cover superposition, entanglement, coherence and density matrices, laying the foundations for the mathematical treatment of decoherence given in Chapter 3. The main physical qubit candidates are reviewed and their merits are assessed. We also discuss candidate hybrid quantum computing systems of relevance to this Thesis.

2.1 Quantum computing

First we look at the origins of quantum computing, starting with its classical counterpart, and discuss some of the motivations behind the development of quantum computing.

2.1.1 Classical computing

All classical computers are fundamentally made up of many bits – transistors that act as miniature 'switches' which can be 'off' or 'on'. These states are represented by the values 0 and 1 respectively. Computations are carried out by applying logic gates to input bits and the results are stored in RAM. The one-bit gate is the `NOT` gate, made from a single transistor. The two-bit gates `OR`, `AND` and `XOR` can all be made from different combinations of `NOR` gates. More complicated mathematical operations such as addition are made from combinations of these basic one and two-bit gates [1]. These operations are in turn combined to form programs, operating systems and so on.

The computational power of a device depends on many complex and interacting factors, but a key element is the number of transistors it contains. In 1965, Gordon Moore predicted that the number of transistors in an integrated circuit would double every year for at least a decade [2]. The exact time period for this doubling has since been revised, but the exponential growth in the number of transistors has continued for far longer than Moore originally anticipated, accompanied by decreasing transistor size (see Figure 2.1).

However all good things must come to an end, and Moore's Law has begun to fail due to the extra heat that is generated from having so much circuitry in such a small area. Quantum tunnelling also starts to cause leakage problems on such small length scales. The computing industry has other strategies to keep increasing computing power,

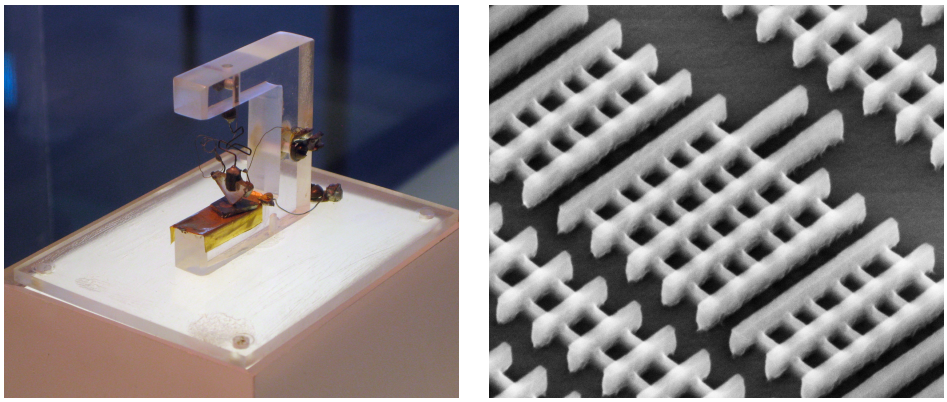

Figure 2.1: Left [3]: the first point-contact transistor measuring around 1cm, invented at Bell Labs in 1947 [4], for which Bardeen, Brattain and Shockley jointly received the Nobel Prize in Physics in 1956 [5]. Right [6]: Intel's 22nm tri-gate transistor, introduced in 2011. Intel has since released processors incorporating 14nm transistors [7].

however some problems will always remain out of reach of a classical computer due to how the number of operations in an algorithm can scale with input size [8]. For example, if we wished to model the quantum-mechanical effects of all the electrons in a mole of a metal, we would need 10^{23} classical bits to store the system's state – an improbably large number.

2.1.2 Quantum computing

Quantum computing offers a completely different approach. Rather than classical bits which must be either 1 or 0, a quantum computer is made from *qubits* – quantum bits – which can exist in a superposition of the two quantum mechanical states $|1\rangle$ and $|0\rangle$ (the concept of superposition will be covered in more detail in Section 2.2.1). Richard Feynman gave a lecture on a quantum mechanical computer published in 1982 [9], but it was David Deutsch's description of a universal quantum computer in 1985 [10] that is credited with launching the field.

Quantum computations rely on two properties – superposition and entanglement, covered in more detail in Section 2.2.1. Both of these properties are fundamentally

quantum and do not have a classical analogue. They allow quantum computers to take advantage of quantum parallelism, whereby a function can be evaluated for many different input values simultaneously [11]. A quantum computer comprised of n qubits can be used to encode 2^n states which can all be fed into the quantum algorithm simultaneously.

However, in order to extract information about multiple states at the end of the computation, it is necessary to design algorithms that take advantage of interference between quantum states. This can often be done by a judicious choice of final transformation in order to extract the maximum possible amount of information from the system. Examples of this include Shor's algorithms for finding discrete logarithms and factorising integers on a quantum computer, which provide exponential speed up [12]; and Grover's search algorithm for an unsorted database which offers quadratic speed up [13].

Many different physical qubit realisations have been proposed, and these will be reviewed in Section 2.3. The past two decades have seen an explosion of research activity centred around quantum information and quantum computing, and yet a physical universal quantum computer remains elusive. The primary reason for this is that quantum states are very fragile and susceptible to environmental influence. This influence causes *decoherence* and destroys the superposition state needed to run quantum computations. Without proper knowledge and control over decoherence, we can never hope to construct a fault-tolerant quantum computer.

Efforts to control decoherence are broadly split into two strands: protecting qubits in order to increase their coherence times, and the use of error correction algorithms [14]. This Thesis shall focus on the former; in Section 2.2 we introduce the mathematical formalism necessary to describe qubits and coherence, whilst in Chapter 3 we will look at the mathematical treatment of decoherence.

2.2 Mathematical properties of qubits

Before looking at physical qubit candidates, let us review the key mathematical properties of qubits: superposition, entanglement and coherence. These properties separate qubits from classical bits, and as such are vital for any quantum computation.

2.2.1 Superposition and entanglement

Superposition

A qubit can exist in a superposition of two states, and has the form:

$$|\psi\rangle = \alpha|0\rangle + \beta|1\rangle, \tag{2.1}$$

where the coefficients α and β are complex numbers. The states $|0\rangle$ and $|1\rangle$ are orthonormal and are known as computational basis states [11]. Note that the above equation assumes that the qubit is in a pure state; pure and mixed states are covered more fully in Section 2.2.2.

As we require the qubit to exist within the vector space defined by two orthonormal states, the two level system (TLS) is a natural choice for qubit representation. If we were to measure the qubit's state, the result would either be 0 (with probability $|\alpha|^2$) or 1 (with probability $|\beta|^2$).

Since all probabilities must sum to one, $|\alpha|^2 + |\beta|^2 = 1$. This allows us to rewrite Equation 2.1 as [11]:

$$|\psi\rangle = \cos\left(\frac{\theta}{2}\right)|0\rangle + e^{i\phi}\sin\left(\frac{\theta}{2}\right)|1\rangle, \tag{2.2}$$

where θ and ϕ are real numbers which define a point on the surface of a three-dimensional sphere of unit radius. This sphere (shown in Figure 2.2) is known as the Bloch sphere, and it provides a way of visualising the state of a qubit. For example, the state $|0\rangle$ lies

at the 'North pole' of the Bloch sphere, whilst the equal superposition $\frac{1}{\sqrt{2}}(|0\rangle + |1\rangle)$ lies along the x axis. Unfortunately there is no such convenient visualisation of the state of a multi-qubit system.

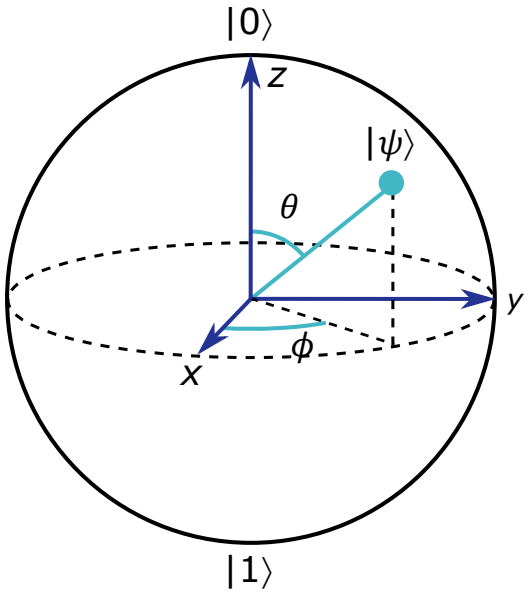

Figure 2.2: Representation of a qubit on the surface of the Bloch sphere.

Entanglement

Unlike superposition, entanglement is specifically a multi-qubit effect and can be thought of as non-classical correlations [15]. To see how entangled states and non-entangled states differ, let us consider two (initially unentangled) qubits a and b, each in a pure state of the form $|\psi_i\rangle = \alpha_i|0\rangle_i + \beta_i|1\rangle_i$ (where $i \in \{a, b\}$). The total state of the combined system is then given by the product state:

$$\begin{aligned} |\psi\rangle &= |\psi_a\rangle \otimes |\psi_b\rangle \\ &= \big(\alpha_a|0\rangle_a + \beta_a|1\rangle_a\big) \otimes \big(\alpha_b|0\rangle_b + \beta_b|1\rangle_b\big) \\ &= \alpha_a\alpha_b|00\rangle + \alpha_a\beta_b|01\rangle + \alpha_b\beta_a|10\rangle + \beta_a\beta_b|11\rangle, \end{aligned} \tag{2.3}$$

where $|ij\rangle$ denotes the two-qubit state containing qubit a in state $|i\rangle$ and qubit b in state $|j\rangle$. (This notation is also used to describe multi-qubit systems of arbitrary size, $|\psi_1, \psi_2, \cdots, \psi_n\rangle$.) The system described in Equation 2.3 is not entangled because it is possible to write the system state as a product of the state of qubit a and the state of qubit b.

The state of a two-qubit system (entangled or unentangled) is generally written in the form:

$$|\psi\rangle = \alpha|00\rangle + \beta|01\rangle + \gamma|10\rangle + \delta|11\rangle, \tag{2.4}$$

where $\alpha, \beta, \gamma, \delta$ are complex coefficients. This system is only unentangled if $|\alpha\delta - \beta\gamma| = 0$. Otherwise, it is entangled and it is not possible to separate the state of a from that of b. The four Bell states form an orthonormal basis of maximally entangled two-qubit states [15]:

$$\begin{aligned}
|\Psi^-\rangle &= \frac{1}{\sqrt{2}}\big(|01\rangle - |10\rangle\big), \\
|\Psi^+\rangle &= \frac{1}{\sqrt{2}}\big(|01\rangle + |10\rangle\big), \\
|\Phi^-\rangle &= \frac{1}{\sqrt{2}}\big(|00\rangle - |11\rangle\big), \\
|\Phi^+\rangle &= \frac{1}{\sqrt{2}}\big(|00\rangle + |11\rangle\big).
\end{aligned} \tag{2.5}$$

If we were to take a system in a Bell state and measure one spin component of one qubit, the same spin component of the other qubit would be immediately determined, no matter how far apart the two qubits were located. Entangled qubits separated by 1.3 kilometres have been produced, violating any theory of nature that obeys both locality and realism [16].

2.2.2 Coherence

We have seen that a superposition of states is required for quantum computing, but in what way does superposition differ from classical uncertainty about which state a system is in? Here we examine how these two cases differ and how they can be represented mathematically.

Pure states

A qubit in a pure state is completely defined by the state vector $|\psi\rangle$ of form given in Equation 2.1, so that it sits on the surface of the Bloch sphere as shown in Figure 2.2. For example, a spin-based TLS may be in the superposition state:

$$|\psi\rangle = \frac{1}{\sqrt{2}}\left(|\uparrow\rangle + |\downarrow\rangle\right), \tag{2.6}$$

where $|\uparrow\rangle$ denotes the spin-up state and $|\downarrow\rangle$ the spin-down state projected onto the z axis. In order to gain information about the state of the spin, we must perform measurements on it. To do this, we must choose which measurements to perform. For example, we could gain information about either the x or the z-projection of the spin.

In quantum theory, an observable A is associated with a Hermitian operator $\hat{A}$. The operators associated with spin measurements are the Pauli matrices:

$$\hat{\sigma}_x = |\uparrow\rangle\langle\downarrow| + |\downarrow\rangle\langle\uparrow|, \quad \hat{\sigma}_y = +i\big(|\downarrow\rangle\langle\uparrow| - |\uparrow\rangle\langle\downarrow|\big), \quad \hat{\sigma}_z = |\uparrow\rangle\langle\uparrow| - |\downarrow\rangle\langle\downarrow| \,. \tag{2.7}$$

Suppose we wish to measure the z-projection of our TLS. Upon measurement, the system is projected into one of the two eigenstates of σ_z: $|\uparrow\rangle$ or $|\downarrow\rangle$. The probability of obtaining an 'up' result is:

$$|\langle\uparrow|\psi\rangle|^2 = \frac{1}{2}, \tag{2.8}$$

since the eigenstates are orthonormal.

So when we measure the spin z-projection, there is a 50% chance we obtain the answer 'up', and 50% that we record 'down'. However, this is distinctly different to the classical case where a coin is flipped, because our quantum state $|\psi\rangle$ is in *superposition*. The implications of this become clear when we swap our measurement basis.

Let us instead measure the spin's x-projection. The eigenstates of σ_x are $|+\rangle = \frac{1}{\sqrt{2}}(|\uparrow\rangle + |\downarrow\rangle)$ and $|-\rangle = \frac{1}{\sqrt{2}}(|\uparrow\rangle - |\downarrow\rangle)$, so an x-measurement of the original state $|\psi\rangle$ returns '$+$' with probability 1. If $|\psi\rangle$ were either 'up' *or* 'down', a measurement in the x-basis would have been $50:50$. In this way, we see that a quantum superposition state is not the same as a classically probabilistic system, and this distinction will be important later.

Mixed states and density matrices

Pure states such as Equation 2.6 can be fully described by their state vector $|\psi\rangle$. However sometimes we don't know for certain which pure state the system is in. All we know is that the system has the probabilities p_n to be in normalised states $|\psi_n\rangle$. Then the system is in a mixed state, and is fully described by its density matrix ρ [15]:

$$\rho = \sum_n p_n |\psi_n\rangle\langle\psi_n|. \tag{2.9}$$

Note that throughout this Thesis, we will use the following notation to refer to an element of a density matrix in a given normalised basis:

$$\rho_{m,n}(t) \equiv \langle m|\rho(t)|n\rangle. \tag{2.10}$$

The density matrix has the following properties:

- **Unit trace** ($\mathrm{Tr}[\rho] = 1$): the sum of the probabilities must equal one.

- **Hermiticity** ($\rho = \rho^\dagger$): evident from the definition of ρ, noting that $p_n \in \mathbb{R}$.
- **Positivity** ($\langle\phi|\rho|\phi\rangle \geq 0$): all probabilities must remain positive, no matter what orthonormal basis they are measured in.

The above properties ensure that the density matrix at some particular time is physical. To ensure that the time evolution of the density matrix is physical, we also need to impose a condition on the maps which act on it. In this context, the map is the time evolution of the density matrix from some time t_1 to a later time t_2, so a condition on the map is a condition on the allowed dynamics.

The density operator must be acted on by *completely positive* maps. To understand this, let us consider the action of maps on composite systems made up of two or more subsystems. If a map acting on a particular subsystem is positive (and trace-preserving), it transforms density operators of that subsystem into density operators. If the map acting on a subsystem is completely positive, then the extended map acting on the composite system is also positive [17].

It is also useful to define the purity of a state, $\mathrm{Tr}[\rho^2]$. A pure state has a purity of one, whereas the purity of a mixed state is less than one and greater than or equal to zero. Whereas a pure state corresponds to a point on the surface of the Bloch sphere (Figure 2.2), a mixed state is represented by a point inside the Bloch sphere [15].

The expectation value of an operator $\hat{A}$ is:

$$\langle\hat{A}\rangle = \mathrm{Tr}[\rho\hat{A}]. \tag{2.11}$$

(The trace operation is $\mathrm{Tr}[\hat{X}] = \sum_n \langle\phi_n|\hat{X}|\phi_n\rangle$, where $|\phi_n\rangle$ is any orthonormal basis [15].)

Sometimes we deal with a composite system made up of two subsystems, and then

it is useful to talk of a reduced system density matrix, found by taking a partial trace:

$$\rho_1 = \mathrm{Tr}_2[\rho]. \tag{2.12}$$

This traces over all the degrees of freedom associated with subsystem 2, leaving ρ_1, which acts in the Hilbert space of subsystem 1.

Populations and coherences

Let us return to our TLS with the pure state defined in Equation 2.6. Its density matrix written in the basis $\{|\uparrow\rangle, |\downarrow\rangle\}$ is:

$$\rho_{TLS} = \frac{1}{2}\begin{pmatrix} 1 & 1 \\ 1 & 1 \end{pmatrix}. \tag{2.13}$$

Let us contrast that with the flipped coin, which we know is either in state 'up' or 'down'. The coin has the density matrix:

$$\rho_{coin} = \frac{1}{2}\begin{pmatrix} 1 & 0 \\ 0 & 1 \end{pmatrix}. \tag{2.14}$$

The purity of ρ_{TLS} is one, whilst the purity of ρ_{coin} is $1/2$ – so the TLS is in a pure state, whilst the coin is in a mixed state.

The diagonal elements of the two density matrices are the same – these are the *populations*, which represent the probabilities that the system is in each of the basis states. The off-diagonal elements are the *coherences*, which provide information about whether the system is in a pure or a mixed state.

To understand more about the coherences, let us rewrite ρ_{TLS} in the x basis,

$\{|+\rangle, |-\rangle\}$:

$$\rho_{TLS} = \begin{pmatrix} 1 & 0 \\ 0 & 0 \end{pmatrix}. \tag{2.15}$$

We can now see that the system is in the pure state $|+\rangle$. Written in this basis, ρ_{TLS} has no coherences associated with it because the population of $|-\rangle$ is zero. If the populations of two basis states are non-zero and the coherence between those two states is zero (as in ρ_{coin}), then the system is in a mixed state. Rewriting ρ_{coin} in the x basis would not change the matrix; it remains in the form of Equation 2.14.

The density matrix represents a statistical mixture of a number of states. Each of these states may or may not be superposition states with respect to a particular basis. Coherences between different states in a given basis are represented by off-diagonal elements of the density matrix in that basis. Coherent manipulation of a state maintains that state's purity as it is rotated around the Bloch sphere, so it maintains a well-defined local phase. Decoherence is the loss of a well-defined local phase, and it presents a major challenge to all quantum information technologies. This will be discussed in more detail in Chapter 3.

2.3 Physical quantum computers

Having discussed which mathematical properties separate qubits from their classical counterparts, in this Section we summarise the progress made in the physical implementation of quantum information systems. We will confine our discussions to spatially localised qubits as non-localised proposals such as topological qubits [18] fall outside of the scope of this work.

2.3.1 Physical qubits

DiVincenzo laid out the "five requirements for the implementation of quantum computation" [19]. These are:

1. **'A scalable physical system with well characterised qubits'**: The qubit's Hamiltonian should be well known and the qubit should be an effective two level system.

2. **It must be possible to initialise the qubits into a simple low-entropy state, such as** $|000\cdots\rangle$: We must be able to initialise the register into a known state before the computation begins.

3. **'Long relevant decoherence times, much longer than the gate operation time'**: See Section 2.2.2 for further discussion of coherence.

4. **'A universal set of quantum gates'**: The set of quantum gates consisting of all one-bit gates plus the two-bit `XOR` gate is universal, as all many-bit gates can be constructed from combinations of these gates [20].

5. **It must be possible to measure specific qubits**: We must be able to read out the result of a computation.

Here we review the most promising physical qubit candidates against DiVincenzo's criteria.

Donor spins in solid-state systems

Donor atoms in solid state materials possess bound electrons at low temperature which can act as spin-based qubits. Silicon is the most commonly-used host material, and offers exceptionally long spin coherence times – a coherence time of over 39 minutes at room temperature (rising to 3 hours at low temperature) was recently achieved using

phosphorus-31 donors [21]. Electron spin coherence times exceeding seconds have been measured in high-purity silicon at 1.8 K [22]. These long coherence times are due to the low spin-orbit coupling and a low proportion of nuclear spins within silicon [23]. In addition, there is already a detailed understanding of silicon's properties, and advanced silicon chip fabrication knowledge and infrastructure currently exists.

Historically, manipulating nuclear spin qubits has proved difficult due to their weak polarization under experimentally accessible conditions. Additionally, whilst AC magnetic fields can be used to manipulate nuclear spins, it is challenging to spatially confine these so as to address a single spin. More recent proposals have focused around the use of electric fields to control donor spins [24] or the use of coupled electron spin qubits [25] (see also Section 2.3.2).

In addition to bound electon spins, many donors possess nuclear spin which can also be used for storing quantum information. The most popular dopant is phosphorus-31, which has a nuclear spin of $\frac{1}{2}$ (see e.g. [21]). Other elements are also being considered, for example bismuth, which offers a larger Hilbert space for computations due to a nuclear spin of $\frac{9}{2}$ in Bi-209 [26].

Donor spins can be manipulated using established electron spin resonance (ESR) techniques, whereby resonant microwaves are used to alter the electron spin state [27]. The duration and phase of the microwave pulse can be adapted to produce all required qubit gates [23]. Read out can be achieved using magnetic resonance [28] or via coupling to other degrees of freedom such as an optical system.

Dopants are also used in other solid state systems to produce spin-based qubits with long decoherence times. Zhong *et al.* achieved a six-hour coherence time by using europium ion dopants in yttrium orthosilicate [29].

Nitrogen vacancy (NV) centres in diamond are another promising dopant-based system. Selected carbon atoms from the diamond are replaced by nitrogen dopants, which only bond to three neighbouring atoms, leaving one site vacant (see Figure 2.3) [30].

The NV centre has a single negative charge and forms a spin triplet. The system can be optically pumped into the initial spin state [31], coherently manipulated using resonant microwaves [32] and detected using spin-dependent fluorescence [31]. Long-distance entanglement is possible using NV centres, and has been demonstrated for spins separated by over one kilometre [16].

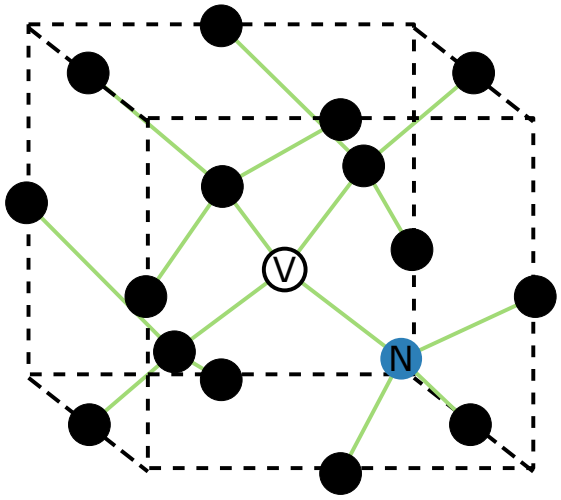

Figure 2.3: A nitrogen vacancy centre in a diamond lattice, with carbon atoms depicted in black, nitrogen in blue and vacancy in white.

NV centres have achieved electronic spin coherence times approaching one second [33]. Coherence times of NV centres are high, even at room temperature, due to weak spin-orbit coupling and almost no nuclear spins within the carbon lattice [31]. This property has lead to the proposal of a scalable architecture for implementing room-temperature NV centre-based quantum computers [34].

The greatest challenge in building scalable solid-state spin-based quantum computers is facilitating the interactions between qubits [31]. The exchange interaction has very short range, necessitating the use of optical modes to connect qubits. Placing donor spins with the required precision is challenging [23], though scanning tunnelling microscopy has been used to place single phosphorus dopants in silicon with atomic precision [35]. Long distance transmission of quantum states would require coupling to an optical mode,

however phosphorus donors in silicon suffer from low measurement efficiency [23]. Solid-state spins are likely to be used as quantum memory, coupled to other degrees of freedom in a hybrid quantum computer (see Section 2.3.2).

Quantum dots

Quantum dots are artificial atoms created by confining one or more electrons (or holes) into a localised potential, so that they have discrete energy levels in just the same way as an atomically bound electron. The confinement may be implemented in several different ways; it can be lithographically defined or self-assembled [31]. Lithographically defined quantum dots have a shallower potential and so require temperatures of less than 1 K, whereas self-assembled quantum dots operate at somewhat higher temperatures ($\sim$4 K) [31]. Self-assembled quantum dots grow on strained heterostructures, forming a regular pattern of islands. This was first demonstrated by Goldstein *et al.*, who grew self-assembled quantum dots on a InAs/GaAs strained-layer superlattice [36].

Loss and DiVincenzo first described how lithographically defined quantum dots could be used to construct a universal set of quantum gates [37]. In this proposal, coupling between qubits is enacted by changing the tunnelling barrier between neighbouring dots. The properties of quantum dots are highly tunable and they can be integrated into devices more easily than donors can [38]. However, self-assembled quantum dots form in random locations and have varying optical characteristics, both of which become increasingly problematic as system size increases [31].

Coherence times in quantum dots are much shorter than in doped silicon. Gallium and arsenic possess a nuclear spin, so any quantum dots made from these materials suffer from decoherence due to spin-spin interactions [39]. Silicon-28 has no nuclear spin, but silicon-oxide interfaces are highly flawed, trapping unwanted parasitic quantum dots [23]. Other materials such as silicon-germanium heterostructures have fewer interface defects, and coherence times of around 400 μs have been measured [40]. As with donor qubits,

coupling quantum dot qubits is a significant challenge, and is likely to involve other degrees of freedom such as optical or superconducting qubits.

Superconducting qubits

Superconducting qubits are integrated circuits made of superconducting materials, so there is no dissipation from electrical resistance. The electrons in a superconductor form Cooper pairs which are condensed into a single macroscopic state. This leads to two important properties: flux quantisation (the magnetic flux in a superconducting ring is quantised in units of $h/2e$) and Josephson tunnelling (Cooper pairs can tunnel coherently across an insulating gap between two regions of superconductor) [41]. Josephson tunnelling allows us to introduce nonlinearity to superconducting circuits without adding extra dissipation or dephasing [42]. The three basic types of superconducting qubit are flux, charge and phase, depending on which collective degree of freedom is used to encode the quantum information [41, 42].

Superconducting qubits exhibit exceedingly fast gate speeds: single qubit gate times are around 5 to 50 ns, whilst two qubit gate times are 50 to 500 ns [42]. These are much shorter than coherence lifetimes, which are $\sim$100 μs [42]. Readout can be achieved via quantum nondemolition measurements which allow continuous monitoring of the qubit, allowing errors to be detected and therefore corrected [42]. Superconducting circuit elements can be made using existing successful integrated circuit fabrication technologies. A quantum computer with five superconducting phase qubits has been used to factorise the number 15 using Shor's algorithm [43]. Classical states in a superconducting quantum circuit have been protected against bit-flip errors by using repetitive error detection techniques [44]. The microprocessor company IBM is conducting research into superconducting quantum computers and hopes to produce a superconducting qubit lattice capable of conducting quantum error correction in the near future [45].

Superconducting qubits must be cooled to mK using a dilution refrigerator to reduce

thermal noise [46] and shielded from external electromagnetic signals. The leads coupling the qubits to readout or control devices introduce considerable decoherence to the system [41]. In addition to these extrinsic sources of noise, there is also intrinsic low-frequency $1/f$ noise due to charge fluctuations, flux fluctuations and fluctuations in the critical current [41]. The individual superconducting qubits will never be perfectly identical, introducing more errors into gate operations. As the system is scaled up, controlling this decoherence becomes ever more important, challenging the capabilities of current error correction methods [42]. Scalable error correction could be achieved by use of surface codes (see e.g. [47] for a review) which use two-dimensional lattice of computational qubits and stabilisers to find and reverse errors.

Optical qubits

Photons have a number of degrees of freedom that can be used to encode a qubit, including polarisation, occupation number, and spin and orbital angular momentum [48]. Photons do not suffer from decoherence to the same extent that matter qubits do [49], and many-photon entangled states have been experimentally demonstrated (see e.g. [50–52]). In addition, photons are the leading candidate for qubit transmission [53], and indeed quantum states have been transmitted over a distance of 143 km using optical links [54]. Single photon gates can be easily implemented using beam splitters, phase shifters and photo-detectors [55].

However a major hurdle for optical qubits is that they do not interact directly, so multi-qubit gates are difficult to achieve. Progress in this area has been made with the construction of an all-optical `CNOT` gate [56], that, together with single-qubit rotations, form a universal set of quantum logic gates. However all-optical `CNOT` gates still suffer from low efficiency and low success rates [57]. Other challenges include the construction of high-efficiency single-photon detectors and engineering high-efficiency indistinguishable single-photon sources [49]. The most likely use of photons in a scal-

able, fault-tolerant quantum computer is for quantum communication between matter qubits [31].

Trapped atoms and ions

Ultracold atoms and ions can be trapped using static or oscillating electromagnetic fields. They have very long coherence times – up to several seconds [58]. As atoms/ions interact strongly with one another via the Coulomb interaction, gate operations are easy to construct [59]. Trapped ions were recently used to construct a five-qubit quantum computer capable of running Shor's algorithm [60]. Many cold atoms can be entangled together by use of optical pulses – Haas *et al.* [61] entangled forty cold atoms in an optical cavity; McConnell *et al.* [62] entangled around 3,000 atoms using a single photon.

Scaling trapped-ion gates remains a challenge. In order to achieve efficient laser cooling and suppress decoherence, high vibrational frequencies are required, however these result in ions which are closely spaced in the trap [59]. Addressing individual ions becomes very challenging, as this involves focusing a laser beam on the selected ion. Additionally the optical pulses used to manipulate the qubits induce decoherence by exciting unwanted modes; these modes become harder to avoid as the system size increases [59]. Recent proposals for scalable trapped-ion quantum computers centre around the use of modular systems in order to avoid these problems [63].

Summary of physical qubit types

The different types of qubit covered above are summarised in Table 2.1.

Qubit	Advantages	Disadvantages
Donor spins	Very long coherence times High-fidelity qubit detection and manipulation Can be made using existing fabrication techniques	Difficult to couple qubits Exchange interaction has a very short range
Quantum dots	Extremely tunable Can be integrated into devices more easily than donors can	Hard to couple many qubits Self assembled dots form in random locations and have varying optical characteristics
Superconducting	Fast gates – much faster than decoherence times Continuous monitoring of states possible Can be made using existing fabrication techniques	Readout and control leads add unavoidable decoherence Intrinsic decoherence of $1/f$ form is hard to overcome
Optical	Extremely long coherence times Excellent transmission over long distances Single qubit gates easy to construct	Inefficient single photon detectors Hard to generate indistinguishable single photons Multi-qubit gates very difficult to construct
Trapped atoms/ions	Long coherence times Many qubits can be entangled together with a single photon Easy to construct qubit gates	Decoherence scales with size Addressing individual atoms harder for large systems

Table 2.1: Summary of major qubit types

2.3.2 Hybrid quantum computing

Each type of qubit offers different advantages to quantum computing; however the most promising proposals use several types of qubits coupled together, each performing different functions. For example, the long relaxation times of nuclear qubits make

them ideally suited to performing as quantum memories, whilst photons are excellent at transmitting quantum information.

There are many different quantum computing proposals that make use of multiple qubit types (for a review see Kurizki *et al.* [64]). Here we focus on two hybrid quantum computing schemes that are directly relevant to this Thesis, though the theories that we present could be applied to numerous other hybrid quantum computing proposals. Figure 2.4 depicts a schematic of the hybrid schemes covered here. Note that the excitation frequencies of the different components are separated by several orders of magnitude – this separation of energy scales will prove important in later Chapters.

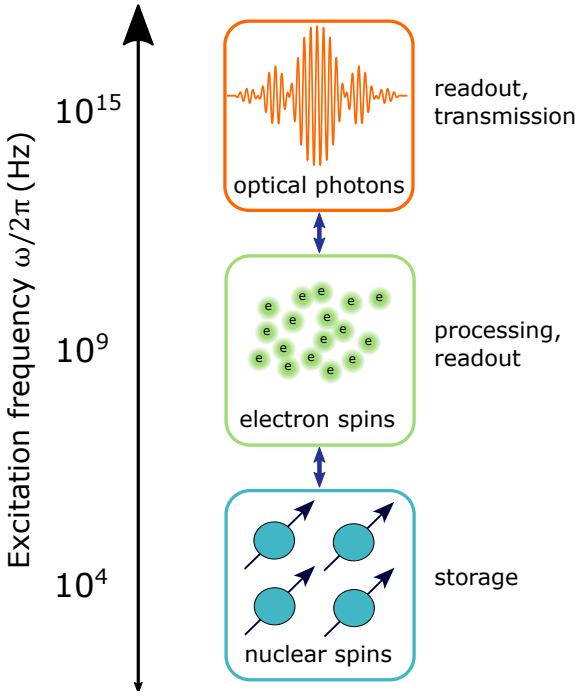

Figure 2.4: Three physical qubit systems which work together to perform the functions required by a quantum computer. These are arranged by the characteristic frequency needed to excite them. Dark blue arrows indicate coupling between the qubit types [64].

Electron-nuclear spin systems

As we have already seen, nuclear spins offer exceedingly long coherence times, making them well suited as memory qubits. However, addressing the nuclear spins is an issue, since they have weak spin splitting at achievable temperatures and magnetic field strengths. Electron spins have a much larger spin splitting as their magnetic moment is around 2,000 times greater than that of nuclear spins. The gate manipulation times of electron spins are also $\sim 10^3$ times faster than that of nuclear spins, and detection methods for electronic spins are more sensitive than those for magnetic spins [65].

For these reasons, there is considerable interest in hybrid electron-nuclear spin quantum computers, whereby the electronic spins are used for manipulation and the nuclear spins for storage. Such schemes typically require coherent state transfer between nuclear and electronic spin qubits. The coupled spin system has two different energy scales – the nuclear spin splitting is much smaller than that of the electron spin (Figure 2.5).

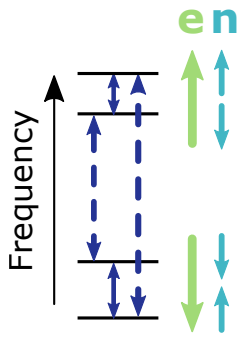

Figure 2.5: Coupling a spin-half nuclear spin to an electronic spin results in four energy levels. The splitting between nuclear spin states (dark blue solid lines) is typically in the radio-frequency regime (1-200 MHz), whilst the electronic splitting (dashed lines) is much larger, usually in the microwave regime (10-100 GHz) [65].

Nuclear-electron coupling in diamond

Electron spins associated with nitrogen vacancy colour centres in diamond provide a promising environment for hybrid quantum computing. The electronic spins are used for readout whilst nuclear spins provide memory [66, 67]. The electronic spins can be

addressed coherently through resonant microwave pulses [68]. Proximal ^{13}C nuclear spins can be coherently coupled to the electron spin and addressed individually due to quantum back-action which modifies nearby energy levels and magnetic moments [68]. ^{13}C nuclear spins in diamond have produced room-temperature coherence times of over one second [69].

However ^{13}C has a natural abundance of 1.1% and this lack of ^{13}C atoms coupled to NV centres causes issues with scalability, since it is desirable if the storage and processing qubits are always found together [70]. In contrast, the nitrogen ^{14}N nuclear spin is always present and its properties are determined by the NV centre geometry [71]. The hyperfine interaction between the optically excited electron spin and the N nuclear spin is $\sim$60 MHz, much larger than the coupling between the ground-state electron and nuclear spin [71].

Fuchs *et al.* [70] have demonstrated coherent quantum state transfer between electronic and nuclear nitrogen spins in NV centres with a transfer time of 120 ns and a total storage fidelity of 88%. The nuclear spins have coherence times $\sim$500 times longer than electron spins, and are also much less sensitive to optically-induced decoherence [72], further confirming their suitability as memory qubits. Single-shot readout of a single N nuclear spin with fidelity of 92% has been achieved using a quantum nondemolition measurement scheme [73]. Repetitive readout of the electron spin has been amplified by a factor of ten by using a single nuclear spin as a storage qubit [66].

Additionally, dynamical decoupling can be used to protect the nuclear qubits from decoherence whilst they are not needed for a calculation. Dynamical decoupling reverses the spin precession, refocusing the qubit phase [71]. Dynamical decoupling has been integrated into quantum gates in diamond NV centres at room temperature to protect the information stored in the nuclear spin [74].

Nuclear-electron coupling in silicon

Silicon-based systems provide another promising electron-nuclear spin hybrid quantum computing environment. Donors such as ^{31}P act as long-lived nuclear spin qubits, however direct measurement of the nuclear spin state by NMR is difficult. The nuclear spin state can instead be coherently transferred to the donor electron spin by using resonant microwave and radio frequency pulses [75]. Once on the electron spin, the state can be read out using high-fidelity single-shot readout techniques [76], first achieved by Morello *et al.* [77]. Electrical single-shot readout of a single ^{31}P nuclear spin with fidelity greater than 99.8% has since been demonstrated [25].

Spin-optical photon coupling

Solid state spins show promise for scalable quantum computational architectures as many qubits can be integrated onto chips using nanofabrication techniques. However, connecting distant stationary qubits in a quantum network or for the purposes of quantum communication requires flying qubits which can be transferred over long distances. Photons form the ideal flying qubit due to their superb transmission rates and long coherence times.

Several spin-based qubits have spin-dependent optical transitions, where the light-matter coupling is dependent on the spin state and on the photon polarisation or frequency [78]. This requires the spin qubit to have a spin-degenerate ground state and an optical transition to an excited state with strong spin-orbit coupling [78]. Two such candidate systems are quantum dots and NV centres in diamond, and we provide an overview of their properties here.

Optically active quantum dots

Quantum dots were used in very early quantum computing proposals [37]. They are highly tunable and can be readily integrated into nanoscale devices. InGaAs quantum

dots in GaAs are the most promising optically active quantum dots since it is possible to confine both electrons and holes simultaneously and obtain discrete optical spectra [78]. Photons generated by different quantum dots are highly indistinguishable, as demonstrated by interference experiments [79, 80].

If we apply a magnetic field parallel to the sample surface, the two spin states are both coupled equally to the two excited states with polarisation-dependent transitions. This can be used to initialise, manipulate and readout the spin state by use of resonant optical pulses which address a single spin state [78]. Li *et al.* [81] first demonstrated an all-optical two-bit quantum gate in a quantum dot, whilst Press *et al.* demonstrated complete coherent control of a single quantum dot spin using ultrafast optical pulses [82].

Another important prerequisite is the ability to create entanglement between a quantum dot spin and a single photon; this has been realised [83–85]. The fidelity of entangled spin-photon pairs can exceed 90% [86]. This entanglement holds promise for quantum teleportation and quantum communication. A recent quantum teleportation experiment [87] generated a single photon in superposition by exciting a quantum dot, then created an entangled spin-photon state in a second dot located 5 m away and interfered the two photons to teleport the quantum information. This has paved the way for the generation of entanglement between two distant quantum dot spins using single-photon interference [88].

Spin-photon coupling in NV centres

NV centre electron spins can be controlled optically. Initialisation and spin readout can be achieved using off-resonant or resonant optical pulses [78]; the fidelity of off-resonant initialisation is thought to be limited to around 90%, whereas resonant initialisation can produce fidelities of at least 99.7% [89]. The coupling between nuclear and electronic spins in NV centres can also be exploited to provide optical initialisation and readout of nearby nuclear spins [73, 90, 91]. The nuclear spin can be protected from

decoherence during optical readout of the electron spin state [72]. Full optical coherent control of the electron spin has also been demonstrated by applying two lasers of different frequencies to the NV centre and varying the phase between them [92, 93].

Photon-coupled NV centres offer a promising avenue for long-distance quantum communication. Togan *et al.* demonstrated entanglement between a single photon polarisation state and an NV electron spin [94]. Since then, photons have been used to remotely entangle electrons in two remote NV centres [95] and thus demonstrate loophole-free Bell inequality violation [16]. Photon-mediated entanglement of remote NV centres has been used to teleport quantum states between NV centres separated by 3 metres [96].

Chapter 3

Open Quantum Systems

The universe has to move forward. Pain and loss, they define us as much as happiness or love. Whether it's a world, or a relationship... Everything has its time. And everything ends.

Sarah Jane Smith, *Doctor Who: School Reunion*

In Chapter 2 we saw that coherences are vital for quantum computation, and that systems undergoing decoherence are most conveniently described using density matrices. Here we look the time evolution of density matrices, both for closed quantum systems and for open quantum systems. This provides a mathematical framework for describing decoherence that will be used extensively in later Chapters.

3.1 Closed and open quantum systems

3.1.1 Closed quantum systems

A closed quantum system is one that does not interact with any external influences – it exists in a perfect bubble away from the rest of the Universe. The dynamics of the system's state vector are determined by the Schrödinger equation [97]:

$$i\frac{d}{dt}|\psi(t)\rangle = H|\psi(t)\rangle, \tag{3.1}$$

where H is the (in general time-dependent) system Hamiltonian and from here onwards we have set Planck's constant $\hbar = 1$.

The Schrödinger equation can be used to derive an equation of motion for the density matrix, known as the Liouville-von Neumann equation [97]:

$$\frac{d}{dt}\rho(t) = -i[H, \rho(t)], \tag{3.2}$$

where $[A, B] \equiv AB - BA$ is the commutator of A and B. Equation 3.2 is an example of a quantum master equation – a set of differential equations, one for each entry of the density matrix. Solving these would provide us with the full dynamics of each density matrix element.

3.1.2 Open quantum systems

An open quantum system is one that interacts with an external environment. If the energy level spacing of that environment tends to zero then it is called a reservoir; if that reservoir is in thermal equilibrium it is a bath [97]. A schematic representation of an open quantum system is shown in Figure 3.1. The total Hilbert space available is the

tensor product of the system and environmental Hilbert spaces [97].

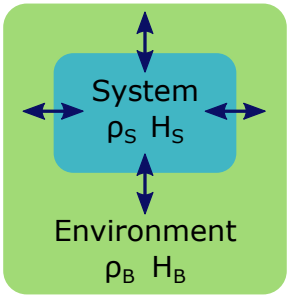

Figure 3.1: Representation of an open quantum system [97]. The total system-bath density matrix is denoted ρ.

The Born-Markov approximations

The Born and Markov approximations are frequently made when investigating open quantum systems. To make the Born approximation, first we assume that the system and environment are weakly coupled so that the system only weakly influences the environment (this is known as the weak-coupling approximation). The environment's density matrix is negligibly affected by the interaction with the system, such that the total density matrix can be approximated as a tensor product [97]:

$$\rho(t) \approx \rho_S(t) \otimes \rho_B. \tag{3.3}$$

In general, when a system is coupled to an environment, its future state can depend not only on its current state, but also on past states since information that was transferred to the environment at earlier times can be transferred back to the system. The Markov approximation assumes that the time evolution of the system is only dependent upon the current state of the system, and not on the system's history.

Applying the Markov approximation to a quantum master equation results in a time local equation. This is valid so long as timescale of environmental correlations is short

compared to the relaxation time of the system [97]. Once the Markov approximation is applied, the resulting description has a coarse-grained timescale, such that the environmental correlations cannot be resolved [98].

The environment

The environment can often be effectively modelled by a system of free bosonic or fermionic modes. Each mode k has frequency ω_k, leading to the free environmental Hamiltonian:

$$H_B = \sum_k \omega_k b_k^\dagger b_k. \tag{3.4}$$

Bosonic operators satisfy $[b_k, b_{k'}^\dagger] = \delta_{k,k'}$, whereas fermionic operators satisfy $\{b_k, b_{k'}^\dagger\} = \delta_{k,k'}$ (where $\{A, B\} \equiv AB + BA$ is the anticommutator).

Each environmental mode k couples to the system with coupling strength c_k, so that the environment's influence on the system can be expressed using the spectral density:

$$J(\omega) \equiv \pi \sum_k |c_k|^2 \delta(\omega - \omega_k). \tag{3.5}$$

The spectral density is the system-environment coupling strength weighted by the environmental density of states. A high value of $J(\omega)$ indicates that it is favourable for the system to exchange ω of energy with the environment.

As a reservoir has zero level spacing, its spectral density contains a smooth continuum of frequency modes, such that Equation 3.5 is replaced by:

$$J(\omega) = \pi |c(\omega)|^2 g(\omega), \tag{3.6}$$

where $g(\omega)$ is the density of states of the reservoir.

We will also make use of the property that for any function $f(k)$:

$$\pi \sum_k |c_k|^2 f(\omega_k) = \int_0^\infty d\omega J(\omega) f(\omega). \tag{3.7}$$

The Markov approximation can also be thought of in terms of requirements on the spectral density. Requiring that the environment correlations decay over a short range of times is equivalent to demanding that a broad range of environmental frequencies are perturbed. The most Markovian environment is $J(\omega) =$ constant, which Fourier transforms to a delta function in the time domain.

Types of spectral density

The spectral density is only ever defined for positive frequencies, and any physical spectral density should tend to zero at high frequency, otherwise high-frequency modes lead to a renormalisation of physical system parameters [97]. We are most interested in the low-frequency behaviour of the spectral density, as these are often the frequencies that the system samples. At low frequencies, the behaviour of $J(\omega)$ can be modelled as a power law:

$$J(\omega) \propto \omega^s, \tag{3.8}$$

where $s \in \mathbb{R}^+$ is a constant. The value of s determines the type of environment [99]:

$$0 \leq s < 1 : \text{subohmic}, \tag{3.9}$$

$$s = 1 : \text{Ohmic}, \tag{3.10}$$

$$s > 1 : \text{superohmic}. \tag{3.11}$$

An Ohmic spectral density gives rise to a frequency-independent system damping rate [97]. To obtain the correct high-frequency behaviour of the spectral density, a cutoff function is needed. Two main cutoff functions will be used throughout this Thesis – the

Lorentzian [97] and the exponential cutoff. The Ohmic spectral density with Lorentzian cutoff has the form:

$$J(\omega) \propto \frac{\omega\omega_c^2}{(\omega-\Omega)^2+\omega_c^2}, \tag{3.12}$$

where Ω is the centre of the Lorentzian peak and ω_c is the high frequency cutoff. The Ohmic spectral density with exponential cutoff and peak frequency ω_c has the form:

$$J(\omega) \propto \frac{\omega}{\omega_c} e^{1-\omega/\omega_c}. \tag{3.13}$$

3.2 Relaxation and dephasing

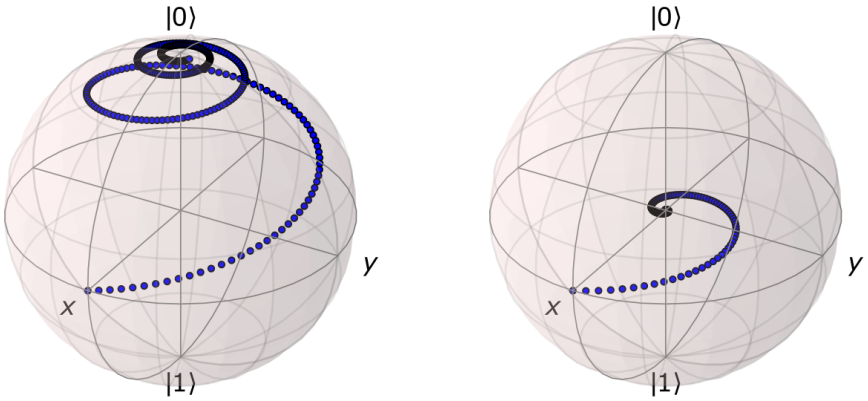

Figure 3.2: A qubit on the Bloch sphere is put into an initial state $\frac{1}{\sqrt{2}}(|0\rangle + |1\rangle)$ and subjected to decoherence. Left: the qubit relaxes via T_1 processes, losing both energy and phase information. Eventually the qubit comes into thermal equilibrium with the environment (which is at zero temperature in this case). Right: a qubit undergoes T_2 dephasing, losing phase information but not energy to the environment.

Environmental decoherence comes in two main forms: relaxation and dephasing. During relaxation, the system exchanges energy with the environment and eventually they come into thermal equilibrium on a timescale T_1. On the other hand, if the system's energy is conserved and only phase information is lost, then the system is said to have undergone dephasing. Dephasing occurs on a timescale $T_2 \leq 2T_1$ and is responsible

for the loss of coherences. Relaxation times are typically much longer than dephasing times, so efforts are focused on controlling dephasing processes [31]. Figure 3.2 shows the effect of relaxation and dephasing on a qubit on the Bloch sphere.

3.3 Quantum master equations and Lindblad form

The density matrix of an open quantum system evolves not as Equation 3.2, but via the *quantum master equation*, which describes the time evolution of the reduced system density matrix $\rho_S(t)$ [97]. The most general form of time local quantum master equation which guarantees a physical density matrix is the *Lindblad equation* [11]:

$$\frac{d}{dt}\rho_S(t) = -i[H_S, \rho_S(t)] + \sum_n \lambda_n \mathcal{D}[L_n]\rho_S(t), \tag{3.14}$$

where the first term on the right hand side represents the unitary dynamics caused by the system Hamiltonian, and:

$$\mathcal{D}[L_n]\rho_S(t) \equiv L_n\rho_S(t)L_n^\dagger - \frac{1}{2}\left(L_n^\dagger L_n\rho_S(t) + \rho_S(t)L_n^\dagger L_n\right), \tag{3.15}$$

is known as the *dissipator*. The L_n are Lindblad operators corresponding to allowed decay channels, with corresponding decay rates λ_n. These Lindblad operators (also known as collapse or transition operators) represent system processes; for example, the decay $|\uparrow\rangle \rightarrow |\downarrow\rangle$ is represented by the Lindblad operator $|\downarrow\rangle\langle\uparrow|$. T_2 relaxation processes are described by the σ_z Lindblad operator, whilst T_1 processes are decribed by σ_-, where:

$$\sigma_\pm = \frac{1}{2}(\sigma_x \pm i\sigma_y). \tag{3.16}$$

We will now look at the derivation of the quantum master equation.

3.4 Derivation of the Born-Markov master equation

This derivation follows that outlined in Breuer & Petruccione [97]. We use a general form of the interaction picture Hamiltonian representing a system coupled to a large environment. This is inserted into the Born-Markov master equation to obtain the differential equation describing the system dynamics.

3.4.1 The Hamiltonian

The total Hamiltonian in the Schrödinger picture is composed of a system Hamiltonian H_S, a free bath Hamiltonian H_B and an interaction term H_{SB} which describes the system-bath coupling:

$$H_{Sch} = \underbrace{H_S + H_B}_{H_{0,S}} + H_{SB}. \tag{3.17}$$

An operator in the interaction picture is:

$$A_{Int}(t) = e^{iH_{0,S}t} A_{Sch}(t) e^{-iH_{0,S}t}. \tag{3.18}$$

Assuming $[H_S, H_B] = 0$, the time-dependent interaction picture Hamiltonian is:

$$H_I(t) = e^{iH_S t} e^{iH_B t} H_{SB} e^{-iH_S t} e^{-iH_B t}. \tag{3.19}$$

We can define a bath interaction operator $b(t)$ which describes the environmental part of the interaction picture Hamiltonian. Then the interaction picture Hamiltonian can be written as follows [97]:

$$H_I(t) = \sum_{\omega} e^{-i\omega t} A_\omega \otimes b(t) + e^{i\omega t} A_\omega^\dagger \otimes b^\dagger(t). \tag{3.20}$$

Here ω are the transition frequencies and A_ω are the system operators - these represent

transitions induced by the coupling to the bath. Note that A_ω does not signify that A is explicitly dependent on ω, but rather that the operator A has the frequency ω associated with it. The Lindblad operators satisfy $A_{-\omega} = A_\omega^\dagger$. Additionally, the collapse operators are said to be eigenoperators of H_S [97]:

$$[H_S, A_\omega] = -\omega A_\omega, \tag{3.21}$$

$$[H_S, A_\omega^\dagger] = +\omega A_\omega^\dagger. \tag{3.22}$$

Consequently, the interaction picture Lindblad operators are [97]:

$$e^{iH_S t} A_\omega e^{-iH_S t} = e^{-i\omega t} A_\omega, \tag{3.23}$$

$$e^{iH_S t} A_\omega^\dagger e^{-iH_S t} = e^{+i\omega t} A_\omega^\dagger. \tag{3.24}$$

3.4.2 The Markovian quantum master equation

To derive the Markovian master equation, we follow Breuer & Petruccione [97], starting with the Liouville-von Neumann equation for the interaction-picture density matrix (Equation 3.2):

$$\frac{d}{dt}\rho(t) = -i[H, \rho(t)], \tag{3.25}$$

which can be expressed as the integral:

$$\rho(t) = \rho(0) - i\int_0^t ds[H_I(s), \rho(s)]. \tag{3.26}$$

Next we substitute the integral form into the differential form and trace out the environmental modes:

$$\frac{d}{dt}\rho_S(t) = -\int_0^t ds\, \mathrm{Tr}_B \left[H_I(t), [H_I(s), \rho(s)]\right]. \tag{3.27}$$

This assumes that $\mathrm{Tr}_B[H_I(t), \rho(0)] = 0$.

Next we apply the Born-Markov approximations (Section 3.1.2). Applying the Born approximation (Equation 3.3) allows us to separate the system and environmental density matrices:

$$\frac{d}{dt}\rho_S(t) = -\int_0^t ds\, \mathrm{Tr}_B[H_I(t), [H_I(s), \rho_S(s) \otimes \rho_B]]. \tag{3.28}$$

This can be made time-local by replacing $\rho_S(s)$ with $\rho_S(t)$ inside the integrand, meaning that the evolution of the state now only depends on the current state of the system, not on any past states. The result is the Redfield equation [100]. Then we substitute s by $t - s$ in the integrand:

$$\frac{d}{dt}\rho_S(t) = -\int_0^t ds\, \mathrm{Tr}_B[H_I(t), [H_I(t-s), \rho_S(t) \otimes \rho_B]]. \tag{3.29}$$

Now s can be understood as the length of history that we account for (the 'memory effect'). Once the environmental correlations decay, there is no memory. By making the Markov approximation, we assume that these environmental correlations decay quickly in comparison to the relaxation time of the system, so that the integrand vanishes quickly for large s. Therefore, we can extend the upper integral limit to infinity and obtain the Markovian quantum master equation:

$$\frac{d}{dt}\rho_S(t) = -\int_0^\infty ds\, \mathrm{Tr}_B[H_I(t), [H_I(t-s), \rho_S(t) \otimes \rho_B]]. \tag{3.30}$$

3.4.3 Generating master equations

We can now find the Markovian master equation in terms of transition operators by substituting Equation 3.20 into Equation 3.30 and expanding:

$$\begin{aligned}\frac{d}{dt}\rho_S(t) = \int_0^\infty ds\, \mathrm{Tr}_B \sum_{\omega\omega'} \Bigg(&\Big(e^{-i\omega(t-s)} A_\omega \otimes b(t-s) + e^{i\omega(t-s)} A_\omega^\dagger \otimes b^\dagger(t-s)\Big) \\ &\times \rho_S(t)\rho_B \Big(e^{-i\omega' t} A_{\omega'} \otimes b(t) + e^{i\omega' t} A_{\omega'}^\dagger \otimes b^\dagger(t)\Big) \\ &- \Big(e^{-i\omega t} A_\omega \otimes b(t) + e^{i\omega t} A_\omega^\dagger \otimes b^\dagger(t)\Big) \\ &\times \Big(e^{-i\omega'(t-s)} A_{\omega'} \otimes b(t-s) + e^{i\omega'(t-s)} A_{\omega'}^\dagger \otimes b^\dagger(t-s)\Big)\rho_S(t)\rho_B \Bigg) + H.c,\end{aligned} \tag{3.31}$$

where ω counts over the transition frequencies of the system. At this point it is useful to define:

$$\Gamma_\uparrow(\omega) = \int_0^\infty ds e^{-i\omega s}\langle b^\dagger(s)b(0)\rangle, \qquad \Gamma_\downarrow(\omega) = \int_0^\infty ds e^{i\omega s}\langle b(s)b^\dagger(0)\rangle. \tag{3.32}$$

These take the form of (complex) absorption and emission rates respectively and will be discussed in more detail in Section 3.4.4. We note that the reservoir correlation function $\langle b^\dagger(t)b(t-s)\rangle$ is homogeneous in time [97]. We use $\mathrm{Tr}_R(\rho_R X) = \langle X\rangle$, insert $\Gamma(\omega)$ into Equation 3.31, and interchange ω and ω' in the middle two lines of Equation 3.31. Finally we swap $\omega \leftrightarrow -\omega$ (noting that $A_{-\omega} = A_\omega^\dagger$) to obtain the Markovian quantum

master equation in the interaction picture:

$$\begin{aligned}\frac{d}{dt}\rho_S(t) = \sum_{\omega\omega'} e^{i(\omega-\omega')t}\Big(&\Gamma_\uparrow(\omega)\Big(A^\dagger_\omega\rho_S(t)A_{\omega'} - A_{\omega'}A^\dagger_\omega\rho_S(t)\Big)\\ &+\Gamma^*_\uparrow(\omega')\Big(A^\dagger_\omega\rho_S(t)A_{\omega'} - \rho_S(t)A_{\omega'}A^\dagger_\omega\Big)\\ &+\Gamma_\downarrow(\omega')\Big(A_{\omega'}\rho_S(t)A^\dagger_\omega - A^\dagger_\omega A_{\omega'}\rho_S(t)\Big)\\ &+\Gamma^*_\downarrow(\omega)\Big(A_{\omega'}\rho_S(t)A^\dagger_\omega - \rho_S(t)A^\dagger_\omega A_{\omega'}\Big)\Big).\end{aligned} \tag{3.33}$$

Transforming master equations between the interaction and Schrödinger pictures

Here we describe the relationship between the master equation in the interaction and the Schrödinger pictures. To do this, we distinguish between the system density matrix $\rho_S(t)$ in these two pictures using $\rho^I_S(t)$ and $\rho^{Sch}_S(t)$ respectively. The superscripts are dropped in the rest of the Thesis and the picture used is defined explicitly for clarity. To transform from the interaction picture back to the Schrödinger picture, we recall that when we derived the master equation, we defined an interaction picture Hamiltonian $H_I(t)$ (Equation 3.19). Using this, we find that the system density operator in the interaction picture is:

$$\rho^I_S(t) = e^{iH_St}\rho^{Sch}_S(t)e^{-iH_St}. \tag{3.34}$$

Take the derivative of Equation 3.34:

$$\begin{aligned}\frac{d}{dt}\rho^I_S(t) &= iH_Se^{iH_St}\rho^{Sch}_S(t)e^{-iH_St} + e^{iH_St}\frac{d}{dt}\Big(\rho^{Sch}_S(t)\Big)e^{-iH_St} - ie^{iH_St}\rho^{Sch}_S(t)H_Se^{-iH_St},\\ &= e^{iH_St}\Big(i[H_S,\rho^{Sch}_S(t)] + \frac{d}{dt}\rho^{Sch}_S(t)\Big)e^{-iH_St}.\end{aligned} \tag{3.35}$$

The interaction picture quantum master equation (Equation 3.33) can be written in

the form:

$$\frac{d}{dt}\rho_S^I(t) = \sum_{\omega\omega'} e^{i(\omega'-\omega)t} \underbrace{\sum_n \gamma_n(\omega,\omega')\hat{O}_{\omega,\omega',n}}_{\mathcal{D}_{\omega,\omega'}[\rho_S^I(t)]}, \tag{3.36}$$

where $\hat{O}_{\omega,\omega',n}$ is some linear combination of A_ω, $A_{\omega'}^\dagger$ and $\rho_S^I(t)$.

Once transformed back into the Schrödinger picture, the terms represented by $e^{i(\omega'-\omega)t}\hat{O}_{\omega,\omega',n}$ in Equation 3.36 become terms like:

$$\begin{aligned} &e^{-i\omega t}A_\omega e^{iH_S t}\rho_S^{Sch}(t)e^{-iH_S t}e^{i\omega' t}A_{\omega'}^\dagger, \\ &e^{i\omega' t}A_{\omega'}^\dagger e^{-i\omega t}A_\omega e^{iH_S t}\rho_S^{Sch}(t)e^{-iH_S t}. \end{aligned} \tag{3.37}$$

Now we use the transition operator properties in Equation 3.24, so the terms in Equation 3.37 become:

$$\begin{aligned} &e^{iH_S t}A_\omega \rho_S^{Sch}(t)A_{\omega'}^\dagger e^{-iH_S t}, \\ &e^{iH_S t}A_{\omega'}^\dagger A_\omega \rho_S^{Sch}(t)e^{-iH_S t}. \end{aligned} \tag{3.38}$$

The master equation becomes:

$$\frac{d}{dt}\rho_S^I(t) = \sum_{\omega,\omega'} e^{i(\omega'-\omega)t}\mathcal{D}_{\omega,\omega'}[\rho_S^I(t)] = e^{iH_S t}\sum_{\omega,\omega'}\mathcal{D}_{\omega,\omega'}[\rho_S^{Sch}(t)]e^{-iH_S t}. \tag{3.39}$$

The Schrödinger picture master equation is therefore:

$$\frac{d}{dt}\rho_S^{Sch}(t) = -i[H_S,\rho_S^{Sch}(t)] + \sum_{\omega,\omega'}\mathcal{D}_{\omega,\omega'}[\rho_S^{Sch}(t)]. \tag{3.40}$$

3.4.4 The (complex) rates

To simplify the reservoir correlation function, we use the following results for bulk photon modes in a thermal state:

$$\begin{aligned}\langle b_k b_{k'}\rangle &= \langle b_k^\dagger b_{k'}^\dagger\rangle = 0,\\ \langle b_k^\dagger b_{k'}\rangle &= \delta_{kk'} n_k,\\ \langle b_k b_{k'}^\dagger\rangle &= \delta_{kk'}(n_k+1).\end{aligned} \tag{3.41}$$

The absorption rate $\Gamma_\uparrow(\omega)$ is:

$$\begin{aligned}\Gamma_\uparrow(\omega) &= \int_0^\infty ds e^{-i\omega s}\langle b^\dagger(s)b(0)\rangle,\\ &= \int_0^\infty ds e^{-i\omega s}\sum_k c_k^2 n_k e^{i\omega_k s},\\ &= \sum_k c_k^2 n_k\left(\pi\delta(\omega-\omega_k) - i\mathcal{P}\frac{1}{\omega-\omega_k}\right).\end{aligned} \tag{3.42}$$

Similarly the emission rate is:

$$\Gamma_\downarrow(\omega) = \sum_k c_k^2(n_k+1)\left(\pi\delta(\omega-\omega_k) + i\mathcal{P}\frac{1}{\omega-\omega_k}\right). \tag{3.43}$$

Here we have used the standard formula [97]:

$$\int_0^\infty ds e^{-i\varepsilon s} = \pi\delta(\varepsilon) - i\mathcal{P}\frac{1}{\varepsilon}, \tag{3.44}$$

where $\mathcal{P}$ represents the Cauchy principal value.

By using Equation 3.7, we can now convert the sums into integrals involving the

spectral density:

$$\Gamma_{\uparrow}(\omega) = J(\omega)n(\omega) + \frac{i}{\pi}\mathcal{P}\int_0^\infty \frac{J(\phi)n(\phi)}{\phi-\omega}d\phi,$$

$$\Gamma_{\downarrow}(\omega) = J(\omega)[n(\omega)+1] - \frac{i}{\pi}\mathcal{P}\int_0^\infty \frac{J(\phi)[n(\phi)+1]}{\phi-\omega}d\phi, \tag{3.45}$$

where $n(\omega)$ is the Bose Einstein occupation function. Note that the spectral density is only non-zero for positive frequencies, so the integrals are one-sided.

The first term in these expressions is real and corresponds to the rate of the transition with frequency ω. The second term is entirely imaginary, and for a master equation in Lindblad form corresponds to a Lamb shift. The complex nature of the rates and their significance will be explored more thoroughly in Section 3.4.5.

When the environment is at zero temperature, the expressions simplify (assuming $J(\omega<0)=0$):

$$\Gamma_{\downarrow}(\omega) = J(\omega) + \frac{i}{\pi}\mathcal{P}\int_0^\infty \frac{J(\phi)}{\omega-\phi}d\phi. \tag{3.46}$$

The absorption rate $\Gamma_{\uparrow}(\omega)=0$ at zero temperature as there are no excitations in the environment to be absorbed by the system.

3.4.5 Secularisation and Lindblad form

The secular approximation

It is possible to view the master equation (Equation 3.33) as a grid of terms, each term with a different combination of ω and ω'. The diagonal terms each represent a transition between two different states of a multi-level system, where $\omega=\omega'$ is the transition frequency. Each of the off-diagonal elements represents the interference between two different transitions.

Equation 3.33 is a quantum master equation, but at present it doesn't guarantee physical behaviour of the density matrix. For this, it must be in Lindblad form, and to achieve this, we must make one more approximation – the secular approximation. The non-secular quantum master equation in the interaction picture is of the form:

$$\frac{d}{dt}\rho_S(t) = \sum_{\omega,\omega'} e^{i(\omega'-\omega)t} f(\omega,\omega'), \tag{3.47}$$

where the rates and transition operators have been bundled up into the function $f(\omega,\omega')$ for convenience.

To make the secular approximation, we assume that for $\omega \neq \omega'$, the exponential term in Equation 3.47 will oscillate rapidly and average to zero. This is valid so long as the frequency differences between different transitions are large compared to the inverse of the system relaxation time τ_R, i.e. $|\omega' - \omega| \gg \tau_R^{-1}$ [97]. As we shall see in future Chapters, the secular approximation is not appropriate when the transitions are closely spaced.

By making the secular approximation on Equation 3.33 and splitting the reservoir correlation function $\Gamma(\omega)$ into real and imaginary parts $\Gamma(\omega) = \Gamma'(\omega) + i\Gamma''(\omega)$, we obtain the quantum master equation in Lindblad form:

$$\frac{d}{dt}\rho_S(t) = \sum_{\omega} \left(2\Gamma'_{\downarrow}(\omega)\mathcal{D}[A_\omega]\rho_S(t) + 2\Gamma'_{\uparrow}(\omega)\mathcal{D}[A_\omega^\dagger]\rho_S(t) - i[H_{LS},\rho_S(t)]\right), \tag{3.48}$$

where the dissipator $\mathcal{D}[L]\rho(t)$ is defined in Equation 3.15 and the Lamb shift Hamiltonian is $H_{LS} = \Gamma''_{\downarrow}(\omega)A_\omega^\dagger A_\omega + \Gamma''_{\uparrow}(\omega)A_\omega A_\omega^\dagger$. In the secular quantum master equation, the real parts of $\Gamma(\omega)$ exactly correspond to the transition rates, and the imaginary parts to the Lamb shift.

The secular approximation is typically justified in quantum optical systems, where the frequency differences between different transitions are much larger than typical relaxation

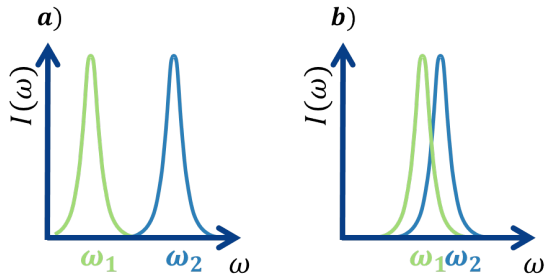

Figure 3.3: Sample emission spectra $I(\omega)$ from two different system transitions with central frequencies ω_1 and ω_2. The transition linewidth is the relaxation rate of the open system (here assumed equal for both transitions). If the linewidths are smaller than the transition frequency difference (as in a)), the transitions are separable and the secular approximation is valid. However, if the spectra from multiple transitions overlap as shown in b), the transitions are not separable. Applying the secular approximation in this case would discard coherent evolution terms.

rates. The transitions are therefore separable – each transition has its own Lindblad operator and associated frequency. If the photon frequency from such a transition is measured, it is possible to identify which transition has taken place (see Figure 3.3).

Non-secular master equations in Lindblad form

Applying the secular approximation indiscriminately causes the loss of coherent oscillation terms from the master equation [101]. The non-secular master equations do not guarantee positivity of the density matrix, however if the underlying microscopic derivation is consistent, then they will still produce physical results [101].

In the absence of secularisation, the interaction picture master equation (Equa-

tion 3.33) can be written:

$$\begin{aligned}\frac{d}{dt}\rho_S(t) = \sum_{\omega,\omega'} e^{i(\omega-\omega')t}\Big(&\big(\bar{\Gamma}'_{\downarrow}(\omega,\omega') + i\delta\Gamma''_{\downarrow}(\omega,\omega')\big)\big(2A_{\omega'}\rho_S(t)A^\dagger_\omega - \{A^\dagger_\omega A_{\omega'}, \rho_S(t)\}\big) \\ &+\big(\bar{\Gamma}'_{\uparrow}(\omega',\omega) + i\delta\Gamma''_{\uparrow}(\omega',\omega)\big)\big(2A^\dagger_\omega\rho_S(t)A_{\omega'} - \{A_{\omega'}A^\dagger_\omega, \rho_S(t)\}\big) \\ &+\big(\delta\Gamma'_{\downarrow}(\omega,\omega') + i\bar{\Gamma}''_{\downarrow}(\omega,\omega')\big)[A^\dagger_\omega A_{\omega'}, \rho_S(t)] \\ &+\big(\delta\Gamma'_{\uparrow}(\omega',\omega) + i\bar{\Gamma}''_{\uparrow}(\omega',\omega)\big)[A_{\omega'}A^\dagger_\omega, \rho_S(t)]\Big),\end{aligned} \tag{3.49}$$

where:

$$\bar{\Gamma}(\omega,\omega') = \frac{\Gamma(\omega') + \Gamma(\omega)}{2}, \qquad \delta\Gamma(\omega,\omega') = \frac{\Gamma(\omega') - \Gamma(\omega)}{2}. \tag{3.50}$$

The upper line on the right hand side of Equation 3.49 is dissipative and must be diagonalised in ω in order to convert to Lindblad form and find the rates. These rates are complex, containing a real part from the spectral density and the Bose Einstein occupation function, as well as an imaginary part from the Cauchy integral that would only be found in the Lamb shift under secularisation (Equation 3.45).

Note that the operators A_ω must be orthonormal in order to convert the dissipator to Lindblad form; this corresponds to requiring that $\mathrm{Tr}[A^\dagger_\omega A_{\omega'}] = \delta_{\omega,\omega'}$ [97]. Once diagonalised, there is no guarantee that all rates will be positive – some processes may appear to have a negative rate and this would lead to non-positive evolution [102].

The behaviour of the system over short timescales cannot be resolved since the Markov approximation causes a coarse-graining such that the environmental correlations cannot be resolved. However we can assess whether the long-time behaviour of the system violates physicality; to do this, we turn to the Liouvillian.

3.4.6 The Liouvillian

The Liouvillian superoperator is defined as [97]:

$$\frac{d}{dt}\boldsymbol{\rho}(t) = \mathcal{L}\boldsymbol{\rho}(t), \tag{3.51}$$

where $\boldsymbol{\rho}(t)$ is comprised of the elements of the density matrix arranged into a vector. The eigenvalues of the Liouvillian are denoted $\{\lambda_i\}$ and the eigenvectors are denoted $\{\boldsymbol{v}_i\}$:

$$\begin{aligned} \mathcal{L}\boldsymbol{v}_i &= \lambda_i \boldsymbol{v}_i, \\ \Rightarrow \frac{d}{dt}\boldsymbol{v}_i(t) &= \lambda_i \boldsymbol{v}_i(t), \\ \Rightarrow \boldsymbol{v}_i(t) &= e^{\lambda_i t}\boldsymbol{v}_i(0). \end{aligned} \tag{3.52}$$

Since the eigenvectors form a complete basis, any density matrix vector can be written as a linear combination of the Liouvillian eigenvectors:

$$\boldsymbol{\rho}(t) = \sum_i c_i \boldsymbol{v}_i(t) = \sum_i c_i e^{\lambda_i t}\boldsymbol{v}_i(0). \tag{3.53}$$

Note that the eigenvectors are associated with matrices which do not necessarily have unit trace and may be non-Hermitian, and as such are not valid density matrices in themselves. There should always be at least one zero eigenvalue; one zero eigenvalue should have an associated eigenvector that possesses unit trace. All other eigenvectors should have zero trace.

In general we may write:

$$\text{For} \begin{cases} \mathbb{R}[\lambda_i] < 0 & \text{the state } \boldsymbol{v}_i(t) \text{ decays.} \\ \mathbb{R}[\lambda_i] = 0 & \text{the state } \boldsymbol{v}_i \text{ is a steady state.} \\ \mathbb{R}[\lambda_i] > 0 & \text{the state } \boldsymbol{v}_i(t) \text{ is amplified.} \end{cases}$$

So any positive eigenvalues of the Liouvillian lead to states that are unphysically amplified. Multiple zero eigenvalues indicate multiple steady states of the system as a result of some symmetry. If all the eigenvalues of the Liouvillian are negative or zero, the long-time behaviour of the system must be physical.

Note that we should look at the Liouvillian in the Schrödinger picture rather than in the interaction picture. This is because the Liouvillian in the interaction picture contains time dependent elements, meaning that we would need to solve:

$$\mathcal{L}(t)\boldsymbol{v}_i(t) = \lambda_i \boldsymbol{v}_i(t). \tag{3.54}$$

However due to the time dependence of the eigenvectors the linear combination:

$$\rho(t) = \sum_i a_i e^{\lambda_i t} \boldsymbol{v}_i(t), \tag{3.55}$$

is not a solution to the equation of motion in the interaction picture.

3.5 Non-Markovianity in open quantum systems

Some quantum many-body models are exactly solvable without use of the Markov approximation – these include the independent boson model [103], which can be used to describe a fixed particle interacting with a set of phonons, and the Tomonaga model, which describes a one dimensional electron gas [104]. However, in general obtaining

dynamics for a non-Markovian system represents a substantial challenge. In this Section we describe some of the most important theoretical techniques for dealing with non-Markovian systems.

Perturbative methods

For a weak system-environment coupling, it is possible to make a perturbative expansion in the system-environment coupling strength, producing a non-Markovian master equation [103]. Crucially in this derivation, when integrating over time the upper limit is not extended to infinity as in Equation 3.30, but remains finite. However it is then necessary to perform the finite-time integral, which can be challenging.

If the system-bath coupling is not necessarily weak, then we must turn to other techniques. The polaron transformed master equation approach [105–110] relies on transforming the Hamiltonian to that of a polaron and separating the static and fluctuating parts of the polaron operators [105]. Perturbation theory is then used on the fluctuating polaron operator terms. This approach remains valid into strong coupling regimes (modelled as multi-phonon effects) [105] so long as the intrasystem coupling is not the largest relevant energy [110]. The polaron master equation which is derived in this technique is Markovian, however recent efforts have been made [110] to consider baths with finite frequency widths which are therefore not strictly Markovian.

Enlarging the system state space

A second approach to dealing with non-Markovian environments involves enlarging the system state space. This can be done by using hierarchical equations of motion [111], or by incorporating a collective environmental degree of freedom within the effective system Hamiltonian [112, 113]. In the case of the former, specific assumptions are made of the environment [111]; in the latter, only the most important environmental modes are treated fully and the full Born-Markov approximation is used on the residual

environmental modes [113].

Path integral techniques

Another class of techniques for dealing with non-Markovian problems are those based on Feynman's path integral formulation of open quantum systems [114, 115]. In the path integral formulation, the probability that a quantum system is in some final state is calculated by summing up all the possible paths from the initial to the final state. The propagator can be discretised and the environmental modes all formally integrated out [116, 117]. Then all of the environmental effects on the system evolution are encapsulated within the discretised Feynman influence functional [116] (note that the Markov approximation has *not* been made here).

In theory, it is possible to compute the time evolution by directly using the discretised influence functional. However the simulation run time grows exponentially with the number of timesteps involved, making long-time evolution infeasible. This can be overcome by assuming a finite memory time [118, 119], whereby only the environmental memory effects that have occurred within the last k_{max} timesteps are taken into account. This finite memory approximation allows system dynamics to be calculated by propagating the Augmented Density Tensor (ADT), a tensor of rank k_{max} [118, 119].

The run time of standard quasi-adiabatic path integral methods still grows exponentially with k_{max}, but with a numerically exact method called TEMPO (Time Evolving Matrix Product Operator) [117], tensor compression techniques allow a linear scaling in many situations. The value of k_{max} can be chosen such that increasing its value has no effect upon the numerical results. In this way, the method is numerically exact.

Single-excitation exact solution

In rare cases, it is possible to deal with non-Markovian problems exactly, without recourse to perturbative techniques or numerical methods. One such case is when the

number of excitations in the system is conserved, so that we may work entirely in the single-excitation subspace [120].This method is described in detail in the following Section.

3.6 An exact approach for open quantum systems

In this Section, we exactly solve a system consisting of a single qubit coupled to a reservoir of independent bosonic modes. For such a system to permit an exact solution, we must work in a Hilbert space which is restructured in order to allow us to solve the equations of motion exactly. We will look at the solution within the single-excitation subspace, which is only valid at zero temperature. Extending this method to finite temperature can be challenging, since one would need to take a temperature-weighted sum over all excitation subspaces. In this Thesis, this exact approach is used at zero temperature to assess the suitability of the Born-Markov approximations for different parameter regimes. Here we outline the general method used by Vacchini & Breuer [120], following the derivation by Wigner & Weisskopf [121].

This derivation concerns the time evolution of a single two level system with splitting ω_0 in contact with a reservoir of bosonic operators with free bath Hamiltonian as given in Equation 3.4. The coupling of a two-level system to a single bosonic mode can be described by the Jaynes-Cummings Hamiltonian:

$$H_{JC} = g(\sigma_+ b + \sigma_- b^\dagger). \tag{3.56}$$

It is worth noting that although the use of the Jaynes-Cummings Hamiltonian is often justified by making the rotating wave approximation (see, for example, Nielsen & Chuang [11]), this is not always necessary. The Jaynes-Cummings model can be obtained without use of the rotating wave approximation in many cases, such as for a two-level system

interacting with a polarised light field, where selection rules can be engineered to suppress any interactions which do not conserve excitation number [122].

Incorporating multiple bath modes into the Jaynes-Cummings Hamiltonian, we get:

$$H_{SB} = \sum_k (g_k \sigma_+ b_k + g_k^* \sigma_- b_k^\dagger). \tag{3.57}$$

We will use this form of system-bath interaction Hamiltonian at multiple points throughout this Thesis.

The Schrödinger equation in the interaction picture is:

$$\frac{d}{dt}|\Psi(t)\rangle = -iH_I(t)|\Psi(t)\rangle, \tag{3.58}$$

where $H_I(t)$ is defined in Equation 3.19. As the interaction Hamiltonian conserves the number of excitations and we are working at zero temperature, the total number of system-bath excitations remains constant. We will work in the one excitation subspace, so that a general state in the interaction picture at time t can be written:

$$|\Psi(t)\rangle = \alpha_1(t)|1\rangle_S \otimes |0\rangle_B + \sum_k \alpha_k(t)|0\rangle_S \otimes |k\rangle_B, \tag{3.59}$$

where $|k\rangle_B$ denotes a single excitation in the kth mode of the bath.

The interaction picture interaction Hamiltonian for a single qubit is:

$$H_I(t) = \sigma_+(t) \otimes b(t) + \sigma_-(t) \otimes b^\dagger(t), \tag{3.60}$$

where the time dependent Pauli operator is:

$$\sigma_\pm(t) = \sigma_\pm e^{\pm i\omega_0 t}, \tag{3.61}$$

and the time dependent bath operator is:

$$b(t) = \sum_k g_k b_k e^{-i\omega_k t}. \tag{3.62}$$

To calculate the master equation for the single excitation subspace, we use:

$$\begin{aligned} b^\dagger(t)|0\rangle &= \sum_k g_k^* e^{i\omega_k t}|k\rangle, \\ b(t)|k\rangle &= g_k e^{-i\omega_k t}|0\rangle. \end{aligned} \tag{3.63}$$

We can now evaluate Equation 3.58, using the form of the interaction picture interaction Hamiltonian given in Equation 3.60:

$$-iH_I(t)|\Psi(t)\rangle = -i\sum_k e^{i(\omega_0-\omega_k)t}\alpha_k(t)g_k|1\rangle_S \otimes |0\rangle_B + e^{i(\omega_k-\omega_0)t}\alpha_1(t)g_k^*|0\rangle_S \otimes |k\rangle_B. \tag{3.64}$$

By comparing coefficients in Equations 3.59 and 3.64, we obtain a pair of coupled differential equations:

$$\frac{d}{dt}\alpha_1(t) = -i\sum_k e^{i(\omega_0-\omega_k)t}\alpha_k(t)g_k \qquad \frac{d}{dt}\alpha_k(t) = -ie^{-i(\omega_0-\omega_k)t}\alpha_1(t)g_k^*. \tag{3.65}$$

We will assume that the environment is initially in the vacuum state, i.e. $\alpha_k(0) = 0$. The integro-differential form of Equation 3.65 is then:

$$\begin{aligned} \alpha_k(t) &= -i\int_0^t g_k^*\alpha_1(t_1)e^{-i(\omega_0-\omega_k)t_1}dt_1, \\ \Rightarrow \frac{d}{dt}\alpha_1(t) &= -\sum_k |g_k|^2 e^{i(\omega_0-\omega_k)t}\int_0^t \alpha_1(t_1)e^{-i(\omega_0-\omega_k)t_1}dt_1. \end{aligned} \tag{3.66}$$

We can define the kernel:

$$K(t-t_1) \equiv \sum_k |g_k|^2 e^{i(\omega_0-\omega_k)(t-t_1)}. \tag{3.67}$$

The integro-differential equation becomes:

$$\frac{d}{dt}\alpha_1(t) = -\int_0^t K(t-t_1)\alpha_1(t_1)dt_1. \tag{3.68}$$

Using Equation 3.7, we can express $K(t)$ in terms of the spectral density $J(\phi)$:

$$K(t) = \frac{1}{\pi}\int_{-\infty}^{\infty} d\phi J(\phi) e^{i(\omega_0-\phi)t}. \tag{3.69}$$

3.6.1 Laplace transform method

To progress further from Equation 3.69, it is necessary to choose a form of the spectral density. We would then insert the spectral density into Equation 3.69 and solve to find the kernel. The kernel is then inserted into Equation 3.68 and solved to find the system time evolution.

Another method which is often easier numerically is to use Laplace transforms. The definition of a Laplace transform for arbitrary function $F(t)$ is:

$$\tilde{F}(s) = \int_0^{\infty} dt e^{-st} F(t). \tag{3.70}$$

First we Laplace transform Equations 3.65:

$$\begin{aligned} s\tilde{\alpha}_1(s) - \alpha_1(0) &= -i\sum_k g_k \int_0^{\infty} dt \alpha_k(t) e^{(-s+i(\omega_0-\omega_k))t}, \\ s\tilde{\alpha}_k(s) &= -ig_k^* \int_0^{\infty} dt \alpha_1(t) e^{(-s-i(\omega_0-\omega_k))t}. \end{aligned} \tag{3.71}$$

These can be restated as:

$$s\tilde{\alpha}_1(s) - \alpha_1(0) = -i\sum_k g_k\tilde{\alpha}_k(s - i(\omega_0 - \omega_k)), \tag{3.72}$$

$$s\tilde{\alpha}_k(s) = -ig_k^*\tilde{\alpha}_1(s + i(\omega_0 - \omega_k)). \tag{3.73}$$

Relabel $s \to s - i(\omega_0 - \omega_k)$ in Equation 3.73:

$$\begin{aligned}(s - i(\omega_0 - \omega_k))\tilde{\alpha}_k(s - i(\omega_0 - \omega_k)) &= -ig_k^*\tilde{\alpha}_1(s),\\ \Rightarrow \tilde{\alpha}_k(s - i(\omega_0 - \omega_k)) &= \frac{-ig_k^*\tilde{\alpha}_1(s)}{s - i(\omega_0 - \omega_k)}.\end{aligned} \tag{3.74}$$

Combine Equations 3.72 and 3.74:

$$s\tilde{\alpha}_1(s) - \alpha_1(0) = -\sum_k |g_k|^2 \frac{\tilde{\alpha}_1(s)}{s - i(\omega_0 - \omega_k)}. \tag{3.75}$$

Using Equation 3.7, we can turn the sum in Equation 3.75 into an integral:

$$\tilde{\alpha}_1(s)\big(s + f(s - i\omega_0)\big) = \alpha_1(0), \tag{3.76}$$

where we have defined:

$$f(s) \equiv \sum_k \frac{|g_k|^2}{s + i\omega_k} = \frac{1}{\pi}\int_0^\infty d\nu \frac{J(\nu)}{s + i\nu}. \tag{3.77}$$

By combining Equations 3.73 and 3.76, we obtain:

$$\tilde{\alpha}_k(s) = -\frac{ig_k^*}{s}\frac{\alpha_1(0)}{s + i(\omega_0 - \omega_k) + f(s - i\omega_k)}. \tag{3.78}$$

To progress further, we would need to combine the Laplace transformed coefficients to find the expression of interest (e.g. ground state coherences), and then inverse Laplace

transform the result. This approach will be used in Chapter 4, where we will also explore its limitations.

Chapter 4

The Coupled Nuclear-Electron Spin System – Zero Temperature

Let me also remind you that zero, like all of mathematics, is fictional and an idealization. It is impossible to reach absolute zero temperature or to get perfect vacuum. Luckily, mathematics is a fairyland where ideal and fictional objects are possible.

Doron Zeilberger

In Chapter 2 we saw that many promising quantum information architectures rely on hybrid systems, and that the different components of a hybrid system often have differing energy scales. Here we show that these systems can be exploited to provide coherence protection. We look at a coupled electron-nuclear-qubit system at zero temperature using both an exact solution and Born-Markov master equations, using techniques covered in Chapter 3.

4.1 System and motivations

In Chapter 3 we saw that a single quantum system weakly coupled to a large environment decoheres, losing phase information to its surroundings. One interpretation of this is that the environment makes a measurement of the quantum system. In hybrid systems, different parts of the system often have different energy scales, and can couple to the environment with different coupling strengths. If the environmental coupling of one part is much smaller than that of another part, the environment can be thought of as having made a partial measurement of the system. This can enable some system coherences to remain protected even as other parts of the system decohere.

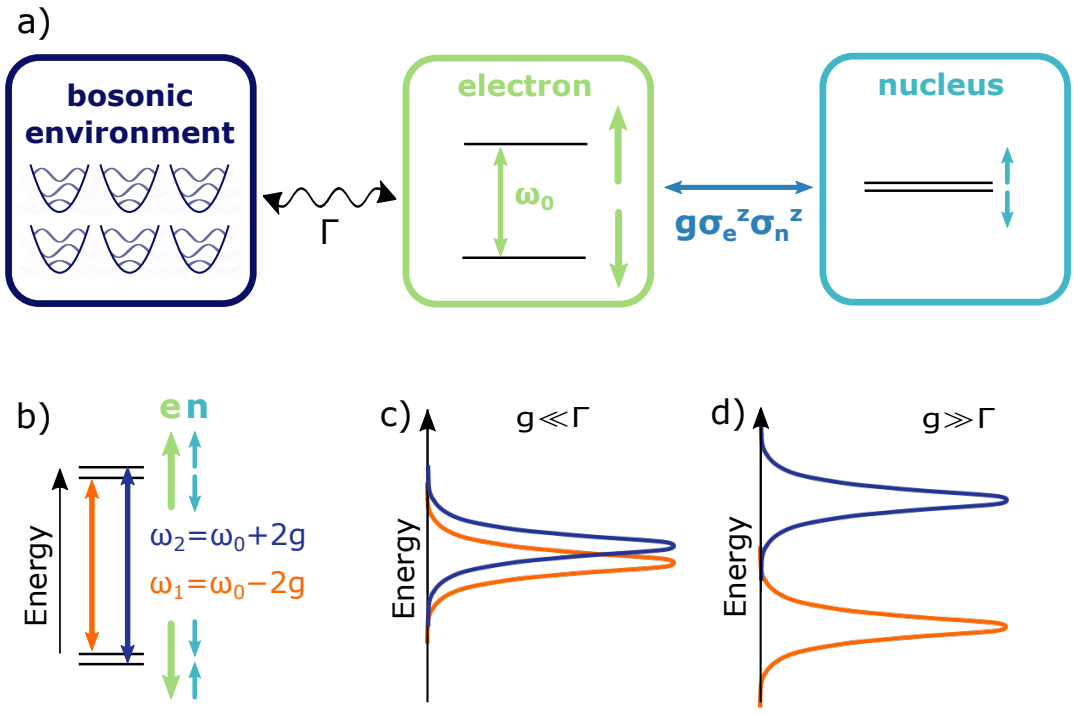

Figure 4.1: a) A hybrid system consisting of an electron spin coupled to a spin-$1/2$ nucleus. The electron has Zeeman splitting of ω_0 and the spin-spin coupling strength is g. The electron is also coupled to a bosonic environment. b) The eigenenergies and allowed transitions of the composite system. c) Small hyperfine coupling causes the transitions to overlap, allowing nuclear coherences to survive. d) Increasing the hyperfine coupling allows the two transitions to be spectrally resolved, and nuclear coherences are lost.

Here we investigate coherence protection in a coupled electron-nuclear spin system (Figure 4.1), but this theory could apply to any coupled hybrid system with differing energy scales.

Electron spin qubits have much shorter coherence times than nuclear spin qubits (Chapter 2), so we will use a simplified description whereby the electron spin interacts with a bosonic environment, but the nuclear spin interacts only with the electron (Figure 4.1 a)). Additionally, the nuclear spin magnetic moment is much smaller than that of the electronic spin, so we ignore the nuclear Zeeman splitting.

Whenever two qubits with distinct energy scales are coupled together, there are four resultant eigenenergies – two closely spaced pairs separated from each other by a large energy gap (Figure 4.1 b)). There are two possible transitions corresponding to electron decay, distinguished by the state of the nuclear spin. The linewidths of these transitions are dependent on the spectral density and the temperature of the environment. If the transition linewidths are narrow in comparison to the transition splitting, then the two decay channels are spectrally resolved (Figure 4.1 d)). Therefore the frequency of the photon emitted as the electron decays provides information about the state of the nuclear spin in the energy eigenbasis. If the nuclear spin is in superposition before the decay, it is projected onto the state associated with the relevant decay channel, and the nuclear coherences are lost.

On the other hand, if the transition linewidths are broad in comparison to the transition splitting, then there is significant overlap between the two spectral lines (Figure 4.1 c)). Now the frequency of an emitted photon does not reveal the state of the nuclear spin. The nuclear spin coherences in the energy eigenbasis can be preserved even as the electron decays. In this way we can engineer a hybrid system with coherence protection.

4.1.1 The Hamiltonian

The hyperfine interaction between spins is approximated by an Ising-type coupling, which is reasonable so long as the Zeeman splitting of the electron spin is large in comparison to the coupling between spins [34]. An Ising-type coupling also has the advantage that the total number of excitations is conserved, allowing us to use the Wigner-Weisskopf method (Section 3.6). The two-spin system Hamiltonian is:

$$H_S = \frac{\omega_0}{2}\sigma_e^z \otimes \mathbb{I}_n + g\sigma_e^z\sigma_n^z, \tag{4.1}$$

where g represents the hyperfine coupling strength and $\sigma_{e(n)}$ is the Pauli operator for the electron (nucleus). Note that the electronic spin will be written first throughout. The computational basis $\{|\uparrow\uparrow\rangle, |\uparrow\downarrow\rangle, |\downarrow\downarrow\rangle, |\downarrow\uparrow\rangle\}$ is also the energy eigenbasis, and the eigenvalues of H_S are $\frac{\omega_0}{2} + g$, $\frac{\omega_0}{2} - g$, $-\frac{\omega_0}{2} + g$ and $-\frac{\omega_0}{2} - g$.

We are interested in what happens to the nuclear coherence when the electron spin has decayed to the ground state, represented by the density matrix element:

$$\rho_{\downarrow\downarrow,\downarrow\uparrow}(t) = \langle\downarrow\downarrow|\rho(t)|\downarrow\uparrow\rangle. \tag{4.2}$$

The interaction between the electron and its bosonic bath is assumed to take the form of the Jaynes-Cummings Hamiltonian (see also Equation 3.56):

$$H_{SB} = \sum_k c_k(\sigma_e^+ b_k + \sigma_e^- b_k^\dagger). \tag{4.3}$$

The free Hamiltonian of the bath is (Equation 3.4):

$$H_B = \sum_k \omega_k b_k^\dagger b_k. \tag{4.4}$$

The interaction picture interaction Hamiltonian is (Equation 3.19):

$$H_I(t) = e^{iH_S t} e^{iH_B t} H_{SB} e^{-iH_S t} e^{-iH_B t}. \tag{4.5}$$

Inserting Equations 4.4 and 4.1 into this produces:

$$H_I(t) = \sum_{n\in\{1,2\}} e^{-i\omega_n t} A_n \otimes b(t) + H.c., \tag{4.6}$$

where $b(t) = \sum_k c_k b_k e^{-i\omega_k t}$ and the transition frequencies are $\omega_{1,2} = \omega_0 \mp 2g$. The transition operators each correspond to an electron spin flip with the nuclear spin in one of two states:

$$A_1 = |{\downarrow\downarrow}\rangle\langle{\uparrow\downarrow}|, \qquad A_2 = |{\downarrow\uparrow}\rangle\langle{\uparrow\uparrow}| \,. \tag{4.7}$$

4.2 An exact solution

Here we follow the method outlined in Section 3.6. Since the temperature is zero and the total Hamiltonian conserves the number of excitations, we may work in the single-excitation subspace. The general single-excitation state for the electron-nuclear spin system at time t can be written:

$$\begin{aligned} |\Psi(t)\rangle =& a_1(t)\, |{\uparrow\downarrow}\rangle \otimes |0\rangle_B + a_2(t)\, |{\uparrow\uparrow}\rangle \otimes |0\rangle_B \\ &+ \sum_k \alpha_{1,k}(t)\, |{\downarrow\downarrow}\rangle \otimes |k\rangle_B + \alpha_{2,k}(t)\, |{\downarrow\uparrow}\rangle \otimes |k\rangle_B, \end{aligned} \tag{4.8}$$

where $a_1(t)$, $a_2(t)$, $\alpha_{1,k}(t)$ and $\alpha_{2,k}(t)$ are complex time-dependent coefficients and $|k\rangle_B$ denotes a single environmental excitation in mode k.

We can use Equations 4.6 and 4.8 to calculate the Schrödinger equation in the

interaction picture:

$$\begin{aligned}\frac{d}{dt}|\Psi(t)\rangle &= -iH_I(t)|\Psi(t)\rangle \\ &= -i\Bigg(\sum_k \Big(e^{i\omega_1 t}\alpha_{1,k}(t)\ |\uparrow\downarrow\rangle + e^{i\omega_2 t}\alpha_{2,k}(t)\ |\uparrow\uparrow\rangle\Big)\otimes c_k e^{-i\omega_k t}|0\rangle \\ &\quad + \Big(e^{-i\omega_1 t}a_1(t)\ |\downarrow\downarrow\rangle + e^{-i\omega_2 t}a_2(t)\ |\downarrow\uparrow\rangle\Big)\otimes\sum_k c_k e^{i\omega_k t}|k\rangle\Bigg). \end{aligned} \tag{4.9}$$

By comparing coefficients in Equations 4.8 and 4.9, we obtain two pairs of coupled differential equations similar in form to Equation 3.65:

$$\begin{aligned}\frac{d}{dt}a_1(t) &= -i\sum_k e^{i(\omega_1-\omega_k)t}\alpha_{1,k}(t)c_k, \qquad \frac{d}{dt}\alpha_{1,k}(t) = -ie^{i(-\omega_1+\omega_k)t}a_1(t)c_k, \\ \frac{d}{dt}a_2(t) &= -i\sum_k e^{i(\omega_2-\omega_k)t}\alpha_{2,k}(t)c_k, \qquad \frac{d}{dt}\alpha_{2,k}(t) = -ie^{i(-\omega_2+\omega_k)t}a_2(t)c_k. \end{aligned} \tag{4.10}$$

These can be written in the general form of Equation 3.65:

$$\frac{d}{dt}a_m(t) = -i\sum_k e^{i(\omega_m-\omega_k)t}\alpha_{m,k}(t)c_k, \quad \frac{d}{dt}\alpha_{m,k}(t) = -ie^{-i(\omega_m-\omega_k)t}a_m(t)c_k, \tag{4.11}$$

where $m \in \{1, 2\}$. The corresponding integro-differential equation is (Equation 3.68):

$$\frac{d}{dt}a_m(t) = -\int_0^t K_m(t-t_1)a_m(t_1)dt_1, \tag{4.12}$$

with kernel (Equation 3.69):

$$K_m(t) = \frac{1}{\pi}\int_{-\infty}^{\infty} d\phi J(\phi)e^{i(\omega_m-\phi)t}. \tag{4.13}$$

Now we must choose a form of the spectral density $J(\phi)$. The spectral density can take many forms, but to be physical it must be equal to zero for negative and zero frequency, and tend to zero at high frequency (Chapter 3). Here we look at the exact solution with

two different spectral densities and discuss their respective merits.

4.2.1 Exact solution – Lorentzian spectral density

The spectral density can be modelled as the Lorentzian:

$$J(\phi) = \frac{1}{2}\frac{\gamma_0\lambda^2}{(\phi_0-\phi)^2+\lambda^2}, \tag{4.14}$$

where ϕ_0 is the centre of the Lorentzian, λ is the half-width and $\gamma_0/2$ is the peak height. Combining Equations 4.13 and 4.14, we obtain:

$$K_m(t) = \frac{\gamma_0\lambda^2}{2\pi}\int_{-\infty}^{\infty} d\phi \frac{e^{i(\omega_m-\phi)t}}{(\phi_0-\phi)^2+\lambda^2}. \tag{4.15}$$

Note here that we haven't imposed the condition that the spectral density must be zero at negative frequencies, so this approach isn't strictly physical.

K_m can be evaluated using complex integration. The integrand has poles at $\phi = \phi_0 \pm i\lambda$, however only the pole at $\phi = \phi_0 + i\lambda$ is enclosed by a semicircle of radius ρ in the upper half plane (contour denoted C).

$$\oint_C d\phi \frac{e^{i(\omega_m-\phi)t}}{(\phi_0-\phi)^2+\lambda^2} = \int_{-\rho}^{\rho} d\phi \frac{e^{i(\omega_m-\phi)t}}{(\phi_0-\phi)^2+\lambda^2} + \int_0^{\pi} d\theta \frac{i\rho e^{i\theta} e^{i(\omega_m-\rho e^{i\theta})t}}{(\phi_0-\rho e^{i\theta})^2+\lambda^2}, \tag{4.16}$$

where $\phi = \rho e^{i\theta}$. As $\rho \to \infty$, the integral over θ becomes:

$$\int_0^{\pi} d\theta \frac{ie^{-i\theta}e^{i(\omega_m-\rho e^{i\theta})t}}{\rho}. \tag{4.17}$$

For this integral to converge, the term $e^{-i\rho e^{i\theta}t}$ must tend to zero (and not to infinity). This imposes the condition:

$$\mathbb{R}[-i\rho e^{i\theta}t] \leq 0 \Rightarrow \rho t \sin(\theta) \leq 0. \tag{4.18}$$

To fulfil this it is necessary to impose $t \leq 0$, i.e. $t = -|t|$. With this condition imposed, the radial integral tends to zero and we can use the Residue Theorem to evaluate the contour integral in Equation 4.16:

$$\begin{aligned}\oint_C d\phi \frac{e^{i(\phi-\omega_m)|t|}}{(\phi_0-\phi)^2+\lambda^2} &= 2\pi i \times \mathrm{Res}(\phi = \phi_0 + i\lambda), \\ &= 2\pi i \lim_{\phi\to\phi_0+i\lambda}\left(\frac{(\phi-\phi_0-i\lambda)e^{i(\phi-\omega_m)|t|}}{(\phi-\phi_0-i\lambda)(\phi-\phi_0+i\lambda)}\right), \\ &= \frac{\pi}{\lambda}e^{i(\phi_0-\omega_m)|t|}e^{-\lambda|t|}. \end{aligned} \tag{4.19}$$

The solution for $t > 0$ can be obtained by completing the contour integral in the lower half plane. The result in Equation 4.19 is valid for all t. The following expression for the kernel is therefore also valid for all t:

$$K_m(t) = \frac{\gamma_0\lambda}{2}e^{i(\phi_0-\omega_m)|t|}e^{-\lambda|t|} \qquad m \in \{1,2\}. \tag{4.20}$$

Inserting Equation 4.20 into Equation 4.12, we obtain:

$$\frac{d}{dt}a_m(t) = -\int_0^t \frac{\gamma_0\lambda}{2}e^{i(\phi_0-\omega_m)(t-t_1)}e^{-\lambda(t-t_1)}a_m(t_1)dt_1. \tag{4.21}$$

Using the Fundamental Theorem of Calculus, Equation 4.21 can be rewritten as a homogeneous linear second order differential equation:

$$a_m''(t) + (i(\omega-\phi_0)+\lambda)a_m'(t) + \frac{\gamma_0\lambda}{2}a_m(t) = 0. \tag{4.22}$$

This can easily be solved by using the ansatz $a_m(t) = e^{k_m t}$:

$$\begin{aligned} k_m^2 + (i(\omega_m-\phi_0)+\lambda)k_m + \frac{\gamma_0\lambda}{2} &= 0, \\ \Rightarrow k_m &= \frac{i(\phi_0-\omega_m)-\lambda\pm\Lambda_m}{2}, \end{aligned} \tag{4.23}$$

where we have defined $\Lambda_m = \sqrt{(i(\omega_m - \phi_0) + \lambda)^2 - 2\gamma_0\lambda}$. The total solution is (using the superposition principle):

$$a_m(t) = C_1 \exp\left(\frac{(i(\phi_0 - \omega_m) - \lambda + \Lambda_m)t}{2}\right) + C_2 \exp\left(\frac{(i(\phi_0 - \omega_m) - \lambda - \Lambda_m)t}{2}\right). \tag{4.24}$$

To find the coefficients C_1 and C_2 we impose the initial conditions:

$$C_1 + C_2 = a_m(0), \qquad \frac{d}{dt}a_m(t)\bigg|_{t=0} = 0. \tag{4.25}$$

The right-hand initial condition is obtained by observing that the environment is initially in a vacuum state, so $\alpha_{m,k}(0) = 0$, which is then inserted into Equation 4.11.

Imposing these, we find:

$$C_1 = a_m(0)\left(\frac{i(\omega_m - \phi_0) + \lambda + \Lambda_m}{2\Lambda_m}\right), \quad C_2 = a_m(0)\left(\frac{i(\phi_0 - \omega_m) - \lambda + \Lambda_m}{2\Lambda_m}\right). \tag{4.26}$$

Combining Equations 4.24 and 4.26:

$$a_m(t) = a_m(0)e^{i(\phi_0-\omega_m)t/2}e^{-\lambda t/2}\left(\cosh\left(\Lambda_m t/2\right) + \left(\frac{i(\omega_m - \phi_0) + \lambda}{\Lambda_m}\right)\sinh\left(\Lambda_m t/2\right)\right). \tag{4.27}$$

Note that $a_1(t)$ and $a_2(t)$ are the coefficients of the state in the interaction picture, as defined in Equation 4.8.

To calculate the ground state coherences, we must find:

$$\begin{aligned}\rho_{\downarrow\downarrow,\downarrow\uparrow}(t) &= \mathrm{Tr}_B[\langle\downarrow\downarrow|\psi\rangle\langle\psi|\downarrow\uparrow\rangle], \\ &= \mathrm{Tr}_B\left[\sum_{kk'}\alpha_{1,k}(t)\alpha^*_{2,k'}(t)|k\rangle_B\langle k'|_B\right], \\ &= \sum_k \alpha_{1,k}(t)\alpha^*_{2,k}(t).\end{aligned} \tag{4.28}$$

From Equation 4.10 we find:

$$\alpha_{1,k}(t) = -i\int_0^t c_k a_1(t_1)e^{i(-\omega_1+\omega_k)t_1}dt_1, \quad \alpha^*_{2,k}(t) = i\int_0^t c_k^* a_2^*(t_1)e^{i(\omega_2-\omega_k)t_1}dt_1. \tag{4.29}$$

Inserting these into Equation 4.28:

$$\begin{aligned}\rho_{\downarrow\downarrow,\downarrow\uparrow}(t) &= \sum_k |c_k|^2 \int_0^t dt_1 \int_0^t dt_2 e^{i(2g(t_1+t_2)+(\omega_0-\omega_k)(t_2-t_1))}a_1(t_1)a_2^*(t_2), \\ &= \frac{1}{\pi}\int_0^t dt_1 \int_0^t dt_2 e^{2ig(t_1+t_2)}a_1(t_1)a_2^*(t_2)\int_{-\infty}^{\infty} d\phi J(\phi)e^{i(\omega_0-\phi)(t_2-t_1)}.\end{aligned} \tag{4.30}$$

By comparing the ϕ integral to Equation 4.13, and using the form of the kernel given in Equation 4.20, we obtain the lower nuclear coherence in the interaction picture:

$$\rho_{\downarrow\downarrow,\downarrow\uparrow}(t) = \frac{\gamma_0\lambda}{2}\int_0^t dt_1 \int_0^t dt_2 a_1(t_1)a_2^*(t_2)e^{2ig(t_1+t_2)}e^{i(\phi_0-\omega_0)|t_2-t_1|}e^{-\lambda|t_2-t_1|}. \tag{4.31}$$

The lower-state dynamics are computationally intensive to plot due to the double integral in Equation 4.31, however the upper-state dynamics are readily accessible. Figures 4.2 and 4.4 show the dynamics of the upper electron state populations, $|a_1(t)|^2+|a_2(t)|^2$, where $a_m(t)$ is given by Equation 4.27. The environment has a Lorentzian spectral density $J(\omega)$ with a negative-frequency tail (see Figure 4.3).

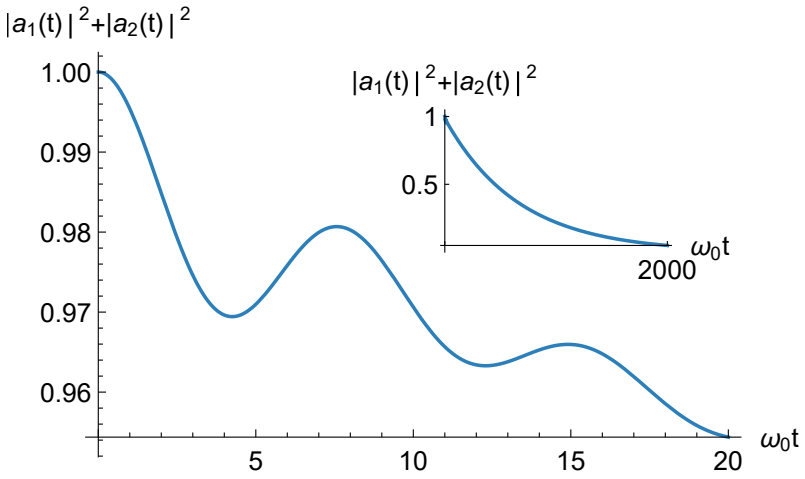

Figure 4.2: The dynamics of the excited electron state populations $|a_1(t)|^2 + |a_2(t)|^2$ following preparation in $|\uparrow\rangle(|\uparrow\rangle + |\downarrow\rangle)/\sqrt{2}$ with hyperfine coupling of $0.01\omega_0$. The electron is coupled to an Lorentzian bath peaked at $0.2\omega_0$ with half-width $\lambda = 0.1\omega_0$ and peak rate $\gamma_0 = 0.1\omega_0$ (see Figure 4.3). The short-time dynamics show population revivals which are not captured in the Born-Markov equations. Over long times (inset) the excited state populations decay.

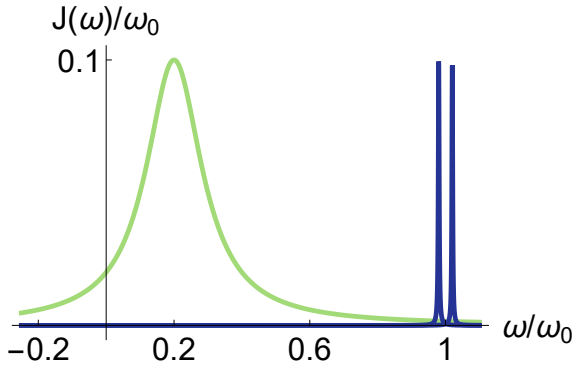

Figure 4.3: The spectral density (green) and the transition spectra (dark blue) for the parameters used in Figure 4.2. The bath has significant structure far away from the transition frequencies. In addition, the spectral density has an unphysical negative-frequency tail.

In Figure 4.2 we see that the excited electron states undergo short-time population revivals. This behaviour cannot be captured by the Born-Markov master equation, which predicts simple exponential decay of excited state populations at zero temperature. There are two possible reasons for these revivals, both of which are concerned with the structure

of the bath (depicted in Figure 4.3):

1. The negative-frequency tail of the spectral density, which is unphysical, is causing population revivals by allowing negative-frequency transitions.

2. The bath has significant structure far away from the transition frequencies, making it highly non-Markovian, and the population revivals are symptoms of this non-Markovianity.

To test which of these hypotheses is causing the revivals, we can increase the half-width of the spectral density. This will increase the negative-frequency tail, so if Hypothesis 1 is correct, then the revivals should increase in amplitude. However, the bath will also become more Markovian, so if Hypothesis 2 is correct then the revivals should decrease in amplitude and eventually become washed out altogether.

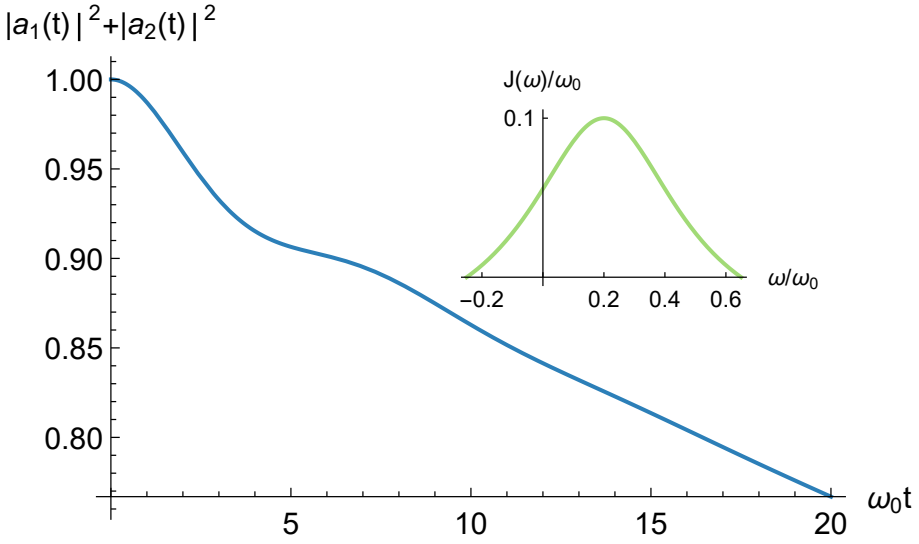

Figure 4.4: The short-time dynamics of the excited state populations, using a Lorentzian bath with half-width $\lambda = 0.3$ (shown in inset) and all other parameters as in Figure 4.2. Broadening the bath's spectral density increases its negative frequency tail, but also makes it more Markovian. The short-time dynamics no longer show the population revivals seen in Figure 4.2, indicating that they were a result of the non-Markovianity of the bath.

The short-time dynamics for a broader spectral density are plotted in Figure 4.4, and we see that the revivals are washed out entirely, confirming the second hypothesis. However, since it is still unphysical to use a spectral density with a negative-frequency tail, in the next Section we look at the exact solution with a physical spectral density.

4.2.2 Exact solution – physical spectral density

If we impose the condition $J(\omega \leq 0) = 0$, then the integral form of the kernel (Equation 4.13) becomes a one-sided integral and cannot be solved using contour integration, so instead we turn to the Laplace transform method outlined in Section 3.6.1.

In the two-spin case, Equation 3.78 becomes:

$$\tilde{\alpha}_{m,k}(s) = -\frac{ic_k}{s}\frac{a_m(0)}{s + i(\omega_m - \omega_k) + f(s - i\omega_k)} \qquad m \in \{1, 2\}. \tag{4.32}$$

The Laplace transform of Equation 4.28 is:

$$\tilde{\rho}_{\downarrow\downarrow,\downarrow\uparrow}(s_1, s_2) = \sum_k \tilde{\alpha}_{1,k}(s_1)\tilde{\alpha}^*_{2,k}(s_2). \tag{4.33}$$

Combining Equations 4.33 and 4.32 produces an expression for the Laplace transformed nuclear coherence:

$$\tilde{\rho}_{\downarrow\downarrow,\downarrow\uparrow}(s_1, s_2) = a_1(0)a_2^*(0)\frac{1}{\pi}\int_0^\infty d\phi J(\phi)\frac{1}{s_1\big(s_1 + i(\omega_1 - \phi) + f(s_1 - i\phi)\big)} \times \frac{1}{s_2\big(s_2 - i(\omega_2 - \phi) + f^*(s_2 - i\phi)\big)}. \tag{4.34}$$

Take the inverse Laplace transform of Equation 4.34:

$$\rho_{\downarrow\downarrow,\downarrow\uparrow}(t) = -\frac{1}{4\pi^3}\int_{\mathcal{B}} ds_1 \int_{\mathcal{B}} ds_2 e^{(s_1+s_2)t} a_1(0)a_2^*(0) \times \int_0^\infty d\phi J(\phi) \frac{1}{s_1\big(s_1 + i(\omega_1 - \phi) + f(s_1 - i\phi)\big)} \frac{1}{s_2\big(s_2 - i(\omega_2 - \phi) + f^*(s_2 - i\phi)\big)}. \tag{4.35}$$

Here $\mathcal{B}$ denotes the Bromwich contour, a vertical contour in the complex plane chosen such that all singularities lie to the left of it [123]. The s-integrals in Equation 4.35 each have a pole at $s = 0$, plus families of poles at $s_1 = -i(\omega_1 - \phi) - f(s_1 - i\phi)$ and $s_2 = i(\omega_2 - \phi) - f^*(s_2 - i\phi)$. This makes Equation 4.35 is very difficult to solve in general, since $f(s)$ is a one-sided complex integral with poles. However, things are simplified when looking at the steady state. Here we are concerned only with contributions from the s integrals that survive for infinite times, i.e. those with a zero real part. All other contributions will decay away within a finite timespan. This means we only need to calculate the residue for the $s = 0$ poles. The residue at $s_1 = 0$ is:

$$\text{Res}(s_1 = 0) = 2\pi i \frac{1}{i(\omega_1 - \phi) + f(-i\phi + 0)}. \tag{4.36}$$

Using the definition of $f(s)$ (Equation 3.77):

$$\begin{aligned} f(-i\phi + 0) &= \frac{1}{\pi}\int_0^\infty d\nu \frac{J(\nu)}{i(\nu - \phi) + 0}, \\ &= \frac{-i}{\pi}\left(i\pi J(\phi) + \mathcal{P}\int_0^\infty d\nu \frac{J(\nu)}{\nu - \phi}\right), \\ &= J(\phi) + \frac{i}{\pi}\mathcal{P}\int_0^\infty d\nu \frac{J(\nu)}{\phi - \nu}, \\ &= \Gamma_\downarrow(\phi), \end{aligned} \tag{4.37}$$

where $\Gamma_\downarrow(\phi)$ is defined as the positive-frequency Born-Markov rate at zero temperature

(Equation 3.46). The steady state coherence becomes:

$$\lim_{t\to\infty}\rho_{\downarrow\downarrow,\downarrow\uparrow}(t) = a_1(0)a_2^*(0)\frac{1}{\pi}\int_0^\infty d\phi \frac{J(\phi)}{(\omega_1-\phi-i\Gamma_\downarrow(\phi))(\omega_2-\phi+i\Gamma_\downarrow^*(\phi))}. \tag{4.38}$$

Ohmic spectral density

Equation 4.38 can be solved numerically for an Ohmic spectral density with cutoff (Equation 3.13) such as:

$$J(\omega) = \gamma_0\frac{\omega}{\omega_c}e^{1-\omega/\omega_c} \qquad \omega \geq 0, \tag{4.39}$$

where γ_0 is the typical electronic decay rate and ω_c is the cutoff frequency (such that the bath is approximately flat around $\omega \simeq \omega_c$). However the dynamics are no longer accessible and we can only look at the steady state solution.

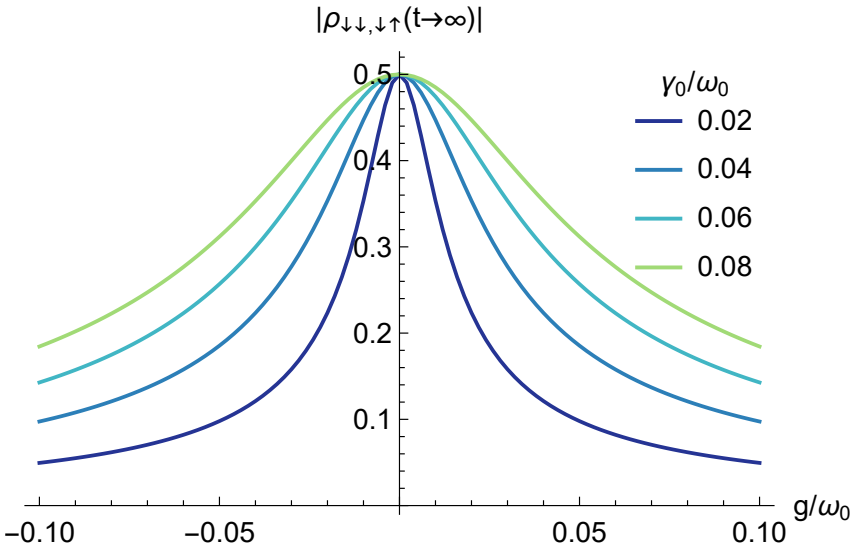

Figure 4.5: The magnitude of the steady state nuclear coherence once the electron has decayed, $|\rho_{\downarrow\downarrow,\downarrow\uparrow}|$ at zero temperature as a function of the hyperfine coupling g. The electron is coupled to an Ohmic environment with peak rate γ_0, peaked at the electronic Zeeman splitting frequency ω_0.

Figure 4.5 plots the steady state nuclear coherence following preparation in the initial

superposition state $|\psi(0)\rangle = |\uparrow\rangle(|\uparrow\rangle + |\downarrow\rangle)/\sqrt{2}$. All of the steady state nuclear coherence is in the lower electron spin state, so Figure 4.5 plots the entire steady state nuclear coherence. When the hyperfine coupling is small compared to γ_0, the steady state nuclear coherence is close to its initial value of $1/2$. Coherence is transferred from $\rho_{\uparrow\downarrow,\uparrow\uparrow}$ to $\rho_{\downarrow\downarrow,\downarrow\uparrow}$ as the electron decays, but it is not lost.

Increasing the hyperfine coupling increases the separability of the two transitions (see Figure 4.1), so that the frequency of the photon emitted provides information about which of the transitions has occurred. The environment effectively measures the frequency of the emitted photon, destroying nuclear coherence even if no measurements are made as part of the experiment. Therefore increasing $|g|$ causes a loss of steady-state nuclear coherence as seen in Figure 4.5.

Increasing γ_0 increases the rate of the two transitions, increasing the linewidth of the transition spectra and therefore increasing the overlap between them. This makes the two transitions less separable for a given value of g, allowing more nuclear coherences to persist into the steady state. This may seem counter-intuitive, as an increase in the typical electronic decay rate might be thought to cause faster decay of the nuclear spin. However when the electron decays quickly, there is less time for the nuclear spin state to be indirectly sampled by the environment during electronic decay. Less information about the nuclear spin leaks out and coherences can be better preserved.

Now we will compare our exact solution to one obtained using a Born-Markov master equation, so we can assess the suitability of the Born-Markov approach.

4.3 Born-Markov solution

To generate the Born-Markov master equation, we use the transition operators A_n from Equation 4.7 and corresponding frequencies $\omega_1 = \omega_0 - 2g$, $\omega_2 = \omega_0 + 2g$. We insert these into the Markovian quantum master equation from Chapter 3 (Equation 3.33). At

zero temperature, the absorption rate $\Gamma_{\uparrow}(\omega) = 0$. The non-secular interaction picture quantum master equation then simplifies to:

$$\frac{d}{dt}\rho(t) = \sum_{n,m=1,2} e^{i(\omega_m-\omega_n)t}\Big(\Gamma_{\downarrow}(\omega_n)\Big(A_n^{\dagger}\rho(t)A_m - A_m A_n^{\dagger}\rho(t)\Big) + \Gamma_{\downarrow}^{*}(\omega_m)\Big(A_n^{\dagger}\rho(t)A_m - \rho(t)A_m A_n^{\dagger}\Big)\Big). \tag{4.40}$$

The zero-temperature emission rate $\Gamma_{\downarrow}(\omega)$ is:

$$\Gamma_{\downarrow}(\omega) = J(\omega) + \frac{i}{\pi}\mathcal{P}\int_0^{\infty}\frac{J(\phi)}{\omega-\phi}d\phi. \tag{4.41}$$

Equation 4.40 results in sixteen coupled first-order differential equations, one for each element of the density matrix:

$$\begin{aligned}
\dot{\rho}_{\uparrow\uparrow,\uparrow\uparrow}(t) &= -\dot{\rho}_{\downarrow\uparrow,\downarrow\uparrow}(t) = -2\,\mathbb{R}[\Gamma_{\downarrow}(\omega_2)]\rho_{\uparrow\uparrow,\uparrow\uparrow}(t),\\
\dot{\rho}_{\uparrow\downarrow,\uparrow\downarrow}(t) &= -\dot{\rho}_{\downarrow\downarrow,\downarrow\downarrow}(t) = -2\,\mathbb{R}[\Gamma_{\downarrow}(\omega_1)]\rho_{\uparrow\downarrow,\uparrow\downarrow}(t),\\
\dot{\rho}_{\uparrow\downarrow,\uparrow\uparrow}(t) &= -\big(\Gamma_{\downarrow}(\omega_1) + \Gamma_{\downarrow}^{*}(\omega_2)\big)\rho_{\uparrow\downarrow,\uparrow\uparrow}(t),\\
\dot{\rho}_{\downarrow\downarrow,\downarrow\uparrow}(t) &= e^{4igt}\big(\Gamma_{\downarrow}(\omega_1) + \Gamma_{\downarrow}^{*}(\omega_2)\big)\rho_{\uparrow\downarrow,\uparrow\uparrow}(t),\\
\dot{\rho}_{\uparrow\uparrow,\downarrow\sigma}(t) &= -\Gamma_{\downarrow}(\omega_2)\rho_{\uparrow\uparrow,\downarrow\sigma}(t),\\
\dot{\rho}_{\uparrow\downarrow,\downarrow\sigma}(t) &= -\Gamma_{\downarrow}(\omega_1)\rho_{\uparrow\downarrow,\downarrow\sigma}(t),
\end{aligned} \tag{4.42}$$

where $\sigma \in \{\uparrow, \downarrow\}$. The interaction picture solutions are:

$$
\begin{aligned}
\rho_{\uparrow\uparrow,\uparrow\uparrow}(t) =& \exp[-2\,\mathbb{R}[\Gamma_\downarrow(\omega_2)]t]\rho_{\uparrow\uparrow,\uparrow\uparrow}(0),\\
\rho_{\downarrow\uparrow,\downarrow\uparrow}(t) =& \Big(1-\exp[-2\,\mathbb{R}[\Gamma_\downarrow(\omega_2)]t]\Big)\rho_{\uparrow\uparrow,\uparrow\uparrow}(0)+\rho_{\downarrow\uparrow,\downarrow\uparrow}(0),\\
\rho_{\uparrow\downarrow,\uparrow\downarrow}(t) =& \exp[-2\,\mathbb{R}[\Gamma_\downarrow(\omega_1)]t]\rho_{\uparrow\downarrow,\uparrow\downarrow}(0),\\
\rho_{\downarrow\downarrow,\downarrow\downarrow}(t) =& \Big(1-\exp[-2\,\mathbb{R}[\Gamma_\downarrow(\omega_1)]t]\Big)\rho_{\uparrow\downarrow,\uparrow\downarrow}(0)+\rho_{\downarrow\downarrow,\downarrow\downarrow}(0),\\
\rho_{\uparrow\downarrow,\uparrow\uparrow}(t) =& \exp[-\big(\Gamma_\downarrow(\omega_1)+\Gamma^*_\downarrow(\omega_2)\big)t]\rho_{\uparrow\downarrow,\uparrow\uparrow}(0),\\
\rho_{\downarrow\downarrow,\downarrow\uparrow}(t) =& \frac{\Gamma_\downarrow(\omega_1)+\Gamma^*_\downarrow(\omega_2)}{4ig-\big(\Gamma_\downarrow(\omega_1)+\Gamma^*_\downarrow(\omega_2)\big)}\Big(\exp[\big(4ig-\big(\Gamma_\downarrow(\omega_1)+\Gamma^*_\downarrow(\omega_2)\big)\big)t]-1\Big)\rho_{\uparrow\downarrow,\uparrow\uparrow}(0)\\
&+\rho_{\downarrow\downarrow,\downarrow\uparrow}(0),\\
\rho_{\uparrow\uparrow,\downarrow\sigma}(t) =& \exp[-\Gamma_\downarrow(\omega_2)t]\rho_{\uparrow\uparrow,\downarrow\sigma}(0),\\
\rho_{\uparrow\downarrow,\downarrow\sigma}(t) =& \exp[-\Gamma_\downarrow(\omega_1)t]\rho_{\uparrow\downarrow,\downarrow\sigma}(0).
\end{aligned}
\tag{4.43}
$$

The real parts of the rates $\Gamma_\downarrow(\omega_{1,2})$ are proportional to the decay constants for the populations of the excited states $|\uparrow\downarrow\rangle$ and $|\uparrow\uparrow\rangle$ respectively and are equal to the spectral density sampled at the appropriate transition frequency. The excited state populations irreversibly decay into the electronic ground states, as there is no absorption from the environment. The nuclear coherence in the excited electron state also decays, but the lower nuclear coherence $\rho_{\downarrow\downarrow,\downarrow\uparrow}(t)$ can be maintained.

4.3.1 Born-Markov dynamics

One benefit of the Born-Markov approach over the exact method outlined in Section 4.2 is that it allows us to look at the dynamics of components of the system density matrix, provided that the bath correlations cannot be resolved over the timescales chosen. Figure 4.6 plots the nuclear coherence dynamics with the electron in the ground state. The system is initialised in a nuclear superposition with the electron spin up, so

the lower nuclear coherence builds from zero, reaching a steady-state value dependent on g. As we saw in Figure 4.5, smaller spin-spin coupling allows for greater steady-state nuclear coherence to be preserved.

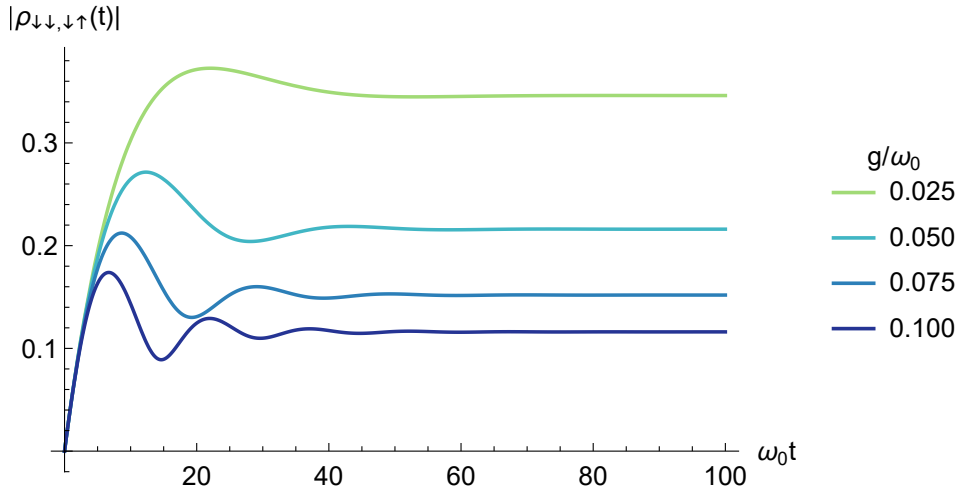

Figure 4.6: The zero temperature interaction picture dynamics of the lower nuclear coherence magnitude, $|\rho_{\downarrow\downarrow,\downarrow\uparrow}(t)|$ at several electron-nucleus coupling strengths g following preparation in the superposition state $|\psi(0)\rangle = |\uparrow\rangle(|\uparrow\rangle + |\downarrow\rangle)/\sqrt{2}$. The electron is coupled to an Ohmic bath peaked at the bare electron splitting ω_0 and peak rate $\gamma_0 = 0.05\omega_0$.

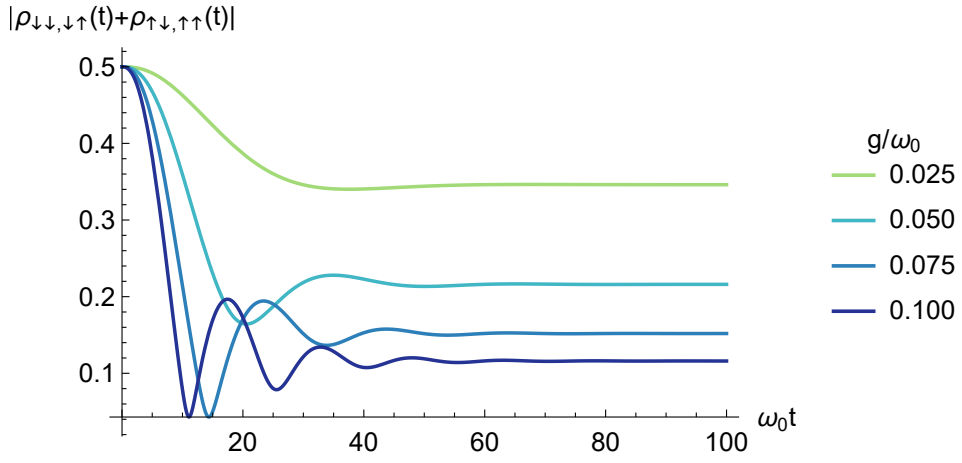

Figure 4.7: The zero temperature dynamics of the magnitude of total nuclear coherence, $|\rho_{\downarrow\downarrow,\downarrow\uparrow}(t) + \rho_{\uparrow\downarrow,\uparrow\uparrow}(t)|$, using the same parameters as in Figure 4.6.

We can see that the nuclear coherence that builds in the lower electron state is transferred from the initial coherence in the upper electron state if we look at the dynamics of the total nuclear coherence (Figure 4.7). Here we see clearly that the initial coherence of $1/2$ is well protected as the electron decays for small values of the hyperfine coupling.

There are also some interesting features in the dynamics of Figures 4.6 and 4.7. The shape of the coherence plots are determined by an overall decay envelope, modulated by oscillations that become more pronounced with larger spin-spin coupling. To understand why, it is useful to consider the precession of the nuclear spin under the influence of the effective magnetic field caused by the interaction with the electron spin. This can be illustrated by by plotting the dynamics of the nuclear spin x-component (Figure 4.8).

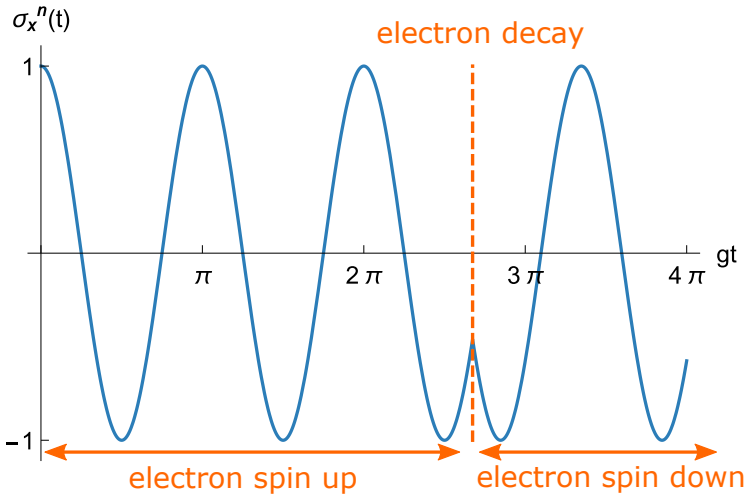

Figure 4.8: The precession of the nuclear spin due to the electron's magnetic field, both before and after electron decay. When the electron flips, the magnetic field felt by the nuclear spin changes sign, reversing its precession direction. Here the hyperfine coupling is larger than the typical electron decay rate, so several complete nuclear oscillations occur before the electronic decay.

Initially, the electron is spin up, and the nuclear spin precesses around this with frequency $2g$. However, when the electron decays, the effective magnetic field felt by the nuclear spin swaps direction, and the nuclear spin starts precessing in the opposite

direction (Figure 4.8).

The illustration depicted in Figure 4.8 is just one iteration of the dynamics; the density matrix dynamics represent an average over many iterations. The electron lifetime will be different in each iteration, with a mean decay rate of around γ_0. If the rate of nuclear spin precession (given by the spin-spin coupling) is large in comparison with the mean decay rate, then typically several oscillations in σ_n^x will be completed before the electron flips. This is the case illustrated in Figure 4.8. When these different iterations are averaged, there is interference between them, which causes oscillations in the dynamics. The interference also causes phase averaging, meaning that less nuclear coherence is preserved.

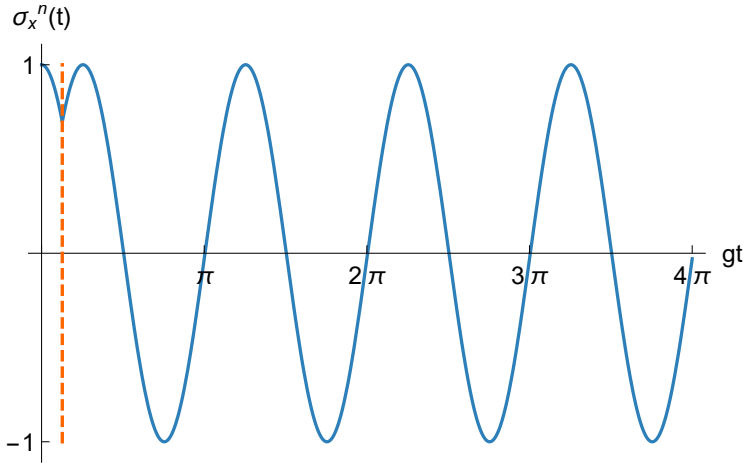

Figure 4.9: The precession of the nuclear spin due to the electron's magnetic field during electronic decay. Here the electron flips quickly, so less nuclear phase information is lost.

However, if the spin-spin coupling is small in comparison to the electronic decay rate, then the decay happens within the first portion of the first nuclear oscillation (Figure 4.9). The different iterations of the nuclear spin dynamics are all very similar and do not interfere as destructively, allowing nuclear coherence to be preserved. Another way to look at this is that the environment has had less time to sample the nuclear phase information before the electron decays.

4.3.2 Validity of approximations

To derive Equation 4.40, we assumed the spin-spin coupling is of Ising form, and we used the Born-Markov approximation. In addition, it is common to use secularisation (Section 3.4.5) to further simplify the master equation. Here we investigate the validity of these three approximations in the order:

1. Born-Markov approximation,
2. Ising coupling between spins,
3. Secularisation.

The Born-Markov approximation

In the long time limit, the lower nuclear coherence from Equation 4.43 becomes:

$$\lim_{t\to\infty} |\rho_{\downarrow\downarrow,\downarrow\uparrow}(t)| \leq \left| \frac{\big(\Gamma_{\downarrow}(\omega_1) + \Gamma^{*}_{\downarrow}(\omega_2)\big)\rho_{\uparrow\downarrow,\uparrow\uparrow}(0)}{4ig - \big(\Gamma_{\downarrow}(\omega_1) + \Gamma^{*}_{\downarrow}(\omega_2)\big)} \right| + |\rho_{\downarrow\downarrow,\downarrow\uparrow}(0)| \,. \tag{4.44}$$

Figure 4.10 numerically compares Equation 4.44 to the exact solution from Equation 4.38, using an Ohmic spectral density of the form of Equation 4.39.

For the parameters chosen in Figure 4.10, the Born-Markov approximation is an extremely good one – the bath is approximately flat across the transition linewidths. The Born-Markov master equation assumes that the bath is sampled at each of the transition frequencies – this is a good approximation as long as the variation in the spectral density function across the linewidth of the transition is small in comparison to the spectral density at the transition frequency.

Figure 4.11 shows sample emission spectra for two different values of the system-bath coupling strength γ_0. The spin-spin coupling strength here is equal to the maximum value used in Figure 4.10 in order to accentuate the effect of varying γ_0.

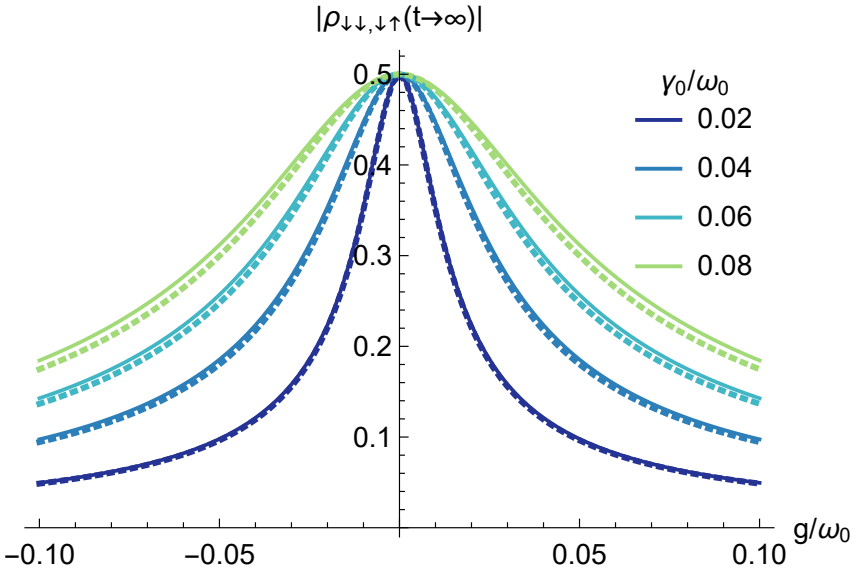

Figure 4.10: The zero temperature steady state lower nuclear coherence magnitude, $|\rho_{\downarrow\downarrow,\downarrow\uparrow}|$ as a function of the electron-nucleus coupling g. The bath has an Ohmic spectral density peaked at the bare electron splitting ω_0 and peak rate γ_0. Solid lines represent the exact solutions; dashed lines the Born-Markov solutions.

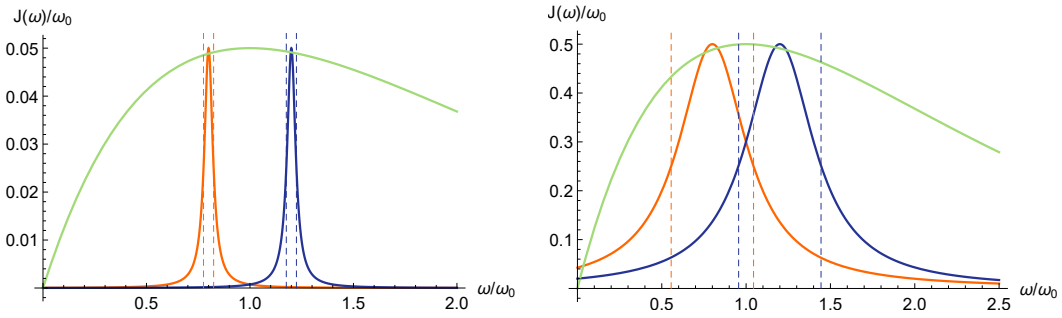

Figure 4.11: Dependence of linewidth and spectral density on system-bath coupling strength γ_0. Left: $\gamma_0 = 0.05\omega_0$; right: $\gamma_0 = 0.5\omega_0$. Each plot contains sample zero temperature emission spectra for two transitions centred at $\omega = \omega_0 \pm 2g$ (orange and dark blue solid lines). The hyperfine coupling $g = 0.1\omega_0$. The spectral linewidths are equal to the spectral density sampled at the transition frequencies. Also plotted is the Ohmic spectral density (green). When the system-bath coupling is small enough (left), the variation in spectral density across the transition linewidths is small and the Born-Markov approximation holds. Increasing γ_0 results in significant variation in the spectral density across the transition linewidths (right); here, the Born-Markov approximation fails.

Increasing γ_0 increases both the peak height of the spectral density and the linewidths of the transition spectra. As γ_0 gets too large, the variation of the spectral density across the linewidth becomes significant and the Born-Markov master equation no longer accurately predicts the system behaviour. In the Born-Markov equation, the spectral density is sampled at the central frequency for each transition on the assumption that the variation in spectral density across the linewidth is minimal. When this is no longer true, the Born-Markov approximation can no longer be applied. The Born-Markov approximation uses perturbation theory of second order in system-bath interaction strength [124]; so we would expect it to fail at high γ_0.

Ising hyperfine coupling

In deriving Equation 4.40, we used a system Hamiltonian with Ising coupling between spins (Equation 4.1). Here we investigate the effect of adding XY spin-spin coupling of strength g_1 to the Hamiltonian:

$$H_S^{XY} = \frac{\omega_0}{2}\sigma_e^z \otimes \mathbb{I}_n + g_1(\sigma_e^x\sigma_n^x + \sigma_e^y\sigma_n^y) + g_2\sigma_e^z\sigma_n^z. \tag{4.45}$$

Unlike the Ising Hamiltonian, the eigenstates of Equation 4.45 are not simply the computational basis states – there is mixing between the two states with one excited spin:

Eigenenergy	Eigenstate
$\frac{\omega_0}{2} + g_2,$	$\lvert\Uparrow\rangle = \lvert\uparrow\uparrow\rangle,$
$\frac{\Omega_0}{2} - g_2,$	$\lvert+\rangle = \cos\theta\,\lvert\uparrow\downarrow\rangle - \sin\theta\,\lvert\downarrow\uparrow\rangle,$
$g_2 - \frac{\omega_0}{2},$	$\lvert\Downarrow\rangle = \lvert\downarrow\downarrow\rangle,$
$-\frac{\Omega_0}{2} - g_2,$	$\lvert-\rangle = \sin\theta\,\lvert\uparrow\downarrow\rangle + \cos\theta\,\lvert\downarrow\uparrow\rangle,$

(4.46)

where the mixing angle satisfies:

$$\cos\theta = \sqrt{\frac{1}{2}\Big(1+\frac{\omega_0}{\Omega}\Big)}, \qquad \sin\theta = \sqrt{\frac{1}{2}\Big(1-\frac{\omega_0}{\Omega}\Big)}, \tag{4.47}$$

with $\Omega = \sqrt{16g_1^2+\omega_0^2}$.

As before, we find the interaction picture interaction Hamiltonian (Equation 3.57), and so identify the following transition frequencies and operators, expressed in the basis of system eigenstates defined in Equation 4.46:

Transition frequency	Transition operator
$\omega_1 = -\frac{\omega_0}{2} - 2g_2 + \frac{\Omega}{2},$	$-\sin\theta\ \lvert\Uparrow\rangle\langle+\rvert,$
$\omega_2 = -\frac{\omega_0}{2} - 2g_2 - \frac{\Omega}{2},$	$\cos\theta\ \lvert\Uparrow\rangle\langle-\rvert,$
$\omega_3 = -\frac{\omega_0}{2} + 2g_2 - \frac{\Omega}{2},$	$\cos\theta\lvert+\rangle\langle\Downarrow\rvert,$
$\omega_4 = -\frac{\omega_0}{2} + 2g_2 + \frac{\Omega}{2},$	$\sin\theta\lvert-\rangle\langle\Downarrow\rvert\ .$

(4.48)

The transition frequencies and operators in Equation 4.48 are then inserted into the Born-Markov master equation in the Schrödinger picture, found by transforming Equation 4.40 from the interaction picture (see Section 3.4.3):

$$\begin{aligned}\frac{d}{dt}\rho(t) = &-i[H_S,\rho(t)] + \sum_{i,j=1}^{4}\Big(\Gamma_\uparrow(\omega_i)\Big(A_i\rho(t)A_j^\dagger - A_j^\dagger A_i\rho(t)\Big)\\ &+\Gamma_\uparrow^*(\omega_j)\Big(A_i\rho(t)A_j^\dagger - \rho(t)A_j^\dagger A_i\Big) + \Gamma_\downarrow(\omega_j)\Big(A_j^\dagger\rho(t)A_i - A_iA_j^\dagger\rho(t)\Big)\\ &+\Gamma_\downarrow^*(\omega_i)\Big(A_j^\dagger\rho(t)A_i - \rho(t)A_iA_j^\dagger\Big)\Big).\end{aligned} \tag{4.49}$$

Our question is whether the addition of XY coupling affects the long-time behaviour of the system. To investigate this, it is useful to look at the Liouvillian at zero temperature (Section 3.4.6). In the absence of XY coupling, there are four Liouvillian eigenvalues

with zero real parts. They and their corresponding eigenvectors (written as density matrix components in the eigenbasis) are:

Eigenvalue	Eigenvector
$\lambda_1 = 0,$	$\boldsymbol{v}_1 = \rho_{-,-},$
$\lambda_2 = 0,$	$\boldsymbol{v}_2 = \rho_{\Downarrow,\Downarrow},$
$\lambda_3 = -2ig_2,$	$\boldsymbol{v}_3 = \rho_{\Downarrow,-},$
$\lambda_4 = 2ig_2,$	$\boldsymbol{v}_4 = \rho_{-,\Downarrow}.$

(4.50)

Recall from the discussion in Section 3.4.6 that multiple zero eigenvalues indicate the presence of multiple steady states due to a symmetry in the system. In the absence of XY coupling, both of the spin states $|\downarrow\downarrow\rangle$ and $|\downarrow\uparrow\rangle$ are stable, and so the populations of these states and the coherences between them form the Liouvillian zero eigenvectors given above.

The other twelve Liouvillian eigenvalues of the Ising master equation all have negative real parts, meaning that their corresponding states decay to zero in the long time limit:

$$\begin{aligned}
\lambda_5 &= i\omega_0 - \Gamma_\uparrow^*(-\omega_2), & \lambda_6 &= \lambda_5^*, \\
\lambda_7 &= i\omega_0 - \Gamma_\uparrow^*(-\omega_3), & \lambda_8 &= \lambda_7^*, \\
\lambda_9 &= i\omega_0 + 2ig_2 - \Gamma_\uparrow^*(-\omega_2), & \lambda_{10} &= \lambda_9^*, \\
\lambda_{11} &= i\omega_0 - 2ig_2 - \Gamma_\uparrow^*(-\omega_3), & \lambda_{12} &= \lambda_{11}^*, \\
\lambda_{13} &= 2ig_2 - \Gamma_\uparrow^*(-\omega_2) - \Gamma_\uparrow(-\omega_3), & \lambda_{14} &= \lambda_{13}^*, \\
\lambda_{15} &= -\Gamma_\uparrow^*(-\omega_2) - \Gamma_\uparrow(-\omega_2), & \lambda_{16} &= -\Gamma_\uparrow^*(-\omega_3) - \Gamma_\uparrow(-\omega_3).
\end{aligned} \tag{4.51}$$

Introducing an XY coupling breaks a system symmetry and so causes three of the four zero eigenvalues given in Equation 4.50 to take on finite (although very small)

values (see Figure 4.12). This break in degeneracy means the system can no longer support steady state coherences, however it still supports a potentially extremely long lived nuclear coherence. The remaining zero eigenvalue is associated with the state $|\downarrow\downarrow\rangle$, which is now the only steady state.

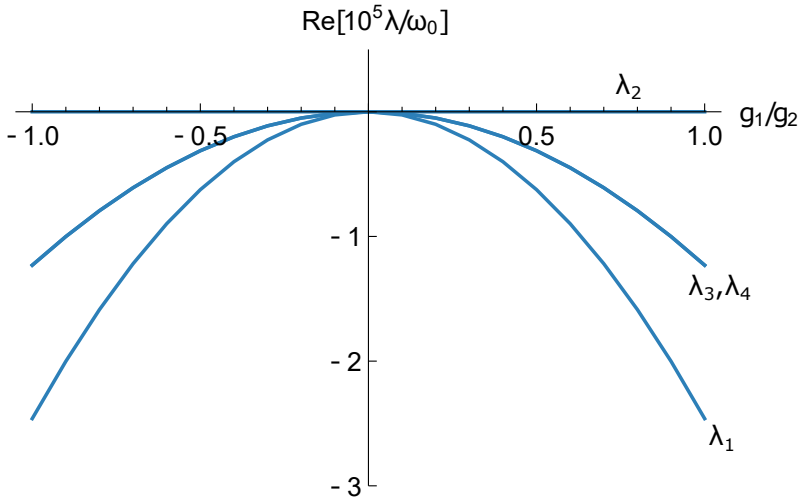

Figure 4.12: The variation of the real parts of the four smallest Liouvillian eigenvalues with g_1, the XY coupling strength. One eigenvalue remains at zero throughout; this corresponds to the steady state solution. The other three eigenvalues have a quadratic dependence on g_1. Two of these remain degenerate; they are plotted in the upper branch. The fourth eigenvalue is in the lower branch. The typical electron decay rate $\gamma_0 = 0.08\omega_0$ and $g_2 = 0.025\omega_0$.

All of the eigenvalues except the zero eigenvalue show a quadratic dependence on XY coupling strength, however this dependence is extremely weak. Changing between Ising and isotropic coupling causes a variation of around 0.01 % of the real parts of the twelve eigenvalues in Equation 4.51. Although the change in eigenvalues is very small, the fact that they are now not zero means that after a long enough time, the nuclear spin coherence will decay.

That introducing XY coupling into our model has a small impact on the Liouvillian eigenvalues and so the long-term behaviour of the system is to be expected if we consider the energy scales of the system. The electron Zeeman splitting is much larger than the

XY coupling strength, so the mixing angle θ is very small and the change in decay rates is small.

To understand the quadratic dependence of the decay rates on the XY coupling strength, let us consider the decay rate of the coherence $\rho_{\downarrow\downarrow,\downarrow\uparrow}(t)$ in the XY model using perturbation theory. Figure 4.13 shows how initial nuclear coherences are destroyed. The nuclear superposition is retained during electronic decay, however the $|\downarrow\uparrow\rangle$ state is mixed with $|\uparrow\downarrow\rangle$, which then decays to $|\downarrow\downarrow\rangle$ (the only true steady state).

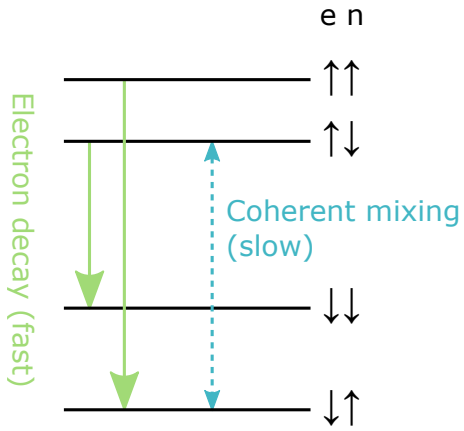

Figure 4.13: The computational basis states of the electron-nuclear spin system. When XY coupling is included there is coherent mixing between the states $|\uparrow\downarrow\rangle$ and $|\downarrow\uparrow\rangle$ (blue). This mixing is much slower than the electronic decay (green).

The overall decay rate of $\rho_{\downarrow\downarrow,\downarrow\uparrow}(t)$ can be roughly estimated by the population which is mixed back into $|\uparrow\downarrow\rangle$, multiplied by the electronic decay rate. The coherent mixing between the states $|\uparrow\downarrow\rangle$ and $|\downarrow\uparrow\rangle$ gives a first order correction δ_1 to the $|\uparrow\downarrow\rangle$ state. This correction is of the order of the coupling strength between the two states, divided by the zeroth order difference in their eigenvalues:

$$\delta_1 \sim \frac{\langle\uparrow\downarrow|H_S^{XY}|\downarrow\uparrow\rangle}{\langle\uparrow\downarrow|H_S|\uparrow\downarrow\rangle - \langle\downarrow\uparrow|H_S|\downarrow\uparrow\rangle} \sim \frac{g_1}{\omega_0}, \tag{4.52}$$

where the perturbed and unperturbed Hamiltonians are given by Equations 4.45 and 4.1 respectively.

The population mixed back into $|\uparrow\downarrow\rangle$ is therefore of the order $(g_1/\omega_0)^2$. The electronic decay rate is of order γ_0, so the overall coherence decay rates (and therefore the real part of the Liouvillian eigenvalues) are quadratic in XY coupling strength.

Secularisation

As discussed in Section 3.4.5, secularising the Born-Markov master equation guarantees that the density matrix will remain physical – it will be Hermitian, completely positive and have unit trace (see Section 2.2.2 for a discussion of these properties). However if the emission spectra from different transitions overlap, then secularisation removes physical coherence terms from the master equation. We did not use the secular approximation in the derivation of Equation 4.40; here we will examine the consequences of applying secularisation to this master equation on the nuclear coherences. For further discussion on secularisation of master equations, see Eastham *et al.* [102].

When we secularise Equation 4.40, all the differential equations given in Equation 4.42 remain the same except for the nuclear coherence element $\rho_{\downarrow\downarrow,\downarrow\uparrow}(t)$, which now remains constant at its initial value.

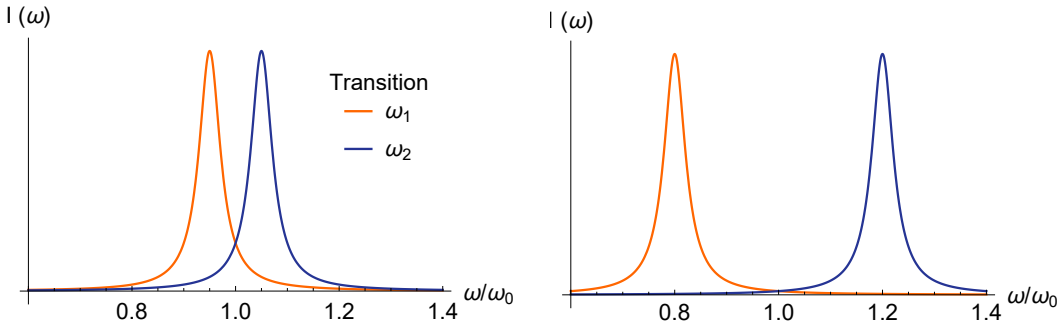

Figure 4.14: Sample transition spectra represented by Lorentzian distributions with linewidths equal to the typical electron decay rate $\gamma_0 = 0.05\omega_0$, centred at the transition frequencies ω_1 (orange) and ω_2 (blue). Left: at $g = 0.025\omega_0$, there is significant overlap between the transitions, corresponding to coherences that would be discounted under secularisation. Right: at $g = 0.1\omega_0$, there is little overlap between transitions and secularisation has less effect.

Thus in the secularised equations of motion, no nuclear coherences can survive when the electron spin flips. As some coherences are physically expected to survive electronic decay, secularisation is not appropriate here. This is further confirmed if we look at sample transition spectra (Figure 4.14). For small values of g (left), the two transition spectra overlap and in the unsecularised master equation significant coherences can be preserved (see Figure 4.6). Increasing the hyperfine coupling (right) separates the spectra, reducing the steady state coherences and meaning that secularisation has less impact.

When is it safe to secularise?

Consider the general case of a quantum system with N transitions, described by a Born-Markov quantum master equation with N^2 terms. Secularising between all pairs of transitions would produce a master equation with N terms. When secularising, it is necessary to consider each pair of transitions separately. In general, the terms pertaining to the pair of transitions ω_A and ω_B may be secularised if:

$$|\omega_A - \omega_B| \gg \frac{1}{2}\big(\Gamma(\omega_A) + \Gamma(\omega_B)\big), \tag{4.53}$$

where $\Gamma(\omega) = N(\omega)\, J(\omega)$.

4.4 Conclusions

In this Chapter, we have found that:

- Highly off-resonant hybrid qubit systems such as the coupled nuclear-electron spin system can provide excellent coherence protection.
- Nuclear coherences are preserved when the hyperfine coupling is small compared to the electron decay rate, so that the two transitions corresponding to an electron spin flip are nearly resonant.
- At zero temperature, the steady state can be found exactly by working in the single-excitation subspace.
- The zero-temperature dynamics can be found by solving the non-secular Born-Markov master equation.
- The Born-Markov steady state agrees very well with the exact solution within our parameter regime, so in the next Chapter we will extend the Born-Markov approach to finite temperature and look at the resultant system behaviour.

Chapter 5

The Coupled Nuclear-Electron Spin System – Finite Temperature

---

One doesn't seek the absolute 'Truth'. One seeks instead the highest quality intellectual explanation of things with the knowledge that if the past is any guide to the future this explanation must be taken provisionally; as useful until something better comes along.

Robert M. Pirsig

In Chapter 4 we saw that highly off-resonant coupled qubit systems are capable of providing excellent coherence protection even as one part of the coupled system decays. We were able to treat this system exactly at zero temperature by working in the single excitation subspace, though this method is not easily extended to finite temperature. We also modelled the system using Born-Markov master equations, and the results agreed extremely well with the exact solution. Here we extend the Born-Markov treatment of the system used in Chapter 4 to finite temperature and examine its behaviour.

5.1 Recap of system

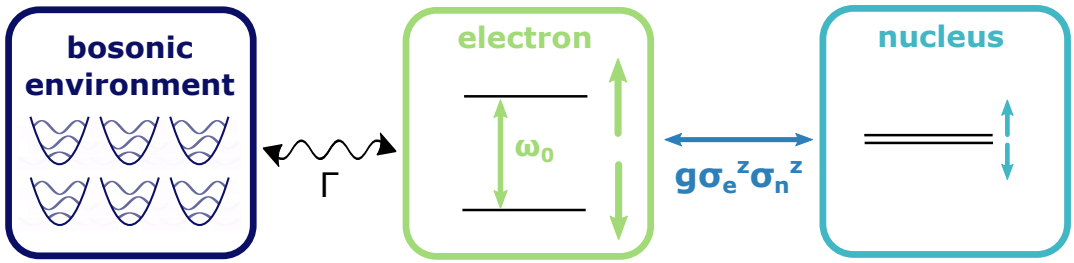

Figure 5.1: A reminder of the system covered in this and the preceding Chapter. Now the environment is in thermal equilibrium at a temperature T, so the electron spin may be re-excited by the bath.

In this Chapter we continue to use the coupled nuclear-electron spin system (Figure 5.1) as a model for understanding the behaviour of hybrid open quantum systems with multiple energy scales. The hyperfine coupling is of Ising form and secularisation will not be used in the derivation of the master equations (for a fuller understanding of these assumptions, see Section 4.3.2).

We will model the environment as a series of quantum harmonic oscillators, with the occupation of different modes at temperature T determined by the Bose-Einstein distribution function $n(\omega) = \left(e^{\hbar\omega/k_B T} - 1\right)^{-1}$. Except where stated otherwise, the environment is assumed to have an Ohmic spectral density of the form given in Equation 4.39 which peaks at the bare electron splitting frequency.

5.2 The Born-Markov master equation at finite temperature

5.2.1 Born-Markov solution

To obtain the master equation, we follow the procedure outlined in Section 3.4, resulting in the Born-Markov equation in the interaction picture (Equation 3.33):

$$\begin{aligned}\frac{d}{dt}\rho(t) = \sum_{n,m=1,2} e^{i(\omega_m-\omega_n)t}\Big(&\Gamma_\uparrow(\omega_m)\Big(A_m^\dagger\rho(t)A_n - A_nA_m^\dagger\rho(t)\Big)\\ &+\Gamma_\uparrow^*(\omega_n)\Big(A_m^\dagger\rho(t)A_n - \rho(t)A_nA_m^\dagger\Big)\\ &+\Gamma_\downarrow(\omega_n)\Big(A_n\rho(t)A_m^\dagger - A_m^\dagger A_n\rho(t)\Big)\\ &+\Gamma_\downarrow^*(\omega_m)\Big(A_n\rho(t)A_m^\dagger - \rho(t)A_m^\dagger A_n\Big)\Big).\end{aligned} \tag{5.1}$$

The relevant transition frequencies and operators are (Equation 4.7):

$$\begin{aligned}\omega_1 &= \omega_0 - 2g, & \omega_2 &= \omega_0 + 2g,\\ A_1 &= |{\downarrow\downarrow}\rangle\langle{\uparrow\downarrow}|, & A_2 &= |{\downarrow\uparrow}\rangle\langle{\uparrow\uparrow}|\,.\end{aligned} \tag{5.2}$$

The transition rates (Equation 3.45) depend on the spectral density $J(\omega)$ and the occupation function $n(\omega)$:

$$\Gamma_\uparrow(\omega) = J(\omega)n(\omega) + \frac{i}{\pi}\mathcal{P}\int_0^\infty \frac{J(\phi)n(\phi)}{\phi-\omega}d\phi,$$

$$\Gamma_\downarrow(\omega) = J(\omega)[n(\omega)+1] - \frac{i}{\pi}\mathcal{P}\int_0^\infty \frac{J(\phi)[n(\phi)+1]}{\phi-\omega}d\phi. \tag{5.3}$$

The resulting coupled differential equations are similar to those given in Equa-

tion 4.42, but with additional terms representing re-excitement of the system:

$$\begin{aligned}
\dot{\rho}_{\uparrow\uparrow,\uparrow\uparrow}(t) &= -\dot{\rho}_{\downarrow\uparrow,\downarrow\uparrow}(t) = -2\,\mathbb{R}[\Gamma_{\downarrow}(\omega_2)]\rho_{\uparrow\uparrow,\uparrow\uparrow}(t) + 2\,\mathbb{R}[\Gamma_{\uparrow}(\omega_2)]\rho_{\downarrow\uparrow,\downarrow\uparrow}(t),\\
\dot{\rho}_{\uparrow\downarrow,\uparrow\downarrow}(t) &= -\dot{\rho}_{\downarrow\downarrow,\downarrow\downarrow}(t) = -2\,\mathbb{R}[\Gamma_{\downarrow}(\omega_1)]\rho_{\uparrow\downarrow,\uparrow\downarrow}(t) + 2\,\mathbb{R}[\Gamma_{\uparrow}(\omega_1)]\rho_{\downarrow\downarrow,\downarrow\downarrow}(t),\\
\dot{\rho}_{\uparrow\downarrow,\uparrow\uparrow}(t) &= -\big(\Gamma_{\downarrow}(\omega_1) + \Gamma^*_{\downarrow}(\omega_2)\big)\rho_{\uparrow\downarrow,\uparrow\uparrow}(t) + e^{-4igt}\big(\Gamma_{\uparrow}(\omega_1) + \Gamma^*_{\uparrow}(\omega_2)\big)\rho_{\downarrow\downarrow,\downarrow\uparrow}(t),\\
\dot{\rho}_{\downarrow\downarrow,\downarrow\uparrow}(t) &= e^{4igt}\big(\Gamma_{\downarrow}(\omega_1) + \Gamma^*_{\downarrow}(\omega_2)\big)\rho_{\uparrow\downarrow,\uparrow\uparrow}(t) - \big(\Gamma_{\uparrow}(\omega_1) + \Gamma^*_{\uparrow}(\omega_2)\big)\rho_{\downarrow\downarrow,\downarrow\uparrow}(t),\\
\dot{\rho}_{\uparrow\uparrow,\downarrow\downarrow}(t) &= -\big(\Gamma_{\downarrow}(\omega_2) + \Gamma^*_{\uparrow}(\omega_1)\big)\rho_{\uparrow\uparrow,\downarrow\downarrow}(t),\\
\dot{\rho}_{\uparrow\uparrow,\downarrow\uparrow}(t) &= -\big(\Gamma_{\downarrow}(\omega_2) + \Gamma^*_{\uparrow}(\omega_2)\big)\rho_{\uparrow\uparrow,\downarrow\uparrow}(t),\\
\dot{\rho}_{\uparrow\downarrow,\downarrow\downarrow}(t) &= -\big(\Gamma_{\downarrow}(\omega_1) + \Gamma^*_{\uparrow}(\omega_1)\big)\rho_{\uparrow\downarrow,\downarrow\downarrow}(t),\\
\dot{\rho}_{\uparrow\downarrow,\downarrow\uparrow}(t) &= -\big(\Gamma_{\downarrow}(\omega_1) + \Gamma^*_{\uparrow}(\omega_2)\big)\rho_{\uparrow\downarrow,\downarrow\uparrow}(t),
\end{aligned} \tag{5.4}$$

and $\dot{\rho}_{n,m}(t) = \dot{\rho}^*_{m,n}(t)$. The solutions for the elements which contain nuclear coherences are (in the interaction picture):

$$\begin{aligned}
\rho_{\downarrow\downarrow,\downarrow\uparrow}(t) &= \left[r_{\downarrow\downarrow,\downarrow\uparrow}(e^{-\kappa_- t} - e^{-\kappa_+ t}) + \rho_{\downarrow\downarrow,\downarrow\uparrow}(0)e^{-\kappa_+ t}\right],\\
\rho_{\uparrow\downarrow,\uparrow\uparrow}(t) &= \left[r_{\uparrow\downarrow,\uparrow\uparrow}(e^{-\kappa_- t} - e^{-\kappa_+ t}) + \rho_{\uparrow\downarrow,\uparrow\uparrow}(0)e^{-\kappa_+ t}\right] e^{-4igt}.
\end{aligned} \tag{5.5}$$

Here we have defined the following quantities:

$$\gamma_{\downarrow} = \Gamma_{\downarrow}(\omega_1) + \Gamma^*_{\downarrow}(\omega_2), \qquad \gamma_{\uparrow} = \Gamma_{\uparrow}(\omega_1) + \Gamma^*_{\uparrow}(\omega_2), \tag{5.6}$$

$$\kappa_{\pm} = \frac{1}{2}\left[\gamma_{\uparrow} + \gamma_{\downarrow} - 4ig \pm \sqrt{(\gamma_{\uparrow} + \gamma_{\downarrow} - 4ig)^2 + 16ig\gamma_{\uparrow}}\right], \tag{5.7}$$

$$r_{\downarrow\downarrow,\downarrow\uparrow} = \frac{\gamma_{\downarrow}\rho_{\uparrow\downarrow,\uparrow\uparrow}(0) + (\kappa_+ - \gamma_{\uparrow})\rho_{\downarrow\downarrow,\downarrow\uparrow}(0)}{\kappa_+ - \kappa_-}, \qquad r_{\uparrow\downarrow,\uparrow\uparrow} = r_{\downarrow\downarrow,\downarrow\uparrow}\Big(\frac{\gamma_{\uparrow} - \kappa_-}{\gamma_{\downarrow}}\Big). \tag{5.8}$$

5.2.2 Finite-temperature Born-Markov dynamics

The finite-temperature nuclear coherence dynamics (Equation 5.5) are governed by two temperature-dependent decay rates, $\mathbb{R}[\kappa_{\pm}(T)]$ (Equation 5.7), and two temperature-dependent amplitudes, $r_{\uparrow\downarrow,\uparrow\uparrow}(T)$ and $r_{\downarrow\downarrow,\downarrow\uparrow}(T)$ (Equation 5.8). The decay rates and amplitudes are plotted in Figure 5.2 using an Ohmic spectral density with $\omega_0 = \omega_c$.

In the limit of zero temperature $\gamma_{\uparrow} = 0$, so the decay rates simplify to:

$$\kappa_{\pm}(T=0) = [\gamma_{\downarrow} - 4ig]\frac{(1 \pm 1)}{2}, \tag{5.9}$$

and the amplitudes are:

$$\rho_{\downarrow\downarrow,\downarrow\uparrow}(t \to \infty)\Big|_{T=0} = r_{\downarrow\downarrow,\downarrow\uparrow}, \qquad |\rho_{\uparrow\downarrow,\uparrow\uparrow}(t \to \infty)|\Big|_{T=0} = |r_{\uparrow\downarrow,\uparrow\uparrow}|. \tag{5.10}$$

As $\kappa_{-}(T = 0) = 0$, there is only one zero-temperature decay rate, κ_{+}, which represents the electronic decay rate. (This is in agreement with the zero temperature solution presented in Chapter 4, Equation 4.43.) At finite temperature, we must consider both emission and absorption processes and the interference between them. We can no longer think of $\kappa_{\pm}$ as purely representing either electronic decay or excitation processes; they are related to two system decay timescales. If these timescales are significantly different, then a quasi steady state (QSS) exists once the faster decay has occurred on timescale $\mathbb{R}[\kappa_{+}]^{-1}$.

There are three finite-temperature regimes within Figure 5.2, and sample dynamics from each regime have been plotted in Figure 5.3. These regimes are:

1. Low temperature (light blue),
2. Intermediate temperature (dark green),
3. High temperature (light green).

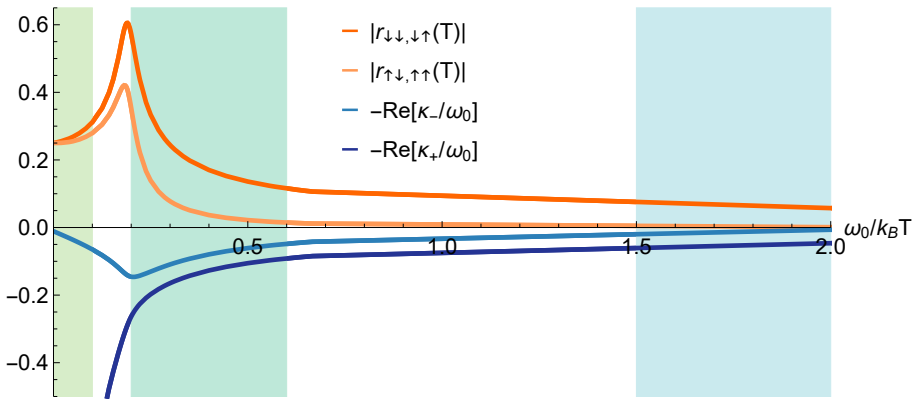

Figure 5.2: The temperature dependence of the amplitudes r and decay rates $\mathbb{R}[\kappa]$ of the quasi steady state nuclear coherences, for $g = 0.1\omega_0$, $\gamma_0 = 0.02\omega_0$, $\rho_{\uparrow\downarrow,\uparrow\uparrow}(0) = 1/2$, $\rho_{\downarrow\downarrow,\downarrow\uparrow}(0) = 0$. A QSS is only observed when $\mathbb{R}[\kappa_-]$ is sufficiently small. There is a QSS at low temperature (blue shaded region, right), which disappears at intermediate temperature (dark green region, middle). At very high temperature (light green region, left) the QSS returns. The dynamics of the three regimes are plotted in Figure 5.3.

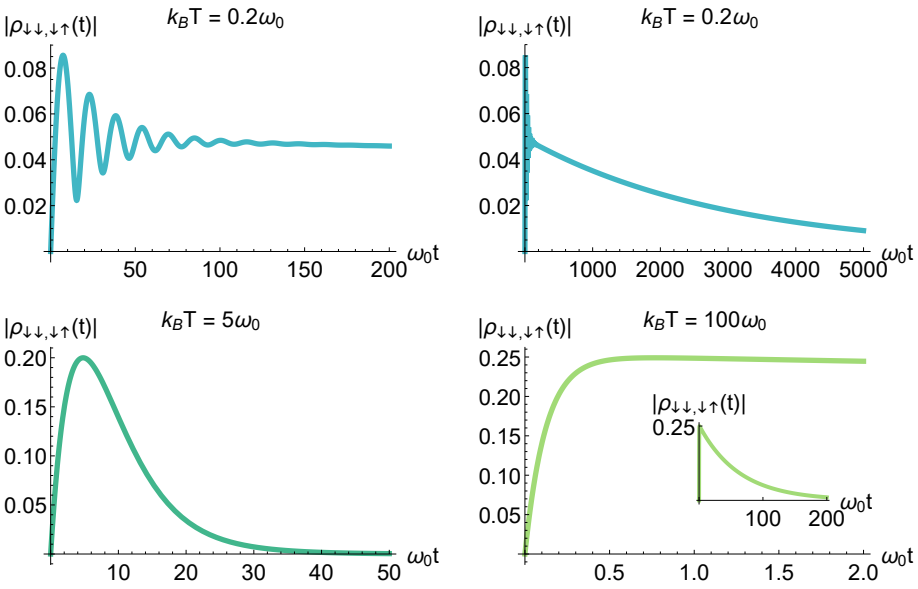

Figure 5.3: The lower nuclear coherence dynamics in each of the three temperature regimes in Figure 5.2: low temperature (blue plots, top), intermediate (dark green, bottom left) and high (light green, bottom right). At low temperature there is a QSS (top-left) which decays slowly (top-right). At intermediate temperature there is no QSS. A QSS returns at high temperature; the QSS coherence amplitude is much larger than that observed at low temperature, although the decay timescales are shorter.

Low (but finite) temperature

Over short timescales (Figure 5.3, top left) the low-temperature nuclear coherence dynamics are essentially the same as in the zero temperature case. For the coupling strengths chosen, the transition spectra are partially resolved, so as the electron decays some information about the nuclear spin is revealed. At zero temperature this is the only decay process, so steady state nuclear coherences survive.

At finite temperature, we must also consider re-excitation of the electron via absorption of environmental photons. The re-excited electron then decays again, revealing more information about the nuclear spin. At low temperatures, this additional process takes place over a much longer timescale than the original decay (Figure 5.3, top right). This separation of decay rates (Figure 5.2, right shaded region) gives rise to QSS nuclear coherences.

Intermediate temperature

Raising the temperature increases the rate at which the electron decays and re-excites, until we reach a point where both decay rates are comparable to one another and to g (Figure 5.2, middle shaded region). The rates are still slow enough that significant information about the nuclear spin is revealed during each emission. As there is no longer any timescale separation, the QSS disappears.

The rise in temperature broadens the transition spectra so that less information is revealed on each emission, so the amplitudes r increase. However if we look at the dynamics (Figure 5.3, bottom left), we see that the lower nuclear coherence never actually reaches $r_{\downarrow\downarrow,\downarrow\uparrow}$ as there is no QSS in this regime. At these temperatures, r is not really a coherence measure, which explains why it can exceed the theoretical maximum coherence of $1/2$.

High temperature

As we raise the temperature still further, we enter a third regime (Figure 5.2, left shaded region). Here the electron decays very quickly, revealing very little information about the nuclear spin state (for further discussion of this, see Section 4.3.1). Here the system decay rates $\gamma_\uparrow, \gamma_\downarrow$ are much larger than the hyperfine coupling g. The coherence decay rates defined in Equation 5.7 are:

$$\kappa_\pm = \frac{1}{2}\left[\gamma_\uparrow + \gamma_\downarrow - 4ig \pm (\gamma_\uparrow + \gamma_\downarrow)\sqrt{1 + \frac{8ig(\gamma_\uparrow - \gamma_\downarrow) - 16g^2}{(\gamma_\uparrow + \gamma_\downarrow)^2}}\right], \tag{5.11}$$

In the high temperature regime:

$$1 \gg \mathbb{R}\left[\frac{8ig(\gamma_\uparrow - \gamma_\downarrow) - 16g^2}{(\gamma_\uparrow + \gamma_\downarrow)^2}\right] \gg \mathbb{I}\left[\frac{8ig(\gamma_\uparrow - \gamma_\downarrow) - 16g^2}{(\gamma_\uparrow + \gamma_\downarrow)^2}\right], \tag{5.12}$$

so we neglect the imaginary part inside the square root in Equation 5.11 and expand to second order in g, using that for $\delta \ll 1$, $(1+\delta)^{1/2} = 1 + \delta/2 - \delta^2/8 + \mathcal{O}[\delta^3]$:

$$\sqrt{1 + \frac{8ig(\gamma_\uparrow - \gamma_\downarrow) - 16g^2}{(\gamma_\uparrow + \gamma_\downarrow)^2}} \approx 1 + \frac{4ig(\gamma_\uparrow - \gamma_\downarrow)}{(\gamma_\uparrow + \gamma_\downarrow)^2} + \frac{8g^2}{(\gamma_\uparrow + \gamma_\downarrow)^2}\left(\frac{(\gamma_\uparrow - \gamma_\downarrow)^2}{(\gamma_\uparrow + \gamma_\downarrow)^2} - 1\right). \tag{5.13}$$

At high temperature, $\gamma_\uparrow - \gamma_\downarrow$ (which is imaginary) is much smaller than $\gamma_\uparrow + \gamma_\downarrow$, and so the first-order g term can be neglected. The real parts of $\kappa_\pm$ are then:

$$\mathbb{R}[\kappa_\pm] \approx \frac{1}{2}\left[\gamma_\uparrow + \gamma_\downarrow \pm \left(\gamma_\uparrow + \gamma_\downarrow - \frac{32g^2\gamma_\uparrow\gamma_\downarrow}{(\gamma_\uparrow + \gamma_\downarrow)^3}\right)\right]. \tag{5.14}$$

Note that at high temperature, $n(\omega) \gg 1$ and so $\Gamma_\uparrow(\omega) \approx \Gamma_\downarrow^*(\omega)$ for all frequencies of interest. This means that the quantities $\gamma_\uparrow + \gamma_\downarrow \approx 2\,\mathbb{R}[\Gamma_\uparrow(\omega_1) + \Gamma_\uparrow(\omega_2)]$ and $\gamma_\uparrow\gamma_\downarrow \approx |\Gamma_\uparrow(\omega_1)|^2 + |\Gamma_\uparrow(\omega_2)|^2 + 2\,\mathbb{R}[\Gamma_\uparrow(\omega_1)\Gamma_\uparrow(\omega_2)]$ are real.

In the high temperature regime, the two nuclear decoherence rates approximate to:

$$\mathbb{R}[\kappa_+] \approx \gamma_\uparrow + \gamma_\downarrow, \qquad \mathbb{R}[\kappa_-] \approx \frac{16g^2\gamma_\uparrow\gamma_\downarrow}{(\gamma_\uparrow + \gamma_\downarrow)^3}. \tag{5.15}$$

Again, we have entered a regime where the two decay rates are separated by several orders of magnitude as g is much smaller than the rates $\gamma_\uparrow$ and $\gamma_\downarrow$. This separation can be seen in the left shaded region of Figure 5.2, and the returned quasi steady state is plotted in Figure 5.3, bottom right.

The timescale of QSS decay (in terms of the inverse bare electron splitting) is much shorter at high temperature than it is at low temperature. This is not important so long as any required quantum computations can be performed before the QSS decays. Crucially, at high temperature the QSS exists for a long time compared to the time initially taken to reach the QSS, providing sufficient time for quantum gates to be applied.

At high temperature, the magnitude of the QSS nuclear coherence is much larger than that at low temperature. At high temperature, the system decay rates $\gamma_\uparrow \sim \gamma_\downarrow$ are much larger than the spin-spin coupling, so the transitions are indistinguishable. Indeed, in the high temperature limit each of the two QSS coherence magnitudes $r_{\updownarrow\downarrow,\updownarrow\uparrow}$ are half of the initial nuclear coherence. They add in phase, so that the magnitude of the coherence in the QSS is the same as that in the initial state. In contrast, at low temperature the decay rates are much smaller than g, so the transitions are quite distinct.

At first glance, this might seem surprising – quantum effects are normally washed out at high temperature. However we can gain some understanding if we re-consider the system using the perspective of overlapping transitions used in Chapter 4. Increasing the environmental temperature increases the transition linewidths and therefore increases the overlap between the two transitions. The transitions become less well-resolved and larger nuclear coherences can be preserved. In this way, increasing the temperature can help to protect nuclear coherences.

5.2.3 High-temperature limitations of the Born-Markov solution

The increase in transition linewidth with increasing temperature also has implications for the validity of the Born-Markov solution. As discussed in Chapter 4 (Section 4.3.2), increasing the transition linewidths leads to a regime where the spectral density varies significantly over the linewidth. Once this occurs, the Born-Markov approximation breaks down. This is shown in Figure 5.4. It is worth noting that the temperature regime required for coherence protection is independent of the temperature regime where the Born-Markov approximation fails, so that with judicious choice of variables, it is possible to achieve significant coherence protection whilst remaining in the Born-Markov regime.

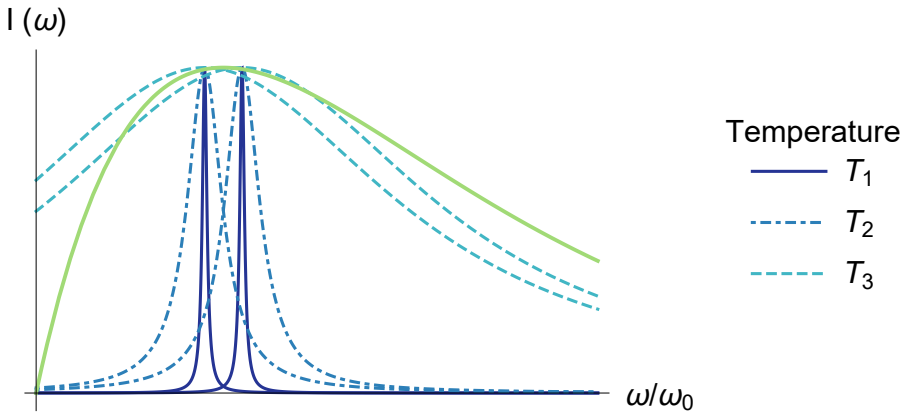

Figure 5.4: Sample emission spectra of two transitions, plotted for three temperaures $T_1 < T_2 < T_3$. Also plotted is the spectral density $J(\omega)$ (light green solid line). The emission spectra are of Lorentzian form with half-width $\Gamma(\omega) = J(\omega)n(\omega)$. At very low temperature (T_1), the two transitions are separable ($\Gamma(\omega) \gg g$) and little nuclear coherence is preserved. By raising the temperature (T_2), we enter a regime where the transitions overlap ($\Gamma(\omega) \sim g$) and coherences are protected. Note that here the Born-Markov approximation still holds as the transition rate $\Gamma(\omega)$ is still much smaller than the spectral density half-width. The Born-Markov approximation breaks down around T_3, when the transition linewidths and spectral density half-width become comparable.

The argument given above provides a first insight into the failure of the Born-Markov solution at high temperature. However it assumes that, whilst the linewidths change with temperature, the bath remains the same. To understand the effects of temperature on

the bath, it is convenient to shift from frequency-space into the time domain. At low temperature, the system decay timescale τ_S is much longer than the bath correlation time τ_B, and so the Born-Markov approximation is valid. Increasing the temperature reduces the system decay timescale. As the system decay timescale approaches the bath correlation time ($\tau_S \sim \tau_B$), the Born-Markov solution breaks down.

Increasing the temperature has a complex effect on the bath correlation time; however we can be sure that τ_B doesn't increase with increasing temperature (it may be reduced or stay constant) [116]. The frequency-space argument used above implicitly assumes that τ_B remains constant as the temperature increases. If τ_B were to decrease as the temperature was raised, then the temperature at which $\tau_S = \tau_B$ would be greater than that for constant τ_B. The breakdown of the Born-Markov solution would occur at a higher temperature than that estimated using the frequency-space argument.

Therefore, the frequency-space argument allows us to calculate the lowest temperature at which the Born-Markov solution may break down. Let us look at a transition centred on the bare electron splitting ω_0 with linewidth $\Gamma(\omega_0) \approx J(\omega_0)n(\omega_0)$. We may define a critical temperature for the breakdown of the Born-Markov approximation T_c which occurs when the spectral linewidths are half the spectral density width $\mathcal{W}$:

$$\mathcal{W} = 2J(\omega_0)\left(\mathrm{Exp}\left[\frac{\omega_0}{k_B T_c}\right] - 1\right)^{-1}. \tag{5.16}$$

Rearranging for T_c:

$$T_c = \frac{\omega_0}{k_B}\left(\ln\left[\frac{2J(\omega_0)}{\mathcal{W}} + 1\right]\right)^{-1}. \tag{5.17}$$

We will use the standard deviation as a measure of width, such that:

$$\begin{aligned}\mathcal{W} &= \sqrt{\langle\omega^2\rangle - \langle\omega\rangle^2}, \\ &= \sqrt{\frac{\int J(\omega)\omega^2 d\omega}{\int J(\omega)d\omega} - \left(\frac{\int J(\omega)\omega d\omega}{\int J(\omega)d\omega}\right)^2}.\end{aligned} \tag{5.18}$$

For an Ohmic spectral density peaked at the electron splitting and peak height $\gamma_0/\omega_0 = 0.02$ (as used in Figures 5.2 and 5.3), the spectral density width $\mathcal{W} \approx 1.4\omega_0$, giving a breakdown temperature of $k_B T_c \approx 36\omega_0$. This is a higher temperature than that at which we expect to see some coherence recovery (see Figure 5.2).

It is important to remember that the breakdown temperature is unconnected to the temperature at which the QSS returns and nuclear coherences are enhanced. The temperature at which the QSS returns is determined by the separation of the decay rates $\kappa_\pm$, themselves dependent on the complex transition rates $\Gamma(\omega)$ and the hyperfine coupling. The breakdown temperature is dependent on the bath's characteristics; in particular the cutoff frequency ω_c and the peak height γ_0. To further explore the validity of the Born-Markov solution at high temperature and gain further insight, we now turn to a semiclassical approach.

5.3 The semiclassical model

At high temperature, any electron coherences are quickly lost to the bath, allowing us to describe it as a classical two state system which fluctuates between spin-up and spin-down. We will use random telegraph noise to model the electron spin fluctuations, and we will compare the results obtained using our semiclassical model to those from the Born-Markov solution.

5.3.1 Derivation of the semiclassical result

Random telegraph noise

Random telegraph noise (RTN) is a process where a variable randomly switches back and forth between two different states. Over a long period of time, the probability distribution function of the switching times is Poissonian [125]. Here the relevant stochastic

variable is ω_n, the nuclear spin splitting. As the electron spin flips, the sign of the nuclear splitting also switches: $\omega_n(t) = \pm 2g$. The nuclear spin coherence is given by:

$$C_n(t) = C_n(0)\left\langle \exp\left[i\int_0^t \omega_n(s)ds\right]\right\rangle, \tag{5.19}$$

where $C_n(0)$ is the initial nuclear coherence and $\langle\cdots\rangle$ indicates the ensemble average. To evaluate this, we use Kubo's Theorem [126]:

$$\begin{aligned}\left\langle \exp\left[i\int_a^b x(t)dt\right]\right\rangle \\ = \exp\left[\sum_{n=1}^{\infty} i^n \int_a^b dt_1 \int_a^{t_1} dt_2 \cdots \int_a^{t_{n-1}} dt_n \big\langle\big\langle x(t_1)x(t_2)\cdots x(t_n)\big\rangle\big\rangle\right],\end{aligned} \tag{5.20}$$

where $\langle\langle\cdots\rangle\rangle$ indicates the cumulant. The first and second-order cumulants can be calculated using [127]:

$$\big\langle\big\langle x(t)\big\rangle\big\rangle = \left[\frac{d}{dk}\ln\langle e^{kx(t)}\rangle\right]_{k=0}, \tag{5.21}$$

$$\big\langle\big\langle x(t_1)x(t_2)\big\rangle\big\rangle = \left[\frac{d^2}{dk_1dk_2}\ln\langle e^{k_1x(t_1)+k_2x(t_2)}\rangle\right]_{k_i=0}. \tag{5.22}$$

The ensemble average is the probability weighted average, so for any continuous function $f(x)$ we may write:

$$\langle f(x)\rangle = \int_{-\infty}^{\infty} p(x)f(x)dx, \tag{5.23}$$

where $p(x)$ is the probability distribution function.

Odd-ordered cumulants

The single cumulant given in Equation 5.21 is:

$$\langle\langle x(t_1)\rangle\rangle \equiv \langle\langle x_1\rangle\rangle = \left[\frac{d}{dk}\left(\ln\left(\int p(x_1)e^{kx_1}dx_1\right)\right)\right]_{k=0}. \tag{5.24}$$

Now we may use the property that for any continuous and non-zero valued function $f(x)$:

$$\frac{d\ln(f(x))}{dx} = \frac{df(x)/dx}{f}. \tag{5.25}$$

Applying this to Equation 5.24, we obtain:

$$\langle\langle x_1\rangle\rangle = \left[\frac{\frac{d}{dk}\left(\int p(x_1)e^{kx_1}dx_1\right)}{\int p(x_1)e^{kx_1}dx_1}\right]_{k=0}. \tag{5.26}$$

To evaluate Equation 5.22, it is helpful to swap the order of the differential and the integral in the numerator, allowing us to differentiate:

$$\langle\langle x_1\rangle\rangle = \left[\frac{\left(\int p(x_1)x_1e^{kx_1}dx_1\right)}{\int p(x_1)e^{kx_1}dx_1}\right]_{k=0}. \tag{5.27}$$

Now we may evaluate this at $k = 0$ (using the normalisation condition $\int p(x)dx = 1$):

$$\langle\langle x_1\rangle\rangle = \langle x_1\rangle. \tag{5.28}$$

In this case, since the stochastic variable is the nuclear spin splitting and $\langle\omega_n(t)\rangle = 0$, all odd-ordered cumulants are zero.

Even-ordered cumulants

The second-order cumulant can be found in the same manner. Using Equations 5.22 and 5.23, we obtain:

$$\begin{aligned}
\langle\langle x_1 x_2 \rangle\rangle &= \left[\frac{d^2}{dk_1 dk_2} \ln\left(\iint p(x_1,x_2) e^{k_1 x_1 + k_2 x_2} dx_1 dx_2\right)\right]_{k_i=0}, \\
&= \left[\frac{d}{dk_2}\left(\frac{\iint p(x_1,x_2) x_1 e^{k_1 x_1 + k_2 x_2} dx_1 dx_2}{\iint p(x_1,x_2) e^{k_1 x_1 + k_2 x_2} dx_1 dx_2}\right)\right]_{k_i=0}, \\
&= \iint p(x_1,x_2) x_1 x_2 dx_1 dx_2 \\
&\quad - \left(\iint p(x_1,x_2) x_1 dx_1 dx_2\right)\left(\iint p(x_1,x_2) x_2 dx_1 dx_2\right), \\
&= \langle x_1 x_2 \rangle - \langle x_1 \rangle \langle x_2 \rangle. \qquad (5.29)
\end{aligned}$$

As all odd-ordered cumulants are zero here, $\langle\langle \omega_n(t_1)\omega_n(t_2)\rangle\rangle = \langle \omega_n(t_1)\omega_n(t_2)\rangle$. Similarly, the fourth-order cumulant is:

$$\begin{aligned}
\big\langle\big\langle \omega_n(t_1)\omega_n(t_2)\omega_n(t_3)\omega_n(t_4)\big\rangle\big\rangle =& \big\langle \omega_n(t_1)\omega_n(t_2)\omega_n(t_3)\omega_n(t_4)\big\rangle \\
&- \big\langle \omega_n(t_1)\omega_n(t_2)\big\rangle\big\langle \omega_n(t_3)\omega_n(t_4)\big\rangle \\
&- \big\langle \omega_n(t_1)\omega_n(t_3)\big\rangle\big\langle \omega_n(t_2)\omega_n(t_4)\big\rangle \\
&- \big\langle \omega_n(t_1)\omega_n(t_4)\big\rangle\big\langle \omega_n(t_2)\omega_n(t_3)\big\rangle. \qquad (5.30)
\end{aligned}$$

Evaluating joint moments

For a Poissonian distribution with an average rate of event occurrence λ, the probability of observing k events in the time interval $(0, t)$ is [128]:

$$P(k \text{ events in interval } t) = e^{-\lambda t}\frac{(\lambda t)^k}{k!}. \tag{5.31}$$

In this case, the event is the flipping of the sign of ω_n. The probability that the nuclear spin splitting at time t_1 is the same as that at time t_2 is given by:

$$\begin{aligned} P\left[\omega_n(t_1) = 2g \mid \omega_n(t_2) = 2g\right] &= P\left[\omega_n(t_1) = -2g \mid \omega_n(t_2) = -2g\right], \\ &= e^{-\lambda(t_1 - t_2)}\cosh\left(\lambda(t_1 - t_2)\right), \qquad \text{for } t_2 \leq t_1, \end{aligned} \tag{5.32}$$

and the probability of the splitting being different from that at time t_1 is:

$$\begin{aligned} P\left[\omega_n(t_1) = 2g \mid \omega_n(t_2) = -2g\right] &= P\left[\omega_n(t_1) = -2g \mid \omega_n(t_2) = 2g\right], \\ &= e^{-\lambda(t_1 - t_2)}\sinh\left(\lambda(t_1 - t_2)\right). \end{aligned} \tag{5.33}$$

For a stochastic variable $x(t) = \pm 1$, the autocorrelation function (also known as the joint moment) is the weighted distribution [128]:

$$\left\langle x(t_1)x(t_2)\right\rangle = \sum_{j=0}^{1}\sum_{k=0}^{1} x_j x_k P\left[x(t_2) = x_k\right] \times P\left[x(t_1) = x_j \mid x(t_2) = x_k\right], \tag{5.34}$$

where $t_2 \leq t_1$ and the two values x can take are $x_0 = -1$ and $x_1 = 1$. By expanding out the above sum and using Equations 5.32 and 5.33, we find:

$$\left\langle x(t_1)x(t_2)\right\rangle = e^{2(t_2 - t_1)\lambda}, \qquad \text{for } t_2 \leq t_1. \tag{5.35}$$

The fourth-order autocorrelation function is (for $t_4 \leq t_3 \leq t_2 \leq t_1$):

$$\big\langle x(t_1)x(t_2)x(t_3)x(t_4)\big\rangle = e^{2(t_2-t_1+t_4-t_3)\lambda} = \big\langle x(t_1)x(t_2)\big\rangle\big\langle x(t_3)x(t_4)\big\rangle. \tag{5.36}$$

The nuclear spin coherence

To obtain an expression for the nuclear spin coherence, we now need to insert the relevant autocorrelation functions into Kubo's Theorem using $\omega_n(t) = 2gx(t)$, and perform the relevant integrals. The second-order term of the right-hand side of Equation 5.20 is:

$$\begin{aligned}\int_0^t dt_1 \int_0^{t_1} dt_2 \big\langle\big\langle \omega_n(t_1)\omega_n(t_2)\big\rangle\big\rangle =& 4g^2 \int_0^t dt_1 \int_0^{t_1} dt_2 \big\langle x(t_1)x(t_2)\big\rangle, \\ =& 4g^2 \int_0^t dt_1 \int_0^{t_1} dt_2 e^{2(t_2-t_1)\lambda}, \\ =& \frac{g^2}{\lambda^2}\left(e^{-2\lambda t} + 2\lambda t - 1\right). \end{aligned} \tag{5.37}$$

The fourth-order term from Kubo's Theorem is:

$$\begin{aligned}&\int_0^t dt_1 \int_0^{t_1} dt_2 \int_0^{t_2} dt_3 \int_0^{t_3} dt_4 \big\langle\big\langle \omega_n(t_1)\omega_n(t_2)\omega_n(t_3)\omega_n(t_4)\big\rangle\big\rangle \\ &\quad = 16g^4 \int_0^t dt_1 \int_0^{t_1} dt_2 \int_0^{t_2} dt_3 \int_0^{t_3} dt_4 \\ &\qquad \Big(\big\langle x(t_1)x(t_2)x(t_3)x(t_4)\big\rangle - \big\langle x(t_1)x(t_2)\big\rangle\big\langle x(t_3)x(t_4)\big\rangle \\ &\qquad - \big\langle x(t_1)x(t_3)\big\rangle\big\langle x(t_2)x(t_4)\big\rangle - \big\langle x(t_1)x(t_4)\big\rangle\big\langle x(t_2)x(t_3)\big\rangle\Big). \end{aligned} \tag{5.38}$$

Using Equations 5.35 and 5.36:

$$\begin{aligned}\big\langle x(t_1)x(t_2)x(t_3)x(t_4)\big\rangle &= \big\langle x(t_1)x(t_2)\big\rangle\big\langle x(t_3)x(t_4)\big\rangle, \\ \big\langle x(t_1)x(t_3)\big\rangle\big\langle x(t_2)x(t_4)\big\rangle &= \big\langle x(t_1)x(t_4)\big\rangle\big\langle x(t_2)x(t_3)\big\rangle. \end{aligned} \tag{5.39}$$

Equation 5.38 then becomes:

$$\begin{aligned}\int_0^t dt_1 \int_0^{t_1} dt_2 \int_0^{t_2} dt_3 \int_0^{t_3} dt_4 \big\langle\big\langle \omega_n(t_1)\omega_n(t_2)\omega_n(t_3)\omega_n(t_4)\big\rangle\big\rangle \\ = -32g^4 \int_0^t dt_1 \int_0^{t_1} dt_2 \int_0^{t_2} dt_3 \int_0^{t_3} dt_4 e^{2(t_3+t_4-t_1-t_2)\lambda}, \\ = -\frac{g^4}{2\lambda^4}\left(e^{-4\lambda t} - 5 + 4\lambda t + e^{-2\lambda t}(4+8\lambda t)\right). \end{aligned} \tag{5.40}$$

By using Equations 5.38 and 5.40, along with the expression for $C_n(t)$ given in Equation 5.19, we can now obtain the nuclear coherence to fourth order in g:

$$\begin{aligned}\frac{C_n(t)}{C_n(0)} &= \left\langle \exp\left[i\int_0^t \omega_n(s)ds\right]\right\rangle, \\ &\approx \exp\left[-\frac{g^2}{\lambda^2}\left(e^{-2\lambda t} + 2\lambda t - 1\right) - \frac{g^4}{2\lambda^4}\left(e^{-4\lambda t} - 5 + 4\lambda t + e^{-2\lambda t}(4+8\lambda t)\right)\right]. \end{aligned} \tag{5.41}$$

We are interested in the behaviour of the nuclear spin coherence on timescales much greater than the inverse of the electron decay rate, i.e. $\lambda t \gg 1$. Then the nuclear coherence is:

$$C_n(t) = C_n(0)\exp\left[-\frac{2g^2 t}{\lambda}\left(1 + \frac{g^2}{\lambda^2}\right)\right]. \tag{5.42}$$

If the electron fluctuation rate is sufficiently fast ($g/\lambda \ll 1$), then the fourth-order term is small in comparison to the second-order term and the nuclear coherence decays exponentially with rate $\kappa_{SC} = 2g^2/\lambda$. At high temperatures, the electron fluctuation rate is assumed to be independent of the nuclear spin state such that the decay rate is $2J(\omega_0)(n(\omega_0+1))$ and the excitation rate is $2J(\omega_0)n(\omega_0)$. For high temperature, $n(\omega_0) \gg 1$, so that decay and excitation happen at approximately the same rate $\lambda = 2J(\omega_0)n(\omega_0)$. Then the semiclassical nuclear coherence decay rate is:

$$\kappa_{SC} = \frac{g^2}{J(\omega_0)n(\omega_0)}. \tag{5.43}$$

Note that κ_{SC} decreases with increasing temperature, so that the decay time is longer at high temperature. This phenomenon is also seen in the motional narrowing effect in nuclear magnetic resonance imaging (NMR). In NMR, the magnetic field experienced by a nuclear spin is subject to local fluctuations. Each spin in the sample has a different splitting, leading to inhomogeneous broadening of the resonant frequency linewidth. At high temperatures, each nucleus experiences a magnetic field that varies in time due to thermal motion. This time averaging reduces the variation in spin splitting across the sample, narrowing the resonant frequency linewidth [129].

5.3.2 Comparison of quantum and semiclassical results

High temperature behaviour

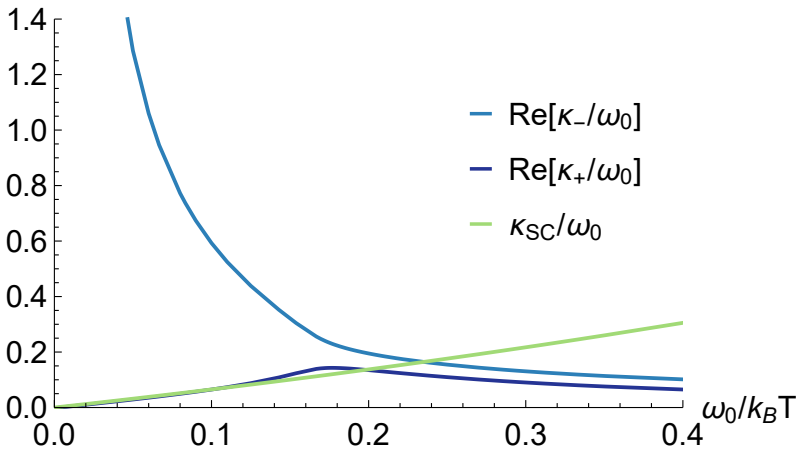

Figure 5.5: The semiclassical coherence decay rate κ_{SC} found using the random telegraph noise model (green). Also plotted are the two quantum decay rates $\kappa_{\pm}$ (dark and light blue). At high temperature ($\omega_0/k_BT < 0.1$), the semiclassical rate agrees well with κ_{-}. The spectral density used here is subohmic ($s = 1/2$) and peaks at $3\omega_0$.

Figure 5.5 compares the semiclassical decay rate κ_{SC} and the two Born-Markov quantum decay rates $\kappa_{\pm}$ as defined in Equation 5.7 (Section 5.2.1). The spectral density

used to plot Figure 5.5 is subohmic:

$$J(\omega) = \gamma_0 \left(\frac{\omega}{\omega_c}\right)^s \exp\left[s\left(1 - \frac{\omega}{\omega_c}\right)\right], \tag{5.44}$$

with $\gamma_0 = 0.02\omega_0$, $\omega_c = 3\omega_0$, and $s = 1/2$.

At high temperature ($k_B T \gtrsim 10\omega_0$), there is good agreement between the semi-classical decay rate and κ_-, the slower quantum decay rate. The high-temperature approximation for κ_- is (Equation 5.15):

$$\mathbb{R}[\kappa_-] \approx \frac{16 g^2 \gamma_\uparrow \gamma_\downarrow}{(\gamma_\uparrow + \gamma_\downarrow)^3}. \tag{5.45}$$

As discussed in Section 5.3.1, at high temperatures we may assume that $\gamma_\downarrow \approx \gamma_\uparrow = 2J(\omega_0)n(\omega_0)$, so that the quantum rate can be written:

$$\mathbb{R}[\kappa_-] \approx \frac{g^2}{J(\omega_0)n(\omega_0)} = \kappa_{SC}, \tag{5.46}$$

and so we expect to see good high-temperature agreement as shown in Figure 5.5.

Validity of the Markov approximation

As discussed in Section 5.2.3, we can assess the high-temperature validity of the Born-Markov approximation for the quantum model by comparing the spectral density width $\mathcal{W}$ (calculated using Equation 5.18) with the transition linewidths (the rates κ). The spectral density used in Figure 5.5 has a width $\mathcal{W} = 7.3\omega_0$. The decay rates must be significantly smaller than this for the Markov approximation to remain valid. Taking $\kappa_\pm < 0.2\mathcal{W}$ as a limit of the range of validity, we see from Figure 5.5 that the Born-Markov approximation is valid for $\omega_0/k_B T > 0.05$.

For the parameters chosen in Figure 5.5, the Born-Markov approximation remains valid well into the high-temperature QSS regime. The return of the QSS at high tem-

peratures is therefore not an artefact of the breakdown of the Born-Markov model, but is a real physical effect.

The semiclassical and quantum results agree well for $\omega_0/k_BT < 0.1$, so there is a temperature regime $0.05 < \omega_0/k_BT < 0.1$ where the semiclassical result agrees with the quantum result *and* the quantum result remains valid. Since the semiclassical result makes the correct prediction here, and both models agree for all temperatures $k_BT > 10\omega_0$, we can conclude that the decoherence rate continues to fall as the temperature is raised. However both the quantum and the semiclassical result rely on Markovianity, which fails at very high temperatures.

5.4 Conclusions

In this Chapter, we have found that:

- Extending the Born-Markov approach to finite temperature produces two decoherence rates, resulting in a quasi steady state if the rates are well separated.
- Small coherences are protected in a QSS at low temperature; this QSS disappears as the temperature is raised.
- At high temperature the QSS returns and much larger coherences are preserved than at low temperature.
- At high temperature, heating the system increases the nuclear coherence time.
- Increasing the temperature still further causes the Born-Markov approximation to break down. Here the quantum and semiclassical results agree; however they might both be wrong at the highest temperatures since both contain an implicit assumption of Markovianity.

Chapter 6

Discussion and Conclusion

Nature's music is never over; her silences are pauses, not conclusions.

Mary Webb

Here we discuss the implications of the results presented in this Thesis. We consider experimental candidate systems for observing coherence protection and suggest a theoretical technique for looking inside non-Markovian regimes.

6.1 Experimental possibilities

In this Thesis we have seen that coherences in coupled two-qubit systems can be protected under certain circumstances. To observe coherence protection, the two qubits should be highly off-resonant ($\omega_A \gg \omega_B$) and qubit B should have a much longer coherence time than qubit A. This separation of energy scales is commonly found in hybrid systems.

In addition, there are different system requirements depending upon the experimental scenario chosen:

Low temperature: Here the qubit coupling should be tunable and the transition linewidths should be fixed. Then the qubit coupling can be varied to change the transition spacing. One would expect that the greater the transition overlap, the greater the coherence preservation.

Variable temperature: Here the qubit coupling should be strong compared to the zero-temperature environmental coupling, so that at low temperature the transitions are well separated. As the temperature is increased, the linewidths are broadened, increasing coherence protection.

Here we consider two promising avenues for the implementation of coherence protection.

6.1.1 Quantum dots (QDs)

The main advantage of quantum dot systems is that they are extremely tunable and can be engineered such that the transition spacings are comparable to the linewidths. A single quantum dot can be coupled to a photonic-crystal cavity [130]; the cavity mode is highly detuned from the QD. The electron spin in the QD plays the role of low energy qubit previously denoted as "nuclear spin" in this Thesis. The coupling to photons is then via exciton states – so in a sense the exciton is the high energy qubit here. There are four optical transitions in this hybrid spin-photon system, although two are suppressed due to their polarisation. The remaining two transitions have linewidths of $\sim$18 μeV and are separated by $\sim$50 μeV (a factor of 2.8 greater than the linewidths) [130].

To achieve coherence protection, we must be able to tune the environmental coupling to the exciton. This can be done using the Purcell effect – the enhancement of the spontaneous emission rate due to the environment. Purcell enhancement can be used to broaden the linewidths of optical QD transitions by a factor of up to 6.7 [131]. If Purcell

enhancement were applied to the coupled QD-cavity system, then the optical transitions would overlap significantly, protecting coherences stored within the QD.

6.1.2 NV centres

NV centres are another promising qubit candidate, and offer long room-temperature coherence times. The NV centre has a single negative charge which can be optically pumped using spin selective transitions. The electron spin plays the role of the low energy qubit and the optical transition the role of the high energy qubit. The spin sublevel splitting can be tuned in zero applied magnetic field by applying an external electric field, and this can be detected using a direct readout technique called photocurrent detection of magnetic resonance (PDMR) [132]. In PDMR, charge carriers which have been excited from NV centres into the conduction band are detected electrically. PDMR can be performed on a chip, improving the scalability of this approach.

NV centres can form part of a tunable coupled quantum system when placed inside a highly off-resonant cavity. The NV centre-cavity coupling can be tuned by means of piezoelectric actuators (devices that use piezoelectric crystals to control movement) [133]. The cavity can be tuned to enhance the emission rate of the NV centre by up to 40% [133], increasing the transition linewidths and thus engineering coherence protection.

6.2 Future calculations

As seen in Chapter 5, there are strong indications that increasing the temperature of a coupled quantum system can provide enhanced coherence protection. We have found high-temperature coherence protection using quantum and semiclassical models, both of which rely on the Markovian approximation. This high-temperature coherence protection is present within the Markovian regime; however we cannot rely on these models to draw

any firm conclusions about non-Markovian behaviour at very high temperature.

TEMPO (Time Evolving Matrix Product Operator) [116] is a numerically exact method discussed in Chapter 3.5 which could be used to provide more insight into the non-Markovian behaviour of coupled systems at very high temperatures. As the coupled qubit system studied in this Thesis is heated, the system decay time is reduced and we enter a non-Markovian regime as the system decay time approaches the bath memory time. By using TEMPO, one could incorporate bath memory effects that occur on similar timescales to the system decay processes. At very high temperatures, these bath memory effects could have a significant impact on system behaviour and so this method could be used to provide new insights into coupled open quantum systems.

Bibliography

[1] R. White. *How Computers Work*. Pearson Education, 2015.

[2] G. E. Moore. Cramming more components onto integrated circuits. *Electronics*, 38, 1965.

[3] Windell Oskay from Sunnyvale, CA, USA (Bell Labs 004). CC BY 2.0 (http://creativecommons.org/licenses/by/2.0), via Wikimedia Commons. [Online; accessed 1 Feb 2017].

[4] S. O. Kasap. *Principles of Electronic Materials and Devices, Second Edition*. McGraw-Hill, 2001.

[5] The Nobel Foundation. The Nobel Prize in Physics 1956. http://www.nobelprize.org/nobel_prizes/physics/laureates/1956/. [Online; accessed 12 Dec 2016].

[6] Intel. http://farm6.static.flickr.com/5184/5687918041_c9c5309bb2_b.jpg. Reproduced with written permission from Intel. [Online; accessed 1 Feb 2017].

[7] Intel. Intel 14nm Technology. http://www.intel.co.uk/content/www/uk/en/silicon-innovations/intel-14nm-technology.html. [Online; accessed 12 Dec 2016].

[8] M. Mitchell Waldrop. The chips are down for Moore's Law. *Nature*, 530:144–147, 2016.

[9] R. P. Feynman. Simulating physics with computers. *International Journal of Theoretical Physics*, 21:467–488, 1982.

[10] D. Deutsch. Quantum theory, the Church-Turing principle and the universal quantum computer. *Proceedings of the Royal Society of London A*, 400:97–117, 1985.

[11] M. A. Nielsen and I. L. Chuang. *Quantum Computation and Quantum Information*. Cambridge University Press, 2000.

[12] P. W. Shor. Algorithms for Quantum Computation: Discrete Logarithms and Factoring. *Proceedings of the 35th Annual Symposium on Foundations of Computer Science*, 124–134, 1994.

[13] L. K. Grover. Quantum Mechanics helps in searching for a needle in a haystack. *Physical Review Letters*, 79:325–328, 1997.

[14] E. Gibney. Physics: Quantum computer quest. *Nature*, 516:24–26, 2014.

[15] S. Barnett. *Quantum Information*. Oxford Master Series in Physics. Oxford University Press, 2009.

[16] B. Hensen, H. Bernien, A. E. Dréau, A. Reiserer, N. Kalb, M. S. Blok, J. Ruitenberg, R. F. L. Vermeulen, R. N. Schouten, C. Abellán, W. Amaya, V. Pruneri, M. W. Mitchell, M. Markham, D. J. Twitchen, D. Elkouss, S. Wehner, T. H. Taminiau, and R. Hanson. Loophole-free Bell inequality violation using electron spins separated by 1.3 kilometres. *Nature*, 526:682–686, 2015.

[17] P. Kok and B. W. Lovett. *Introduction to Optical Quantum Information Processing*. Cambridge University Press, 2010.

[18] Sankar Das Sarma, Michael Freedman, and Chetan Nayak. Topologically protected qubits from a possible non-abelian fractional quantum hall state. *Physical Review Letters*, 94:166802, Apr 2005.

[19] D. P. DiVincenzo. The Physical Implementation of Quantum Computation. *Fortschritte der Physik*, 48:771–783, 2000.

[20] A. Barenco, C. H. Bennett, R. Cleve, D. P. DiVincenzo, N. Margolus, H. Weinfurter, T. Sleator, J. A. Smolin, and P. Shor. Elementary gates for quantum computation. *Physical Review A*, 52:3457–3467, 1995.

[21] K. Saeedi, S. Simmons, J. Z. Salvail, P. Dluhy, H. Riemann, N. V. Abrosimov, P. Becker, H.-J. Pohl, J. J. L. Morton, and M. L. W. Thewalt. Room-temperature quantum bit storage exceeding 39 minutes using ionized donors in silicon-28. *Science*, 342:830–833, 2013.

[22] A. M. Tyryshkin, S. Tojo, J. J. L. Morton, H. Riemann, N. V. Abrosimov, P. Becker, H.-J. Pohl, T. Schenkel, M. L. W. Thewalt, K. M. Itoh, and S. A. Lyon. Electron spin coherence exceeding seconds in high-purity silicon. *Nature Materials*, 11:143–7, 2012.

[23] J. J. L. Morton, D. R. McCamey, M. A. Eriksson, and S. A. Lyon. Embracing the quantum limit in silicon computing. *Nature*, 479:345–353, 2011.

[24] A. J. Sigillito, A. M. Tyryshkin, T. Schenkel, A. A. Houck, and S. A. Lyon. All-electric control of donor nuclear spin qubits in silicon. *Nature Nanotechnology*, 12:958–962, 2017.

[25] J. J. Pla, K. Y. Tan, J. P. Dehollain, W. H. Lim, J. J .L. Morton, F. A. Zwanenburg, D. N. Jamieson, A. S. Dzurak, and A. Morello. High-fidelity readout and control of a nuclear spin qubit in silicon. *Nature*, 496:334–338, 2013.

[26] G. W. Morley, M. Warner, A. M. Stoneham, P. T. Greenland, J. van Tol, C. W. M. Kay, and G. Aeppli. Initializing, manipulating and storing quantum information with bismuth dopants in silicon. *Nature Materials*, 9:725–729, 2010.

[27] A. Schweiger and G. Jeschke. *Principles of Pulse Electron Paramagnetic Resonance*. Oxford University Press, 2001.

[28] S. Simmons, H. Wu, and J. J. L. Morton. Controlling and exploiting phases in multi-spin systems using electron spin resonance and nuclear magnetic resonance. *Philosophical transactions of the Royal Society A*, 370:4794–4809, 2012.

[29] M. Zhong, M. P. Hedges, R. L. Ahlefeldt, J. G. Bartholomew, S. E. Beavan, S. M. Wittig, J. J. Longdell, and M. J. Sellars. Optically addressable nuclear spins in a solid with a six-hour coherence time. *Nature*, 517:177–181, 2015.

[30] M. W. Doherty, N. B. Manson, P. Delaney, F. Jelezko, J. Wrachtrup, and L. C. L. Hollenberg. The nitrogen-vacancy colour centre in diamond. *Physics Reports*, 528:1–45, 2013.

[31] T. Ladd, F. Jelezko, R. Laflamme, Y. Nakamura, C. Monroe, and J. O'Brien. Quantum computers. *Nature*, 464:45–53, 2010.

[32] L. Robledo, Ha. Bernien, I. Van Weperen, and R. Hanson. Control and coherence of the optical transition of single nitrogen vacancy centers in diamond. *Physical Review Letters*, 105:177403, 2010.

[33] N. Bar-Gill, L. M. Pham, A. Jarmola, D. Budker, and R. L. Walsworth. Solid-state electronic spin coherence time approaching one second. *Nature Communications*, 4:1743, 2013.

[34] N. Y. Yao, L. Jiang, A. V. Gorshkov, P. C. Maurer, G. Giedke, J. I. Cirac, and M. D. Lukin. Scalable architecture for a room temperature solid-state quantum information processor. *Nature Communications*, 3:800, 2012.

[35] S. R. Schofield, N. J. Curson, M. Y. Simmons, F. J. Ruess, T. Hallam, L. Oberbeck, and R. G. Clark. Atomically precise placement of single dopants in Si. *Physical Review Letters*, 91(13), 2003.

[36] L. Goldstein, F. Glas, J. Y. Marzin, M. N. Charasse, and G. Le Roux. Growth by molecular beam epitaxy and characterization of InAs/GaAs strained-layer superlattices. *Applied Physics Letters*, 47:1099–1101, 1985.

[37] D. Loss and D. P. DiVincenzo. Quantum Computation with Quantum Dots. *Physical Review A*, 57:120–126, 1998.

[38] S. C. Benjamin, B. W. Lovett, and J. M. Smith. Prospects for measurement-based quantum computing with solid state spins. *Laser & Photonics Review*, 3:556–574, 2009.

[39] C. C. Lo and J. J. L. Morton. Silicon's Second Act. *IEEE Spectrum*, 51:37–43, 2014.

[40] E. Kawakami, T. Jullien, P. Scarlino, D. R. Ward, D. E. Savage, M. G. Lagally, V. V. Dobrovitski, Mark Friesen, S. N. Coppersmith, M. A. Eriksson, and L. M. K. Vandersypen. Gate fidelity and coherence of an electron spin in a Si/SiGe quantum dot with micromagnet. *Proceedings of the National Academy of Sciences*, 113:11738–11743, 2016.

[41] J. Clarke and F. K. Wilhem. Superconducting quantum bits. *Nature*, 453:1031–1042, 2008.

[42] M. H. Devoret and R. J. Schoelkopf. Superconducting circuits for quantum computation. *Science*, 339:1169–1174, 2013.

[43] E. Lucero, R. Barends, Y. Chen, J. Kelly, M. Mariantoni, A. Megrant, P. O'Malley, D. Sank, A. Vainsencher, J. Wenner, T. White, Y. Yin, A. N. Cleland, and J. M. Martinis. Computing prime factors with a Josephson phase qubit quantum processor. *Nature Physics*, 8:719–723, 2012.

[44] J. Kelly, R. Barends, A. G. Fowler, A. Megrant, E. Jeffrey, T. C. White, D. Sank, J. Y. Mutus, B. Campbell, Y. Chen, Z. Chen, B. Chiaro, A. Dunsworth, I.-C. Hoi, C. Neill, P. J. J. O 'Malley, C. Quintana, P. Roushan, A. Vainsencher, J. Wenner, A. N. Cleland, and J. M. Martinis. State preservation by repetitive error detection in a superconducting quantum circuit. *Nature*, 519:66–69, 2015.

[45] J. M. Gambetta, J. M. Chow, and M. Steffen. Building logical qubits in a superconducting quantum computing system. *NPJ Quantum Information*, 3(2), 2017.

[46] M. H. Devoret, A. Wallraff, and J. M. Martinis. Superconducting qubits: A short review. *arXiv*, cond-mat/0411174v1, 2004.

[47] A. G. Fowler, A. M. Stephens, and P. Groszkowski. High-threshold universal quantum computation on the surface code. *Physical Review A*, 80(052312), 2009.

[48] L. Allen, S.M. Barnett, and M.J. Padgett. *Optical Angular Momentum*. Optics & Optoelectronics. Taylor & Francis, 2003.

[49] J. L. O'Brien. Optical quantum computing. *Science*, 318:1567–1571, 2007.

[50] J.-W. Pan, M. Daniell, S. Gasparoni, G. Weihs, and A. Zeilinger. Experimental demonstration of four-photon entanglement and high-fidelity teleportation. *Physical Review Letters*, 86:4435–4438, 2001.

[51] Z. Zhao, Y.-A. Chen, A.-N. Zhang, T. Yang, H. J. Briegel, and J.-W. Pan. Experimental demonstration of five-photon entanglement and open-destination teleportation. *Nature*, 430:54–58, 2004.

[52] M. Eibl, S. Gaertner, M. Bourennane, C. Kurtsiefer, M. Żukowski, and H. Weinfurter. Experimental observation of four-photon entanglement from parametric down-conversion. *Physical Review Letters*, 90:200403, 2003.

[53] T. E. Northup and R. Blatt. Quantum information transfer using photons. *Nature Photonics*, 8:356–363, 2014.

[54] X.-S. Ma, T. Herbst, T. Scheidl, D. Wang, S. Kropatschek, W. Naylor, B. Wittmann, A. Mech, J. Kofler, E. Anisimova, V. Makarov, T. Jennewein, R. Ursin, and A. Zeilinger. Quantum teleportation over 143 kilometres using active feed-forward. *Nature*, 489:269–73, 2012.

[55] E. Knill, R. Laflamme, and G. J. Milburn. A scheme for efficient quantum computation with linear optics. *Nature*, 409:46–52, 2001.

[56] J. L. O'Brien, G. J. Pryde, A. G. White, T. C. Ralph, and D. Branning. Demonstration of an all-optical quantum controlled-NOT gate. *Nature*, 426:264, 2003.

[57] H. He, J. Wu, and X. Zhu. An introduction to all-optical quantum controlled-not gates. In *Advanced Computer Architecture*, pages 157–173. Springer Singapore, 2016.

[58] S. Bernon, H. Hattermann, D. Bothner, M. Knufinke, P. Weiss, F. Jessen, D. Cano, M. Kemmler, R. Kleiner, D. Koelle, and J. Fortágh. Manipulation and coherence of ultra-cold atoms on a superconducting atom chip. *Nature Communications*, 4:2380, 2013.

[59] D. Wineland, C. Monroe, W. Itano, D. Leibfried, B. King, and D. Meekhof. Experimental issues in coherent quantum-state manipulation of trapped atomic ions. *Journal of Research of the National Institute of Standards and Technology*, 103:259–328, 1998.

[60] T. Monz, D. Nigg, E. A. Martinez, M. F. Brandl, P. Schindler, R. Rines, S. X. Wang, I. L. Chuang, and R. Blatt. Realization of a scalable Shor algorithm. *Science*, 351:1068–1070, 2016.

[61] F. Haas, J. Volz, R. Gehr, J. Reichel, and J. Estève. Entangled States of More Than 40 Atoms in an Optical Fiber Cavity. *Science*, 344:180–183, 2014.

[62] R. McConnell, H. Zhang, J. Hu, S. Ćuk, and V. Vuletić. Entanglement with negative Wigner function of almost 3,000 atoms heralded by one photon. *Nature*, 519:439–442, 2015.

[63] K. R. Brown, J. Kim, and C. Monroe. Co-designing a scalable quantum computer with trapped atomic ions. *NPJ Quantum Information*, 2:16034, 2016.

[64] G. Kurizki, P. Bertet, Y. Kubo, K. Mølmer, D. Petrosyan, P. Rabl, and J. Schmiedmayer. Quantum technologies with hybrid systems. *Proceedings of the National Academy of Sciences*, 112:3866–3873, 2015.

[65] J. J. L. Morton and B. W. Lovett. Hybrid Solid-State Qubits: The Powerful Role of Electron Spins. *Annual Review of Condensed Matter Physics*, 2:189–212, 2011.

[66] L. Jiang, J. S. Hodges, J. R. Maze, P. Maurer, J. M. Taylor, D. G. Cory, P. R. Hemmer, R. L. Walsworth, A. Yacoby, A. S. Zibrov, and M. D. Lukin. Repetitive Readout of a Single Electronic Spin via Quantum Logic with Nuclear Spin Ancillae. *Science*, 326:267–272, 2009.

[67] W. Pfaff, T. H. Taminiau, L. Robledo, H. Bernien, M. L. Markham, D. J. Twitchen, and R. Hanson. Demonstration of entanglement-by-measurement of solid state qubits. *Nature Physics*, 9:29–33, 2012.

[68] L. Childress, M. V. G. Dutt, J. M. Taylor, A. S. Zibrov, F. Jelezko, J. Wrachtrup, P. R. Hemmer, and M. D. Lukin. Coherent dynamics of coupled electron and nuclear spin qubits in diamond. *Science*, 314:281–285, 2006.

[69] P. C. Maurer, G. Kucsko, C. Latta, L. Jiang, N. Y. Yao, S. D. Bennett, F. Pastawski, D. Hunger, N. Chisholm, M. Markham, D. J. Twitchen, J. I. Cirac, and M. D. Lukin. Room-Temperature Quantum Bit Memory Exceeding One Second. *Science*, 336:1283–1286, 2012.

[70] G. D. Fuchs, G. Burkard, P. V. Klimov, and D. D. Awschalom. A quantum memory intrinsic to single nitrogenvacancy centres in diamond. *Nature Physics*, 7:789–793, 2011.

[71] V. V. Dobrovitski, G. D. Fuchs, A. L. Falk, C. Santori, and D. D. Awschalom. Quantum Control over Single Spins in Diamond. *Annual Review of Condensed Matter Physics*, 4:23–50, 2013.

[72] M. V. G. Dutt, L. Childress, L. Jiang, E. Togan, J. Maze, F. Jelezko, A. S. Zibrov, P. R. Hemmer, and M. D. Lukin. Quantum Register Based on Individual Electronic and Nuclear Spin Qubits in Diamond. *Science*, 316:1312–1316, 2007.

[73] P. Neumann, J. Beck, M. Steiner, F. Rempp, H. Fedder, P. R. Hemmer, J. Wrachtrup, and F. Jelezko. Single-Shot Readout of a Single Nuclear Spin. *Science*, 329:542–544, 2010.

[74] T. van der Sar, Z. H. Wang, M. S. Blok, H. Bernien, T. H. Taminiau, D. M. Toyli, D. A. Lidar, D. D. Awschalom, R. Hanson, and V. V. Dobrovitski. Decoherence-protected quantum gates for a hybrid solid-state spin register. *Nature*, 484:82–86, 2012.

[75] J. J. L. Morton, A. M. Tyryshkin, R. M. Brown, S. Shankar, B. W. Lovett, A. Ardavan, T. Schenkel, E. E. Haller, J. W. Ager, and S. A. Lyon. Solid-state quantum memory using the 31P nuclear spin. *Nature*, 455:1085–1088, 2008.

[76] F. A. Zwanenburg, A. S. Dzurak, A. Morello, M. Y. Simmons, L. C. L. Hollenberg, G. Klimeck, S. Rogge, S. N. Coppersmith, and M. A. Eriksson. Silicon quantum electronics. *Reviews of Modern Physics*, 85:961–1019, 2013.

[77] A. Morello, J. J. Pla, F. A. Zwanenburg, K. W. Chan, H. Huebl, M. Möttönen, C. D. Nugroho, C. Yang, J. A. van Donkelaar, A. D. C. Alves, D. N. Jamieson, C. C. Escott, L. C. L. Hollenberg, R. G. Clark, and A. S. Dzurak. Single-shot readout of an electron spin in silicon. *Nature*, 467:687–691, 2010.

[78] W. B. Gao, A. Imamoglu, H. Bernien, and R. Hanson. Coherent manipulation, measurement and entanglement of individual solid-state spins using optical fields. *Nature Photonics*, 9:363–373, 2015.

[79] E. B. Flagg, A. Muller, S. V. Polyakov, A. Ling, A. Migdall, and G. S. Solomon. Interference of single photons from two separate semiconductor quantum dots. *Physical Review Letters*, 104(137401), 2010.

[80] R. B. Patel, A. J. Bennett, I. Farrer, C. A. Nicoll, D. A. Ritchie, and A. J. Shields. Two-photon interference using electrically tunable remote quantum dots. *Proceedings of SPIE*, 7948, 2011.

[81] X. Li, Y. Wu, D. Steel, D. Gammon, T. Stievater, D. Katzer, D. Park, C. Piermarocchi, and L. J. Sham. An All-Optical Quantum Gate in a Semiconductor Quantum Dot. *Science*, 301:809–811, 2003.

[82] D. Press, T. D. Ladd, B. Zhang, and Y. Yamamoto. Complete quantum control of a single quantum dot spin using ultrafast optical pulses. *Nature*, 456:218–221, 2008.

[83] W. B. Gao, P. Fallahi, E. Togan, J. Miguel-Sanchez, and A. Imamoglu. Observation of entanglement between a quantum dot spin and a single photon. *Nature*, 491:426–430, 2012.

[84] K. De Greve, L. Yu, P. L. McMahon, J. S. Pelc, C. M. Natarajan, N. Y. Kim, E. Abe, S. Maier, C. Schneider, M. Kamp, S. Höfling, R. H. Hadfield, A. Forchel, M. M. Fejer, and Y. Yamamoto. Quantum-dot spinphoton entanglement via frequency downconversion to telecom wavelength. *Nature*, 491:421–425, 2012.

[85] J. R. Schaibley, A. P. Burgers, G. A. McCracken, L. M. Duan, P. R. Berman, D. G. Steel, A. S. Bracker, D. Gammon, and L. J. Sham. Demonstration of quantum entanglement between a single electron spin confined to an InAs quantum dot and a photon. *Physical Review Letters*, 110(167401), 2013.

[86] K. De Greve, P. L. McMahon, L. Yu, J. S. Pelc, C. Jones, C. M. Natarajan, N. Y. Kim, E. Abe, S. Maier, C. Schneider, M. Kamp, S. Höfling, R. H. Hadfield, A. Forchel, M. M. Fejer, and Y. Yamamoto. Complete tomography of a high-fidelity solid-state entangled spinphoton qubit pair. *Nature Communications*, 4:2228, 2013.

[87] W. B. Gao, P. Fallahi, E. Togan, A. Delteil, Y. S. Chin, J. Miguel-Sanchez, and A. Imamoğlu. Quantum teleportation from a propagating photon to a solid-state spin qubit. *Nature Communications*, 4(2744), 2013.

[88] A. Delteil, Z. Sun, W. B. Gao, E. Togan, S. Faelt, and A. Imamoğlu. Generation of heralded entanglement between distant hole spins. *Nature Physics*, 12:218–224, 2016.

[89] L. Robledo, L. Childress, H. Bernien, B. Hensen, P. F. A. Alkemade, and R. Hanson. High-fidelity projective read-out of a solid-state spin quantum register. *Nature*, 477:574–578, 2011.

[90] A. Dréau, P. Spinicelli, J. R. Maze, J. F. Roch, and V. Jacques. Single-shot readout of multiple nuclear spin qubits in diamond under ambient conditions. *Physical Review Letters*, 110(060502), 2013.

[91] G. Waldherr, Y. Wang, S. Zaiser, M. Jamali, T. Schulte-Herbrüggen, H. Abe, T. Ohshima, J. Isoya, J. F. Du, P. Neumann, and J. Wrachtrup. Quantum error correction in a solid-state hybrid spin register. *Nature*, 506:204–207, 2014.

[92] C. G. Yale, B. B. Buckley, D. J. Christle, G. Burkard, F. J. Heremans, L. C. Bassett, and D. D. Awschalom. All-optical control of a solid-state spin using coherent dark states. *Proceedings of the National Academy of Sciences*, 110:7595–7600, 2013.

[93] D. A. Golter and H. Wang. Optically driven rabi oscillations and adiabatic passage of single electron spins in diamond. *Physical Review Letters*, 112(116403), 2014.

[94] E. Togan, Y. Chu, A. S. Trifonov, L. Jiang, J. Maze, L. Childress, M. V. G. Dutt, A. S. Sørensen, P. R. Hemmer, A. S. Zibrov, and M. D. Lukin. Quantum entanglement between an optical photon and a solid-state spin qubit. *Nature*, 466:730–734, 2010.

[95] H. Bernien, B. Hensen, W. Pfaff, G. Koolstra, M. S. Blok, L. Robledo, T. H. Taminiau, M. Markham, D. J. Twitchen, L. Childress, and R. Hanson. Heralded entanglement between solid-state qubits separated by 3 meters. *Nature*, 497:86–90, 2012.

[96] W. Pfaff, B. Hensen, H. Bernien, S. B. van Dam, M. S. Blok, T. H. Taminiau, M. J. Tiggelman, R. N. Schouten, M. Markham, D. J. Twitchen, and R. Hanson. Unconditional quantum teleportation between distant solid-state qubits. *Science*, 345:532–536, 2014.

[97] H. P. Breuer and F. Petruccione. *The Theory of Open Quantum Systems*. Oxford University Press, 2002.

[98] C. Cohen-Tannoudji, J. Dupont-Roc, and G. Grynberg. *Atom-Photon Interactions: Basic Processes and Applications*. Wiley-VCH, 2004.

[99] E. Y. Wilner, H. Wang, M. Thoss, and E. Rabani. Sub-Ohmic to super-Ohmic crossover behavior in nonequilibrium quantum systems with electron-phonon interactions. *Physical Review B*, 92:195143, 2015.

[100] A. G. Redfield. On the theory of relaxation processes. *IBM Journal of Research & Development*, 1:19–31, 1957.

[101] J. Jeske, D. Ing, M. B. Plenio, S. F. Huelga, and J. H. Cole. Bloch-Redfield equations for modeling light-harvesting complexes. *Journal of Chemical Physics*, 142:064104, 2015.

[102] P. R. Eastham, P. Kirton, H. M. Cammack, B. W. Lovett, and J. Keeling. Bath-induced coherence and the secular approximation. *Physical Review A*, 94(012110), 2016.

[103] I. De Vega and D. Alonso. Dynamics of non-Markovian open quantum systems. *Reviews of Modern Physics*, 89(015001), 2017.

[104] G. D. Mahan. *Many-Particle Physics: Third Edition*. Kluwer Academic/Plenum Publishers, 2000.

[105] A. Würger. Strong-coupling theory for the spin-phonon model. *Physical Review B*, 57(347), Jan 1998.

[106] I. Wilson-Rae and A. Imamoğlu. Quantum dot cavity-QED in the presence of strong electron-phonon interactions. *Physical Review B*, 65(235311), 2002.

[107] S. Jang, Y.-C. Cheng, D. R. Reichman, and J. D. Eaves. Theory of coherent resonance energy transfer. *The Journal of Chemical Physics*, 129(101104), 2008.

[108] S. Jang. Theory of coherent resonance energy transfer for coherent initial condition. *The Journal of Chemical Physics*, 131(164101), 2009.

[109] A. Nazir. Correlation-dependent coherent to incoherent transitions in resonant energy transfer dynamics. *Physical Review Letters*, 103(146404), 2009.

[110] D. P. S. McCutcheon and A. Nazir. Coherent and incoherent dynamics in excitonic energy transfer: Correlated fluctuations and off-resonance effects. *Physical Review B*, 83(165101), 2011.

[111] Y. Tanimura and R. Kubo. Time Evolution of a Quantum System in Contact with a Nearly Gaussian-Markoffian Noise Bath. *Journal of the Physical Society of Japan*, 58(1):101–114, 1989.

[112] B. M. Garraway. Nonperturbative decay of an atomic system in a cavity. *Physical Review A*, 55(2290), 1997.

[113] J. Iles-Smith, N. Lambert, and A. Nazir. Environmental dynamics, correlations, and the emergence of noncanonical equilibrium states in open quantum systems. *Physical Review A*, 90(032114), 2014.

[114] R. P. Feynman and F. L. Vernon. The theory of a general quantum system interacting with a linear dissipative system. *Annals of Physics*, 24:118–173, 1963.

[115] A. O. Caldeira and A. J. Leggett. Path integral approach to quantum Brownian motion. *Physica A: Statistical Mechanics and its Applications*, 121:587–616, 1983.

[116] A. Strathearn, B. W. Lovett, and P. Kirton. Efficient real-time path integrals for non-Markovian spin-boson models. *New Journal of Physics*, 19(093009), 2017.

[117] A. Strathearn, P. Kirton, D. Kilda, J. Keeling, and B. W. Lovett. Efficient non-Markovian quantum dynamics using time-evolving matrix product operators. *Nature Communications*, 9(3322), 2018.

[118] N. Makri and D. E. Makarov. Tensor propagator for iterative quantum time evolution of reduced density matrices. I. Theory. *The Journal of Chemical Physics*, 102:4600–4610, 1995.

[119] N. Makri and D. E. Makarov. Tensor propagator for iterative quantum time evolution of reduced density matrices. II. Numerical methodology. *The Journal of Chemical Physics*, 102:4611–4618, 1995.

[120] B. Vacchini and H. P. Breuer. Exact master equations for the non-Markovian decay of a qubit. *Physical Review A*, 81:042103, 2010.

[121] V. Weisskopf and E. Wigner. Berechnung der Natürlichen Linienbreite auf Grund der Diracschen Lichttheorie. *Zeitschrift für Physik*, 63:54–73, 1930.

[122] M. D. Crisp. Jaynes-Cummings model without the rotating-wave approximation. *Physical Review A*, 43(2430), 1991.

[123] E. W. Weisstein. Bromwich Integral. From *MathWorld* – A Wolfram Web Resource. http://mathworld.wolfram.com/BromwichIntegral.html. [Online; accessed 18 Sep 2018].

[124] D. F. Walls and G. J. Milburn. *Quantum Optics*. Springer-Verlag Berlin Heidelberg, 2008.

[125] E. Simoen, B. Kaczer, M. Toledano-Luque, and C. Claeys. Random Telegraph Noise: From a Device Physicist's Dream to a Designer's Nightmare. *ECS Transactions*, 39:3–15, 2011.

[126] R. Kubo. Generalized Cumulant Expansion Method. *Journal of the Physical Society of Japan*, 17:1100–1120, 1962.

[127] I. Kuprov. Module VI, Lecture 01: Generalized Cumulant Expansion. http://spindynamics.org/documents/sd_m6_lecture_01.pdf. [Online; accessed 20 Jun 2018].

[128] I. A. Cunningham. Introduction to Random Processes. http://cis.rit.edu/class/simg713/Lectures/Lecture713-12-4.pdf. [Online; accessed 21 Jun 2018].

[129] C. P. Slichter. *Principles of Magnetic Resonance*. Springer, 1996.

[130] T. M. Sweeney, S. G. Carter, A. S. Bracker, M. Kim, C. S. Kim, L. Yang, P. M. Vora, P. G. Brereton, E. R. Cleveland, and D. Gammon. Cavity-stimulated Raman emission from a single quantum dot spin. *Nature Photonics*, 8:442–447, 2014.

[131] S. Weiler, A. Ulhaq, S. M. Ulrich, S. Reitzenstein, A. Löffler, A. Forchel, and P. Michler. Highly indistinguishable photons from a quantum dot in a microcavity. *Physica Status Solidi (B)*, 248:867–871, 2011.

[132] E. Bourgeois, A. Jarmola, P. Siyushev, M. Gulka, J. Hruby, F. Jelezko, D. Budker, and M. Nesladek. Photoelectric detection of electron spin resonance of nitrogen-vacancy centres in diamond. *Nature Communications*, 6:8577, 2015.

[133] S. Johnson, P. R. Dolan, T. Grange, A. A. P. Trichet, G. Hornecker, Y. C. Chen, L. Weng, G. M. Hughes, A. A. R. Watt, A. Auffves, and J. M. Smith. Tunable cavity coupling of the zero phonon line of a nitrogen-vacancy defect in diamond. *New Journal of Physics*, 17:122003, 2015.